12-2017

Mathematical Modeling of Mixtures and Numerical Solution with Applications to Polymer Physics

John Timothy Cummings
University of Tennessee, Knoxville, jcummin9@vols.utk.edu

To the Graduate Council:

I am submitting herewith a dissertation written by John Timothy Cummings entitled "Mathematical Modeling of Mixtures and Numerical Solution with Applications to Polymer Physics." I have examined the final electronic copy of this dissertation for form and content and recommend that it be accepted in partial fulfillment of the requirements for the degree of Doctor of Philosophy, with a major in Mathematics.

Steven Wise, Major Professor

We have read this dissertation and recommend its acceptance:

Ohannes Karakashian, Tim Schulze, Michael Berry, Rajeev Kumar

Accepted for the Council:
Carolyn R. Hodges

Vice Provost and Dean of the Graduate School

(Original signatures are on file with official student records.)

Mathematical Modeling of Mixtures and Numerical Solution with Applications to Polymer Physics

A Dissertation Presented for the

Doctor of Philosophy

Degree

The University of Tennessee, Knoxville

John Timothy Cummings

December 2017

I dedicate this work to my wife, Charisse. Her belief in me has given me strength in the times that I felt certain I would fail. To articulate what her unwavering support has meant to me requires words I cannot assemble.

Acknowledgments

I would like to thank my advisor Dr. Steven Wise for the education and guidance that he has provided in the years I have spent here at the University of Tennessee. Additionally, I would like to thank Dr. Ohannes Karakashian, Dr. Rajeev Kumar, Dr. Tim Schulze, and Dr. Michael Berry for their instruction and service on my committee.

I thank my parents, Rose and Tim Cummings, for providing me with the encouragement throughout my life to pursue my goals. I also thank my mother and father-in-law, Sonny and Mildred Nitura, for their guidance and advice. I thank my siblings Alan, Margaret, Rebecca, and Philip for their wonderful support. I am truly blessed to have the wonderful family that I have.

Many thanks to the friends that I have made, both here at UT and back home. I will always think fondly of the many discussions and activities that we enjoyed together. I especially thank Chris Parsons and Andy Harazin, who convinced me to continue to do mathematics when I was so sure I wanted to quit in despair. Thank you to Eddie, Nathan, and Tyler, the three best roommates one could ask for, for whom without which I would have certainly graduated sooner and with a much less rich graduate career.

Finally, I would like to thank my wife, Charisse, whose kindness, work ethic, and patience are unparalleled. She has been and will continue to be an inspiration to me, and I am extremely grateful for her love and support through graduate school when we have been separated by distance. I have great times ahead simply by having her in my life.

This material is based upon work supported by the U.S. Department of Energy, Office of Science, Office of Workforce Development for Teachers and Scientists, Office of Science Graduate Student Research (SCGSR) program, which was conducted at the Center for Nanophase Matrial Sciences. The SCGSR program is administered by the Oak

Ridge Institute for Science and Education for the DOE under contract number DE-AC05-06OR23100.

Abstract

We consider in this dissertation the mathematical modeling and simulation of a general diffuse interface mixture model based on the principles of energy dissipation. The model developed allows for a thermodynamically consistent description of systems with an arbitrary number of different components, each of which having perhaps differing densities. We also provide a mathematical description of processes which may allow components to source or sink into other components in a mass conserving, energy dissipating way, with the motivation of applying this model to phase transformation. Also included in the modeling is a unique set of thermodynamically consistent boundary conditions which allows flow across the boundary of a select number of components. The result of this modeling is a unique Cahn-Hilliard, Allen-Cahn-like system of equations. For numerical solution of this model, we use cell-centered finite difference methods for discretization and Full Approximation Storage (FAS) multigrid methods to solve the resulting system of equations via use of the BSAM (Block-Structured Adaptive Multigrid) libraries. Upon development of the mathematical model, we consider two applications.

The primary application of this mathematical modeling is the time evolution of a quaternary mixture consisting of a volatile solvent in the liquid phase, solvent in the vapor phase, and two polymers. This modeling is motivated by the need to better understand the active layer in Organic Photovoltaics (OPVs). In this mixture, the volatile solvent is evaporating into the its vapor phase, and upon fully evaporating the polymer mixture which results is the active layer of the OPV device. Simulations are provided which demonstrate the solvent evaporation phenomenon and the resulting microstructure of the active layer.

As a future application, we consider a mixture of a charged polymer and its counterion. We provide a description of the system based on the dissipation of the electrochemical

free energy which allows for the permittivity to be dependent on the volume fractions. Simulations are provided which vary the gradient energies and polymer chain length and demonstrate the different steady-state microstructures which can result.

Table of Contents

List of Tables

List of Figures

Chapter 1

Introduction

1.1 The Cahn-Hilliard Equation

We start by considering a mixture consisting of two components, A and B, and wish to model the spatially dependent concentrations of each component. Let $\phi(\boldsymbol{x}, t)$ be the volume fraction of the B component in the mixture, where $\phi = 1$ indicates pure phase B and $\phi = 0$ indicates pure phase A. At high temperatures, the mixture may prefer (energetically) to be uniform throughout, but at temperatures below some critical temperature $T < T_c$ the system, subject to some initial fluctuation in concentration, can phase separate into regions of relatively pure concentrations of each component through the process known as spinodal decomposition. Cahn and Hilliard provide a diffuse interface description [7, 8] of this by introducing an associated free energy which, assuming a uniform temperature throughout the mixtures, can be expressed as

$$E(\phi) = \int_\Omega f(\phi) + \frac{\epsilon^2}{2}|\nabla\phi|^2 d\boldsymbol{x} \quad \epsilon > 0. \tag{1.1}$$

The first part of the energy $f(\phi)$ is called the homogeneous energy, and the second is called the gradient energy. Common forms of the $f(\phi)$ in the literature are the quartic free energy

$$f_q(\phi) = \frac{1}{4}\phi^2(1-\phi)^2 \tag{1.2}$$

and the logarithmic free energy

$$f_{log}(\phi) = \theta\left[\phi\ln(\phi) + (1-\phi)\ln(1-\phi)\right] + \phi(1-\phi) \quad \theta > 0. \tag{1.3}$$

In the case of the quartic double well energy on the domain $(-\infty, \infty)$, one can show that the solutions have the hyperbolic tangent profile. Consider now taking a time derivative of the free energy

$$\begin{aligned} \frac{dE}{dt} &= \int_\Omega f'(\phi)\frac{\partial\phi}{\partial t} + \epsilon^2\nabla\phi\cdot\nabla\frac{\partial\phi}{\partial t}d\boldsymbol{x} \\ &= \int_\Omega \left(f'(\phi) - \epsilon^2\Delta\phi\right)\frac{\partial\phi}{\partial t}d\boldsymbol{x} + \int_{\partial\Omega}\epsilon^2\frac{\partial\phi}{\partial t}\nabla\phi\cdot\boldsymbol{n}dS \end{aligned} \tag{1.4}$$

It is quite common that the modeling applies to a domain which is a cube in an infinite domain, for which periodic boundary conditions for ϕ apply, or that the system is isolated and locally near the boundary in thermodynamic equilibrium, for which $\nabla\phi\cdot\boldsymbol{n} = 0$ on the boundary. In either case, the surface integral term in (1.4) is zero, so

$$\frac{dE}{dt} = \int_\Omega \left(f'(\phi) - \epsilon^2\Delta\phi\right)\frac{\partial\phi}{\partial t}d\boldsymbol{x}. \tag{1.5}$$

Ubiquitous throughout the modeling of physical phenomena is some energy law, and in this case we require that the free energy of the system is non-increasing. We say a model that obeys this property is thermodynamically consistent. One thermodynamically consistent model for this energy would be the Allen-Cahn equations

$$\begin{aligned} \frac{\partial\phi}{\partial t} &= \mu \\ \mu &= -A\left(f'(\phi) - \epsilon^2\Delta\phi\right) \end{aligned} \tag{1.6}$$

where A is a positive constant. The Allen-Cahn Equation leads to non-conserved dynamics in the sense that, defining the total volume of the B component as

$$V_B(t) = \int_\Omega \phi d\boldsymbol{x} \tag{1.7}$$

we have that

$$\begin{aligned}\frac{dV_B}{dt} &= \int_\Omega \frac{\partial \phi}{\partial t}\boldsymbol{x} \\ &= \int_\Omega -A\left(f'(\phi) - \epsilon^2\Delta\phi\right) d\boldsymbol{x} \neq 0.\end{aligned} \tag{1.8}$$

In particular, the volume of the B component is not necessarily conserved. Often one wants to ensure that the volume (or equivalently, mass) is conserved in the system. It is common to enforce this by assuming that the continuity equation is satisfied

$$\frac{\partial \phi}{\partial t} + \nabla \cdot \boldsymbol{j} = 0 \tag{1.9}$$

where $\boldsymbol{j}$ is the volumetric flux which satisfies a no-flux condition $\boldsymbol{j} \cdot \boldsymbol{n} = 0$ on the boundary, and thus guaranteeing conservation through an application of the divergence theorem. Making this assumption, we compute the time derivative of the energy

$$\begin{aligned}\frac{dE}{dt} &= -\int_\Omega \left(f'(\phi) - \epsilon^2\Delta\phi\right) \nabla \cdot \boldsymbol{j} d\boldsymbol{x} \\ &= \int_\Omega \nabla\left(f'(\phi) - \epsilon^2\Delta\phi\right) \cdot \boldsymbol{j} d\boldsymbol{x} - \int_{\partial\Omega} \left(f'(\phi) - \epsilon^2\Delta\phi\right) \boldsymbol{j} \cdot \boldsymbol{n} dS \\ &= \int_\Omega \nabla\left(f'(\phi) - \epsilon^2\Delta\phi\right) \cdot \boldsymbol{j} d\boldsymbol{x}.\end{aligned} \tag{1.10}$$

We make the constitutive assumption that the volumetric flux satisfies

$$\boldsymbol{j} = -M(\phi)\nabla\left(f'(\phi) - \epsilon^2\Delta\phi\right) \tag{1.11}$$

so that the model is thermodynamically consistent. Here $M(\phi)$ is typically called the mobility and is frequently assumed to either be a positive constant or degenerate as $M(\phi) = C\phi(1-\phi)$, where C is a positive constant. In general, however, it could be some positive operator. With this we write the Cahn-Hilliard equation

$$\begin{aligned}&\frac{\partial \phi}{\partial t} - \nabla \cdot (M(\phi)\nabla\mu) = 0 \\ &\mu = \frac{\delta E}{\delta \phi} = \frac{\partial f(\phi)}{\partial \phi} - \epsilon^2\Delta\phi.\end{aligned} \tag{1.12}$$

From this we obtain the energy decrease of the system as

$$\frac{dE}{dt} = -\int_{\Omega} M(\phi)|\nabla\mu|^2 d\boldsymbol{x} \tag{1.13}$$

1.2 The Multicomponent Cahn-Hilliard Equation and Applications

In this dissertation we are interested in mixtures with more than two components. So as to demonstrate the techniques of the derivation of the upcoming models, we provide a derivation of the binary Cahn-Hilliard equation that is related to the multicomponent case. Let ϕ_i be the volume fractions for the ith component of the mixtures. It is very common to make the approximation that

$$\sum_{i=0}^{1} \phi_i \equiv 1 \tag{1.14}$$

which is sometimes called the no voids or no gaps approximation. The (unconstrained) free energy reads

$$E(t) = \int_{\Omega} f_h(\boldsymbol{\phi}) + \sum_{i=0}^{1} \frac{\epsilon_i^2}{2}|\nabla\phi_i|^2 d\boldsymbol{x} \tag{1.15}$$

where

$$\boldsymbol{\phi} = \begin{bmatrix} \phi_0 \\ \phi_1 \end{bmatrix} \tag{1.16}$$

is the vector whose ith component are the volume fractions of the ith component. The continuity equation for the ith equation is

$$\frac{\partial\phi_i}{\partial t} + \rho_{0,i}^{-1}\nabla\cdot\boldsymbol{j}_i = 0 \tag{1.17}$$

where now the $\boldsymbol{j}_i$ is the *mass* flux of component i and $\rho_{0,i}$ is the density of pure component i. Assuming the boundary conditions

$$\frac{\partial\phi_i}{\partial n} = 0 \tag{1.18}$$

we have that the time derivative of the energy is

$$\begin{aligned}\frac{dE}{dt} &= \int_\Omega \sum_{i=0}^{1} \mu_i \frac{\partial \phi_i}{\partial t} d\boldsymbol{x} \\ &= -\int_\Omega \sum_{i=0}^{1} \mu_i \rho_{0,i}^{-1} \nabla \cdot \boldsymbol{j}_i d\boldsymbol{x}\end{aligned} \tag{1.19}$$

where

$$\mu_i = \frac{\partial f_h(\boldsymbol{\phi})}{\partial \phi_i} - \epsilon_i^2 \Delta \phi_i \tag{1.20}$$

is the variational derivative of the free energy. To conserve mass, we require the boundary conditions for the fluxes satisfy $\boldsymbol{j}_i \cdot \boldsymbol{n} = 0$ and that $\sum_{i=0}^{1} \nabla \cdot \boldsymbol{j}_i = 0$. Substituting the latter into (1.19) we get that

$$\frac{dE}{dt} = \int_\Omega \nabla \left(-\rho_{0,0}^{-1} \mu_0 + \rho_{0,1}^{-1} \mu_1 \right) \cdot \boldsymbol{j}_1 d\boldsymbol{x}. \tag{1.21}$$

If we make the constitutive assumption

$$\boldsymbol{j}_1 = -M \nabla \left(\rho_{0,1}^{-1} \mu_1 - \rho_{0,0}^{-1} \mu_0 \right) \tag{1.22}$$

then it is clear again we have a thermodynamically consistent model. Note that if we make the assumption of matched densities $\rho_{0,0} = \rho_{0,1} = \rho$, then

$$\boldsymbol{j}_1 = -\frac{M}{\rho} \nabla \left(\mu_1 - \mu_0 \right). \tag{1.23}$$

We can relate this matched density model to the derivation in 1.1. If we define

$$\widehat{f}_h(\phi_1) = f_h(1 - \phi_1, \phi_1) \tag{1.24}$$

and

$$\widehat{E}(t) = \int_\Omega \widehat{f}_h(\phi_1) + \frac{\widehat{\epsilon}^2}{2} |\nabla \phi_1|^2 d\boldsymbol{x} \quad \widehat{\epsilon}^2 = \epsilon_0^2 + \epsilon_1^2 \tag{1.25}$$

then we see that, after an application of the chain rule on $\widehat{f_h}$,

$$\begin{aligned}\mu_1 - \mu_0 &= \frac{\partial f_h(\boldsymbol{\phi})}{\phi_1} - \frac{\partial f_h(\boldsymbol{\phi})}{\phi_0} - (\epsilon_0^2 + \epsilon_1^2)\Delta\phi_1 \\ &= \widehat{f}_h'(\phi_1) - \widehat{\epsilon}^2\Delta\phi_1 \\ &= \widehat{\mu}\end{aligned} \tag{1.26}$$

where $\widehat{\mu}$ is the variational derivative of the energy $\widehat{E}$ with respect to ϕ_1, and so once again we have

$$\frac{\partial\phi_1}{\partial t} - \nabla\cdot\widehat{M}\nabla\widehat{\mu} = 0. \tag{1.27}$$

While this derivation is only applied for the two-component, matched density case, this demonstrates the ideas for applying similar techniques to systems with larger number of components and varying densities. In general our strategy will be to start with some free energy of the system, compute its time derivative, and from inspection of the time derivative of the free energy make a choice for the velocities (and other terms to be introduced) that will provide a free energy decrease of the system, thus ensuring our model is thermodynamically consistent. The novelty of our modeling is that it provides a description of systems for which:

1. The model is thermodynamically consistent.
2. The densities of each component may be unequal.
3. The system has source terms, allowing one component of the mixture to source or sink into a different component of the system.
4. The boundary conditions of the system allow for flow of a selection of the components across the boundary.

To demonstrate the subtleties of why 2-4 are necessary, consider the application of a diffuse interface model to a system of a box filled with a volatile liquid. Let us call the volume fraction of the volatile liquid ϕ_l, and the volume fraction of the volatile liquid in the vapor phase ϕ_v, so that $\phi_l = 1$ everywhere in the box initially. Physically, as time evolves one would expect that due to the volatility of the liquid phase ϕ_l will decrease and ϕ_v will increase until eventually all the liquid phase has evaporated and $\phi_v = 1$. With the intuition that the

system will try to minimize its free energy, it is reasonable to construct some free energy that is lower if the system is occupied by the vapor phase, and develop some mechanism so that the two components can source and sink into the other in a way that decreases the free energy. One would then expect the qualitative behavior of the system to "prefer" the vapor concentration, as energetically it would be more favorable for $\phi_v \approx 1$, and thus decrease ϕ_l and increase ϕ_v. There is a problem with this approach in the sense of mass conservation if no-flow or periodic boundary conditions for the velocities are used. Since the densities are not equal in this model, the mass of the initial state of the system is greater than that of the mass of the final state. If one implements boundary conditions that are no-flow or periodic for this type of system, which is typical, it is easy to show as in (2.33) that the time derivative of the mass is zero, which is not desired for the system described! What is needed mathematically is some mechanism that allows for the system to change of the mass, and that is done through the boundary conditions of the velocities, which demonstrates the necessity of the flow boundary conditions.

This mathematical modeling in this dissertation is related to approaches based on recent tumor growth models [56, 48, 13, 55] in the sense that we apply a multicomponent diffuse interface model based on the principles of energy dissipation, with the introduction of new source terms and boundary conditions which are thermodyanmically consistent. Energetic variational principles applied to systems with advection driven by a single barycentric velocity paired with Allen-Cahn and Cahn-Hilliard dynamics considered in [33], without the boundary conditions required for this application, is also highly relevant. For alternative approaches to the multicomponent Cahn-Hilliard equations as a constrained H^{-1} gradient flow of the energy and its possible coupling with flow effects, we reference [24, 6, 28]. The primary application that is considered is the time evolution of a multicomponent mixture in which one component of the mixture is volatile. This is especially of interest in the construction of the active layer in organic photovoltaics (OPVs), in which this multicomponent mixture is deposited on a substrate and allowed to evolve in time. Of special interest is how the interfaces evolve in time, and one of the most attractive properties of diffuse interface models is that they allow for details on the interface location without need to computationally track the interface. Eventually the volatile solvent evaporates fully from

the mixture and what is left is the other components which constitute the active layer of the OPV device. To our knowledge there are no models which attempt to describe such a system that includes the mass density difference of the solvent in the vapor and liquid phases, though there are some recent notable works. A common characteristic for some similar models is that some assumption is made which allows for the issue of density differences in the evaporation of the volatile liquid to its vapor phase to be simplified in some manner, for example by either assuming some form a-priori of the interface [39], assuming matched densities by modeling a system in which the solvent-polymer mixture is immersed in a non-solvent bath [49], or simulating a top-down view of the system and removing solvent from the system at each time step [30]. We consider a flow model for the velocities that is Darcy-like in this application, though there are a wealth of interesting multiphysics that could be paired with this model in the form of Navier-Stokes equations, Hele-Shaw Equations, Darcy-Stokes Equations, etc. [1, 21, 26, 34, 17, 32] that allow our developments in treating one of the components as volatile to be applied to a variety of systems.

As a future application, we consider an ionic liquid system of a charged polymer between two parallel planar electrodes and provide simulation of the resulting time dependent mictrostructural evolution of a charged polymer under an applied voltage. In the case of a constant permittivity, the derived equations for the multi-component system bears resemblance to the Poisson-Nernst-Planck equations, with the addition of gradient energy terms and the Flory energy of mixing term. Recently for two components [25] in a similar model, a one dimensional stability analysis demonstrates critical parameter values for which the solution prefers different resulting microstructures. We include a derivation which extends this model to the case where the permittivity may be spatially and temporally dependent through the dependence on the concentration variables ϕ_i, and is similar in nature to techniques used in the polymer community that describe these systems through the Rayleighian functional to prescribe an appropriate energy dissipation [19, 31]. With the intentions of, in future works, studying the dependence of the effect of the variable permittivity and analyzing the electric current produced, we present preliminary simulations which demonstrate the effect of the polymer chain length and gradient energy coefficients in the constant permittivity system.

For numerical simulation of the applications described, we use first order semi-implicit finite difference methods for time discretization and second order finite differences the for spatial discretization, which we solve using efficient block structured adaptive multigrid methods [50] implemented through the BSAM package [54]. There is difficulty in solving the equations as in the energy

$$E = \int_\Omega f_h(\boldsymbol{\phi}) + \sum_{i=0}^{N} |\nabla \phi_i|^2 d\boldsymbol{x} \tag{1.28}$$

$f_h(\boldsymbol{\phi})$ is of the form

$$f_h(\boldsymbol{\phi}) = \sum_{i=0}^{N} \rho_i \phi_i \ln(\phi_i) + \sum_{i \neq j} \chi_{ij} \phi_i \phi_j \tag{1.29}$$

where ρ_i, χ_{ij} are some positive constants. In the applications we consider, it is common (and physically quite practical) that some of the components' volume fractions ϕ_i are approximately 0 or 1, from which numerical difficulties arise in evaluating logarithms in the equations due to the singularity of the logarithm near 0. This causes the governing equations of the system to be quite stiff, limiting the allowable time step, especially in the semi-implicit discretization for which the logarithm term is treated explicitly in the time discretization, as this introduces a stability condition $\Delta t < Ch^4$ [12]. Very little in the literature is available for constructing energy stable schemes for multicomponent Cahn-Hilliard systems with logarithmic free energy. Notably Kim and Jeong [28] provide analysis of a stable scheme by discretizing the homogeneous free energy as

$$f_h(\boldsymbol{\phi}^{n+1}, \boldsymbol{\phi}^n) = \sum_{i=0}^{N} \rho_i \phi_i^n \ln_\delta(\phi_i^n) + \sum_{i \neq j} \chi_{ij} \phi_i^n \phi_j^n + \sum_{i=0}^{N} \left(\chi A \left(\phi_i^{n+1}\right)^2 - \chi A \left(\phi_i^n\right)^2 \right) \tag{1.30}$$

where A is some non-negative constant and $\ln_\delta(\phi)$ is the approximation to the logarithm

$$\ln_\delta(x) = \begin{cases} \ln(x) & x > \delta \\ \ln(\delta) + 2\frac{x}{\delta} - \frac{x^2}{2\delta^2} - 1.5 & x \leq \delta. \end{cases} \tag{1.31}$$

The ideas of this strategy originate from Eyre [20], where the energy is split into a convex and concave piece, $F_c(\boldsymbol{\phi}), F_e(\boldsymbol{\phi})$ respectively, and then a time discretization of the energy

$$E = \int_\Omega F_c(\boldsymbol{\phi}^{n+1}) + F_e(\boldsymbol{\phi}^n) d\boldsymbol{x} \tag{1.32}$$

is applied. In 1.30, an "artificial" term has been introduced, and if one assumes that $\rho_i = \rho$ $\forall i$ and $\chi_{ij} = \chi$ $\forall ij$, then this splitting is convex only if

$$\phi > \frac{4\delta\rho - (A+1)\chi\delta^2}{3\rho} \tag{1.33}$$

when $\phi < \delta$. Since we know that the volume fractions ϕ_i can be very close to 0 or 1, we wish this discretization to be stable for all $\phi_i \in (0, 1)$. Assuming that $\chi = \rho$, for this scheme to be stable for all such $\phi_i \in (0, 1)$ we must have

$$A > \frac{4}{\delta} - 1 \tag{1.34}$$

which is impractical for this application as we use $\delta = 10^{-3}$ in simulation.

Chapter 2

Mathematical Modeling of Multicomponent Mixtures

2.1 Fundamentals

Consider a mixture of $N+1$ components in a domain $\Omega \subset \mathbb{R}^d$ with $\rho_i(\boldsymbol{x}, t)$ representing the number density of the ith component. We write the conservation of mass through the continuity equations

$$\frac{\partial \rho_i(\boldsymbol{x}, t)}{\partial t} + \nabla \cdot \boldsymbol{j}_i = S_i(\boldsymbol{x}, t) \quad i = 0, 1, \ldots N \tag{2.1}$$

where $\boldsymbol{j}_i$ is the flux of the ith component, for which we choose to be advective and distinct for each i, and so

$$\frac{\partial \rho_i(\boldsymbol{x}, t)}{\partial t} + \nabla \cdot (\rho_i(\boldsymbol{x}, t)\boldsymbol{u}_i(\boldsymbol{x}, t)) = S_i(\boldsymbol{x}, t) \tag{2.2}$$

where $S_i(\boldsymbol{x}, t)$ is a source term. We assume that this density function can be written as

$$\rho_i(\boldsymbol{x}, t) = \rho_{0,i}\phi_i(\boldsymbol{x}, t) \tag{2.3}$$

where $\rho_{0,i}$ is the (constant) density of the pure ith phase and $\phi_i(\boldsymbol{x}, t)$ is the volume fraction of the ith component. Under this assumption the continuity equation reads

$$\frac{\partial \phi_i(\boldsymbol{x}, t)}{\partial t} + \nabla \cdot (\phi_i(\boldsymbol{x}, t)\boldsymbol{u}_i(\boldsymbol{x}, t)) = \rho_{0,i}^{-1} S_i(\boldsymbol{x}, t). \tag{2.4}$$

The total mass of the system is

$$M(t) = \int_\Omega \sum_{i=0}^{N} \rho_i(\boldsymbol{x}, t) d\boldsymbol{x}. \tag{2.5}$$

Consider computing the time derivative of the mass of the system as

$$\begin{aligned} \frac{dM}{dt} &= \int_\Omega \sum_{i=0}^{N} \frac{\partial \rho_i(\boldsymbol{x}, t)}{\partial t} d\boldsymbol{x} \\ &= \int_\Omega -\nabla \cdot \left(\sum_{i=0}^{N} \rho_i(\boldsymbol{x}, t)\boldsymbol{u}_i(\boldsymbol{x}, t) \right) + \sum_{i=0}^{N} S_i(\boldsymbol{x}, t) d\boldsymbol{x} \\ &= -\int_{\partial\Omega} \sum_{i=0}^{N} \rho_i(\boldsymbol{x}, t)\boldsymbol{u}_i(\boldsymbol{x}, t) \cdot \boldsymbol{n} dS + \int_\Omega \sum_{i=0}^{N} S_i(\boldsymbol{x}, t) d\boldsymbol{x}. \end{aligned} \tag{2.6}$$

We leave the discussion of the boundary terms in the mass time derivative for later, but remark only that in the applications that will be discussed they are *not necessarily* assumed to be the commonly used no-flow boundary conditions, but a boundary condition that will allow for the system to change mass in a thermodynamically consistent way, thus decreasing the free energy of the system. In the applications to follow, the source terms will allow for one component of the mixture to change into another component, specifically implemented later to model the phenomenon of evaporation, though other types of sources, such as chemical reactions, could be considered. With this in mind, physically we do not expect the system to change its mass through this mechanism, as this is a phenomenon that occurs in the interior of the domain that only transfers mass of one component to mass of some other component. As such, we pointwise enforce the condition that

$$\sum_{i=0}^{N} S_i(\boldsymbol{x}, t) = 0. \tag{2.7}$$

Consider summing (2.2) on i and applying (2.7) so that

$$\sum_{i=0}^{N} \frac{\partial \rho_i(\boldsymbol{x},t)}{\partial t} + \nabla \cdot \left(\sum_{i=0}^{N} \rho_i(\boldsymbol{x},t)\boldsymbol{u}_i(\boldsymbol{x},t) \right) = \sum_{i=0}^{N} S_i(\boldsymbol{x},t) = 0. \tag{2.8}$$

We define the mixture density $\rho(\boldsymbol{x},t)$ and mass averaged velocity $\boldsymbol{u}(\boldsymbol{x},t)$ to be

$$\rho(\boldsymbol{x},t) = \sum_{i=0}^{N} \rho_i(\boldsymbol{x},t) \tag{2.9}$$

and

$$\boldsymbol{u}(\boldsymbol{x},t) = \frac{\sum_{i=0}^{N} \rho_i(\boldsymbol{x},t)\boldsymbol{u}_i(\boldsymbol{x},t)}{\rho(\boldsymbol{x},t)}. \tag{2.10}$$

Substituting these definitions into (2.8) we have the continuity equation for the mixture to be

$$\frac{\partial \rho(\boldsymbol{x},t)}{\partial t} + \nabla \cdot (\rho(\boldsymbol{x},t)\boldsymbol{u}(\boldsymbol{x},t)) = 0. \tag{2.11}$$

From summing (2.4) on i we have the equation for the volume fractions to be

$$\sum_{i=0}^{N} \frac{\partial \phi_i(\boldsymbol{x},t)}{\partial t} + \nabla \cdot \left(\sum_{i=0}^{N} \phi_i(\boldsymbol{x},t)\boldsymbol{u}_i(\boldsymbol{x},t) \right) = \rho_{0,i}^{-1} S_i(\boldsymbol{x},t). \tag{2.12}$$

We also assume that there are no voids in the mixture so that the volume fractions satisfy

$$\sum_{i=0}^{N} \phi_i(\boldsymbol{x},t) \equiv 1 \tag{2.13}$$

and thus

$$\nabla \cdot \left(\sum_{i=0}^{N} \phi_i(\boldsymbol{x},t)\boldsymbol{u}_i(\boldsymbol{x},t) \right) = \rho_{0,i}^{-1} S_i(\boldsymbol{x},t). \tag{2.14}$$

Conversely, upon supposing that

$$\sum_{i=0}^{N} \phi_i(\boldsymbol{x},0) \equiv 1 \tag{2.15}$$

holds, the no-voids constraint is satisfied. They are equivalent statements. Thus one of the phase variables can be algebraically solved in terms of the others as

$$\phi_i(\boldsymbol{x}, t) = 1 - \sum_{j \neq i} \phi_j(\boldsymbol{x}, t). \tag{2.16}$$

2.2 Building Thermodynamically Consistent Equations

We assume that the system has constant temperature throughout. We do remark that this approximation may not be entirely physical [53] for the applications that we will consider, specifically where a phase change occurs. However, upon making an assumption that these are small enough to be neglected, for the governing equations to be thermodynamically consistent the system must decrease its Helmholtz free energy, which is defined to be

$$E(t) = \int_\Omega e(\boldsymbol{\phi}(\boldsymbol{x}, t), \nabla \boldsymbol{\phi}(\boldsymbol{x}, t)) d\boldsymbol{x} + \int_{\partial\Omega} e_s(\boldsymbol{\phi}(\boldsymbol{x}, t)) dS \tag{2.17}$$

where $\boldsymbol{\phi}$ is the vector with ith component $\phi_i(\boldsymbol{x}, t)$. The energy may have many different contributions, and for now we consider the chemical energy

$$E_{\text{chem}}(t) = \int_\Omega f_h(\boldsymbol{\phi}(\boldsymbol{x}, t)) + \sum_{i=0}^{N} \frac{\epsilon_i^2}{2} |\nabla \phi_i(\boldsymbol{x}, t)|^2 d\boldsymbol{x} + \int_{\partial\Omega} f_s(\boldsymbol{\phi}(\boldsymbol{x}, t)) dS. \tag{2.18}$$

Computing the time derivative of the free energy, we have

$$\begin{aligned}
\frac{dE_{\text{chem}}}{dt} &= \int_\Omega \sum_{i=0}^{N} \frac{\partial f_h(\boldsymbol{\phi}(\boldsymbol{x}, t))}{\partial \phi_i} \frac{\partial \phi_i(\boldsymbol{x}, t)}{\partial t} + \sum_{i=0}^{N} \epsilon_i^2 \nabla \phi_i(\boldsymbol{x}, t) \cdot \nabla \frac{\partial \phi_i(\boldsymbol{x}, t)}{\partial t} d\boldsymbol{x} \\
&\quad + \int_{\partial\Omega} \sum_{i=0}^{N} \frac{\partial f_s(\boldsymbol{\phi}(\boldsymbol{x}, t))}{\partial \phi_i} \frac{\partial \phi_i(\boldsymbol{x}, t)}{\partial t} dS \\
&= \int_\Omega \sum_{i=0}^{N} \frac{\partial f_h(\boldsymbol{\phi}(\boldsymbol{x}, t))}{\partial \phi_i} \frac{\partial \phi_i(\boldsymbol{x}, t)}{\partial t} - \sum_{i=0}^{N} \epsilon_i^2 \Delta \phi_i(\boldsymbol{x}, t) \frac{\partial \phi_i(\boldsymbol{x}, t)}{\partial t} d\boldsymbol{x} \\
&\quad + \int_{\partial\Omega} \sum_{i=0}^{N} \frac{\partial f_s(\boldsymbol{\phi}(\boldsymbol{x}, t))}{\partial \phi_i} \frac{\partial \phi_i(\boldsymbol{x}, t)}{\partial t} + \sum_{i=0}^{N} \epsilon_i^2 \nabla \phi_i(\boldsymbol{x}, t) \cdot \boldsymbol{n} \frac{\partial \phi_i(\boldsymbol{x}, t)}{\partial t} dS.
\end{aligned} \tag{2.19}$$

We will assume that locally near the boundary the solution is in thermodynamic equilibrium, though we remark that there are other choices that one could make here that dissipate the free energy. This assumption leads to the boundary conditions

$$\epsilon_i^2 \nabla \phi_i \cdot \boldsymbol{n} - \epsilon_0^2 \nabla \phi_0 \cdot \boldsymbol{n} + \frac{\partial f_s(\boldsymbol{\phi})}{\partial \phi_i} - \frac{\partial f_s(\boldsymbol{\phi})}{\partial \phi_0} = 0, \quad i = 1, \cdots, N, \quad \text{on} \quad \partial\Omega \tag{2.20}$$

after recalling the enforcement of the no voids constraint

$$\sum_{i=0}^{N} \frac{\partial \phi_i(\boldsymbol{x}, t)}{\partial t} = 0. \tag{2.21}$$

We wish to construct thermodynamically consistent constitutive equations for the velocities in the continuity equation. We define

$$\mu_i(\boldsymbol{x}, t) = \frac{\partial f_h(\boldsymbol{\phi}(\boldsymbol{x}, t))}{\partial \phi_i} - \epsilon_i^2 \Delta \phi_i(\boldsymbol{x}, t) \tag{2.22}$$

and compute the time derivative of the free energy as (assuming the boundary conditions (2.20))

$$\begin{aligned} \frac{dE_{\text{chem}}}{dt} &= \sum_i \int_\Omega \mu_i(\boldsymbol{x}, t) \frac{\partial \phi_i(\boldsymbol{x}, t)}{\partial t} d\boldsymbol{x} \\ &= \sum_i \int_\Omega \mu_i(\boldsymbol{x}, t) \left(-\nabla \cdot (\phi_i(\boldsymbol{x}, t) \boldsymbol{u}_i(\boldsymbol{x}, t)) + \rho_{0,i}^{-1} S_i(\boldsymbol{x}, t) \right) d\boldsymbol{x} \\ &= \sum_i \int_\Omega \phi_i(\boldsymbol{x}, t) \nabla \mu_i(\boldsymbol{x}, t) \cdot \boldsymbol{u}_i(\boldsymbol{x}, t) + \mu_i(\boldsymbol{x}, t) \rho_{0,i}^{-1} S_i(\boldsymbol{x}, t) d\boldsymbol{x} \\ &\quad - \sum_i \int_{\partial\Omega} \phi_i(\boldsymbol{x}, t) \mu_i(\boldsymbol{x}, t) \boldsymbol{u}_i(\boldsymbol{x}, t) \cdot \boldsymbol{n} dS. \end{aligned} \tag{2.23}$$

With the intentions of introducing constitutive equations that respect the no voids constraint (2.13) in the free energy functional, we introduce the Lagrange multiplier $p(\boldsymbol{x}, t)$ and note that since (2.13) holds

$$0 = \int_\Omega p(\boldsymbol{x}, t) \sum_{i=0}^{N} \frac{\partial \phi_i(\boldsymbol{x}, t)}{\partial t} d\boldsymbol{x}. \tag{2.24}$$

$p(\boldsymbol{x},t)$ will henceforth be referred to as the pressure. After applying the continuity equation and integration by parts we have

$$\begin{aligned} 0 &= \int_\Omega p(\boldsymbol{x},t) \sum_{i=0}^{N} \left(-\nabla\cdot(\phi_i(\boldsymbol{x},t)\boldsymbol{u}_i(\boldsymbol{x},t)) + \rho_{0,i}^{-1} S_i(\boldsymbol{x},t)\right) d\boldsymbol{x} \\ &= \sum_{i=0}^{N} \int_\Omega \phi_i(\boldsymbol{x},t)\nabla p(\boldsymbol{x},t)\cdot\boldsymbol{u}_i(\boldsymbol{x},t) + \rho_{0,i}^{-1} p(\boldsymbol{x},t) S_i(\boldsymbol{x},t) d\boldsymbol{x} \\ &- \sum_{i=0}^{N} \int_{\partial\Omega} \phi_i(\boldsymbol{x},t) p(\boldsymbol{x},t)\boldsymbol{u}_i(\boldsymbol{x},t)\cdot\boldsymbol{n} dS. \end{aligned} \tag{2.25}$$

Upon combining (2.23) with the multiplier (2.25) we calculate

$$\begin{aligned} \frac{dE_{\text{chem}}}{dt} &= \sum_{i=0}^{N} \int_\Omega \phi_i(\boldsymbol{x},t)\nabla\left(\mu_i(\boldsymbol{x},t) + p(\boldsymbol{x},t)\right)\cdot\boldsymbol{u}_i(\boldsymbol{x},t) d\boldsymbol{x} \\ &+ \sum_{i=0}^{N} \int_\Omega \rho_{0,i}^{-1}\left(\mu_i(\boldsymbol{x},t) + p(\boldsymbol{x},t)\right) S_i(\boldsymbol{x},t) d\boldsymbol{x} \\ &- \sum_{i=0}^{N} \int_{\partial\Omega} \phi_i(\boldsymbol{x},t)\left(\mu_i(\boldsymbol{x},t) + p(\boldsymbol{x},t)\right)\boldsymbol{u}_i(\boldsymbol{x},t)\cdot\boldsymbol{n} dS \end{aligned} \tag{2.26}$$

where we have applied the continuity equation and integration by parts. Enforcing the conservation of mass requirement of the sources in (2.7), we write

$$S_0(\boldsymbol{x},t) = -\sum_{i=1}^{N} S_i(\boldsymbol{x},t). \tag{2.27}$$

Substituting this into the second term of (2.26) we have that

$$\begin{aligned} \frac{dE_{\text{chem}}}{dt} &= \sum_{i=0}^{N} \int_\Omega \phi_i(\boldsymbol{x},t)\nabla\left(\mu_i(\boldsymbol{x},t) + p(\boldsymbol{x},t)\right)\cdot\boldsymbol{u}_i(\boldsymbol{x},t) d\boldsymbol{x} \\ &+ \sum_{i=1}^{N} \int_\Omega \left(\rho_{0,i}^{-1}\mu_i(\boldsymbol{x},t) - \rho_{0,i}^{-1}\mu_0(\boldsymbol{x},t) + (\rho_{0,i}^{-1} - \rho_{0,0}^{-1}) p(\boldsymbol{x},t)\right) S_i(\boldsymbol{x},t) d\boldsymbol{x} \\ &- \sum_{i=0}^{N} \int_{\partial\Omega} \phi_i(\boldsymbol{x},t)\left(\mu_i(\boldsymbol{x},t) + p(\boldsymbol{x},t)\right)\boldsymbol{u}_i(\boldsymbol{x},t)\cdot\boldsymbol{n} dS. \end{aligned} \tag{2.28}$$

We make the definitions

$$\begin{aligned} q_i(\boldsymbol{x},t) &= \rho_{0,i}^{-1}\mu_i(\boldsymbol{x},t) - \rho_{0,0}^{-1}\mu_0(\boldsymbol{x},t) + (\rho_{0,i}^{-1} - \rho_{0,0}^{-1})p(\boldsymbol{x},t) \\ \boldsymbol{Q}_i(\boldsymbol{x},t) &= \phi_i \nabla\left(\mu_i(\boldsymbol{x},t) + p(\boldsymbol{x},t)\right), \quad r_i(\boldsymbol{x},t) = \phi_i\left(\mu_i(\boldsymbol{x},t) + p(\boldsymbol{x},t)\right) \end{aligned} \tag{2.29}$$

so that

$$\begin{aligned} \frac{dE_{\text{chem}}}{dt} &= \sum_{i=0}^{N}\int_\Omega \boldsymbol{Q}_i(\boldsymbol{x},t)\cdot\boldsymbol{u}_i(\boldsymbol{x},t)d\boldsymbol{x} \\ &+ \sum_{i=1}^{N}\int_\Omega q_i(\boldsymbol{x},t)S_i(\boldsymbol{x},t)d\boldsymbol{x} \\ &- \sum_{i=0}^{N}\int_{\partial\Omega} r_i(\boldsymbol{x},t)\boldsymbol{u}_i(\boldsymbol{x},t)\cdot\boldsymbol{n}dS. \end{aligned} \tag{2.30}$$

Suppose that the boundary comprises of two types of boundary, $\partial\Omega = \Gamma_A \cup \Gamma_B$, where $\Gamma_A = \Gamma_{\text{no-flow}} \cup \Gamma_{\text{perioidic}}$ is a no-flow (or periodic boundary in the case of a rectangular domain) and Γ_B is a boundary which is open to flow. Then

$$\begin{aligned} \frac{dE_{\text{chem}}}{dt} &= \sum_{i=0}^{N}\int_\Omega \boldsymbol{Q}_i(\boldsymbol{x},t)\cdot\boldsymbol{u}_i(\boldsymbol{x},t)d\boldsymbol{x} \\ &+ \sum_{i=1}^{N}\int_\Omega q_i(\boldsymbol{x},t)S_i(\boldsymbol{x},t)d\boldsymbol{x} \\ &- \sum_{i=0}^{N}\int_{\Gamma_B} r_i(\boldsymbol{x},t)\boldsymbol{u}_i(\boldsymbol{x},t)\cdot\boldsymbol{n}dS. \end{aligned} \tag{2.31}$$

Indeed, there are many choices of constitutive equations for the velocities that decrease this free energy. Here we choose the evolution laws so that each term in (2.31) is nonpositive

$$\begin{aligned}
&\boldsymbol{u}_i(\boldsymbol{x},t) = -\gamma_i \boldsymbol{Q}_i(\boldsymbol{x},t) \quad i = 0,1,\dots,N \quad \text{in } \Omega \\
&S_i(\boldsymbol{x},t) = -\lambda_i q_i(\boldsymbol{x},t) \quad i = 1,\dots,N \quad \text{in } \Omega \\
&S_0(\boldsymbol{x},t) = -\sum_{i=1}^{N} S_i(\boldsymbol{x},t) \\
&\boldsymbol{u}_i(\boldsymbol{x},t)\cdot\boldsymbol{n} = \omega_i r_i(\boldsymbol{x},t) \quad i = 0,1,\dots,N \quad \text{on } \Gamma_B \\
&\boldsymbol{u}_i\cdot\boldsymbol{n} = 0 \quad i = 0,1,\dots,N \quad \text{on } \Gamma_{\text{no-flow}}
\end{aligned} \tag{2.32}$$

where γ_i, λ, and ω_i are all positive constants, though could be positive operators more generally, with periodic boundary conditions on Γ_{periodic}. It is important to note that through this choice of boundary conditions the mass of the system is *not* be conserved, as

$$\begin{aligned}
\frac{dM}{dt} &= \int_\Omega \sum_{i=0}^{N} \frac{\partial \rho_i(\boldsymbol{x},t)}{\partial t} d\boldsymbol{x} \\
&= \int_\Omega -\nabla\cdot\left(\sum_{i=0}^{N} \rho_i(\boldsymbol{x},t)\boldsymbol{u}_i(\boldsymbol{x},t)\right) d\boldsymbol{x} \\
&= -\int_{\Gamma_B} \sum_{i=0}^{N} \rho_i(\boldsymbol{x},t)\boldsymbol{u}_i(\boldsymbol{x},t)\cdot\boldsymbol{n} dS \\
&= -\int_{\Gamma_B} \sum_{i=0}^{N} \rho_{0,i}\phi_i^2(\boldsymbol{x},t)\omega_i \left(\mu_i(\boldsymbol{x},t) + p(\boldsymbol{x},t)\right)\cdot\boldsymbol{n} dS.
\end{aligned} \tag{2.33}$$

With these constitutive equations in hand we can eliminate the velocities and write

$$\frac{\partial \phi_i(\boldsymbol{x},t)}{\partial t} - \nabla\cdot\left(\gamma_i\phi_i^2(\boldsymbol{x},t)\nabla\left(\mu_i(\boldsymbol{x},t) + p(\boldsymbol{x},t)\right)\right) = \rho_{0,i}^{-1} S_i \quad i = 0,1,\dots,N \tag{2.34}$$

$$\mu_i(\boldsymbol{x},t) = \frac{\partial f_h(\boldsymbol{\phi})}{\partial \phi_i} - \epsilon_i^2 \Delta\phi_i(\boldsymbol{x},t) \quad i = 0,1,\dots,N. \tag{2.35}$$

Having eliminated the velocity $\boldsymbol{u}_i(\boldsymbol{x},t)$ we now specify appropriate boundary conditions for $\mu_i(\boldsymbol{x},t)$ and $p(\boldsymbol{x},t)$. On $\Gamma_{\text{no-flow}}$ we desire the no-flow boundary condition for $\boldsymbol{u}_i(\boldsymbol{x},t)$, and so on this portion of the boundary we specify homogeneous Neumann boundary conditions

for $\mu_i(\boldsymbol{x}, t)$ and $p(\boldsymbol{x}, t)$, since if

$$\nabla \mu_i(\boldsymbol{x}, t) \cdot \boldsymbol{n} = 0 \text{ and } \nabla p(\boldsymbol{x}, t) \cdot \boldsymbol{n} = 0 \tag{2.36}$$

then

$$\boldsymbol{u}_i(\boldsymbol{x}, t) \cdot \boldsymbol{n} = \phi_i(\boldsymbol{x}, t)\gamma_i \nabla(\mu_i(\boldsymbol{x}, t) + p(\boldsymbol{x}, t)) \cdot \boldsymbol{n} = 0. \tag{2.37}$$

More care needs to be taken on Γ_B, which can be thought of as a semi-permeable boundary. In our applications we will allow some components to flux across the open boundary Γ_B, and so we combine the interior and boundary velocity equations in (2.32) to obtain appropriate thermodynamically consistent boundary conditions for μ_i and p. For the upcoming discussion on these boundary conditions, we remark that if there are no components which flow across the boundary, then homogeneous Neumann boundary conditions for all μ_i, p are appropriate. For that reason we assume that *at least* one of the components flow across the boundary, and as such further assume that the $i = 0$ component has flow across the boundary. For a component i which may flow across Γ_B we must have that

$$-\nabla(\mu_i(\boldsymbol{x}, t) + p(\boldsymbol{x}, t)) \cdot \boldsymbol{n} = \beta_i \left(\mu_i(\boldsymbol{x}, t) + p(\boldsymbol{x}, t)\right) \quad \text{where } \beta_i = \frac{\omega_i}{\gamma_i}, \tag{2.38}$$

and perhaps the most natural way to enforce such a condition is to require the Robin-type boundary conditions for the variables $\mu_i(\boldsymbol{x}, t)$ and $p(\boldsymbol{x}, t)$. Firstly, let

$$-\nabla p(\boldsymbol{x}, t) \cdot \boldsymbol{n} = \beta p(\boldsymbol{x}, t) \quad -\nabla \mu_0(\boldsymbol{x}, t) \cdot \boldsymbol{n} = \beta \mu_0(\boldsymbol{x}, t) \quad \text{on } \partial\Gamma_B. \tag{2.39}$$

Now, for each other component i which has flow across the boundary we enforce the boundary condition

$$-\nabla \mu_i(\boldsymbol{x}, t) \cdot \boldsymbol{n} = \beta_i \mu_i + (\beta_i - \beta)\, p \tag{2.40}$$

since, if (2.40) holds, then

$$\begin{aligned} -\nabla(\mu_i(\boldsymbol{x}, t) + p(\boldsymbol{x}, t)) \cdot \boldsymbol{n} &= \beta_i \mu_i(\boldsymbol{x}, t) + (\beta_i - \beta)\, p(\boldsymbol{x}, t) + \beta p(\boldsymbol{x}, t) \\ &= \beta_i \left(\mu_i(\boldsymbol{x}, t) + p(\boldsymbol{x}, t)\right) \end{aligned} \tag{2.41}$$

as desired. For the components which do not flow across the boundary, note that since the pressure boundary conditions have already been prescribed, specifying homogeneous Neumann boundary conditions for the chemical potential would lead to flow across the boundary. In fact, we have that the no flow boundary conditions for the ith component

$$\boldsymbol{u}_i \cdot \boldsymbol{n} = 0 \tag{2.42}$$

implies that $\beta_i = 0$, for which the boundary conditions are

$$\begin{aligned} -\nabla \mu_i(\boldsymbol{x}, t) \cdot \boldsymbol{n} &= -\beta p(\boldsymbol{x}, t) \quad \text{by (2.40)} \\ &= \nabla p(\boldsymbol{x}, t) \cdot \boldsymbol{n} \quad \text{by (2.39)} \end{aligned} \tag{2.43}$$

All that is left is to include the local thermodynamic equilibrium boundary conditions (2.20). $f_s(\boldsymbol{\phi})$ will be a function which allows for portions of the boundary to exhibit preference for one of the components of the mixture. In this dissertation we consider a linear dependence on the concentration

$$f_s(\boldsymbol{\phi}) = \sum_{i=0}^{N} \alpha_i \phi_i. \tag{2.44}$$

2.2.1 A Pressure Poisson Equation

Due to the no voids constraint, which implies

$$\sum_{i=0}^{N} \frac{\partial}{\partial t} \phi_i(\boldsymbol{x}, t) = 0, \tag{2.45}$$

one of the components in the system of equations, which we will assume here to be the zeroth component, is never solved numerically, as it can be algebraically solved for after the other partial differential equations have been numerically solved. Our goal now is to eliminate the two Cahn-Hilliard like equations for the $i = 0$ component, and obtain an equation for the pressure. To obtain an equation for the pressure, consider summing (2.34) on i and applying

the no voids constraint (2.45) so as to obtain the equation

$$-\sum_{i=0}^{N}\nabla\cdot\left(\gamma_i\phi_i^2(\boldsymbol{x},t)\nabla\left(\mu_i(\boldsymbol{x},t)+p(\boldsymbol{x},t)\right)\right)=\sum_{i=1}^{N}\left(\rho_{0,i}^{-1}-\rho_{0,0}^{-1}\right)S_i(\boldsymbol{x},t) \tag{2.46}$$

which we call the pressure Poisson equation. Instead of solving for ϕ_0, μ_0 via the partial differential equations previously given in (2.34) and (2.35), we solve the other components' partial differential equations coupled with this pressure Poisson equation. This reduces the problem to solving the system of equations

$$\frac{\partial\phi_i(\boldsymbol{x},t)}{\partial t}-\nabla\cdot\left(\gamma_i\phi_i^2(\boldsymbol{x},t)\nabla\left(\mu_i(\boldsymbol{x},t)+p(\boldsymbol{x},t)\right)\right)=\rho_{0,i}^{-1}S_i\quad i=1,2,\ldots,N \tag{2.47}$$

$$S_i(\boldsymbol{x},t)=-\lambda_i\left(\rho_{0,i}^{-1}\mu_i(\boldsymbol{x},t)-\rho_{0,0}^{-1}\mu_0(\boldsymbol{x},t)+(\rho_{0,i}^{-1}-\rho_{0,0}^{-1})p(\boldsymbol{x},t)\right)\quad i=1,2,\ldots,N \tag{2.48}$$

$$\mu_i(\boldsymbol{x},t)=\frac{\partial f_h(\boldsymbol{\phi})}{\partial\phi_i}-\epsilon_i^2\Delta\phi_i(\boldsymbol{x},t)\quad i=1,2,\ldots,N \tag{2.49}$$

$$-\sum_{i=0}^{N}\nabla\cdot\left(\gamma_i\phi_i^2(\boldsymbol{x},t)\nabla\left(\mu_i(\boldsymbol{x},t)+p(\boldsymbol{x},t)\right)\right)=\sum_{i=1}^{N}\left(\rho_{0,i}^{-1}-\rho_{0,0}^{-1}\right)S_i(\boldsymbol{x},t). \tag{2.50}$$

2.2.2 A Change of Variables

While equations for ϕ_0, μ_0 have been eliminated from the system (2.34) and (2.35), μ_0 is still present in the model through the pressure Poisson equation and the source terms. Thus for simulations one must compute μ_0 as the equations are currently written, which can be done through the no voids constraint. So as to eliminate this requirement computationally, consider the proposed change of variables

$$\widetilde{p}(\boldsymbol{x},t)=\mu_0(\boldsymbol{x},t)+p(\boldsymbol{x},t)\quad\text{and}\quad\widetilde{\mu}_i(\boldsymbol{x},t)=\mu_i(\boldsymbol{x},t)-\mu_0(\boldsymbol{x},t)\text{ for }i=1,2,\ldots,N \tag{2.51}$$

In the equations (2.47) - (2.50) the terms $\mu_i(\boldsymbol{x},t)+p(\boldsymbol{x},t)$ remain unchanged, as

$$\begin{aligned}\mu_i(\boldsymbol{x},t)+p(\boldsymbol{x},t)&=\mu_i(\boldsymbol{x},t)-\mu_0(\boldsymbol{x},t)+\mu_0(\boldsymbol{x},t)+p(\boldsymbol{x},t)\\&=\widetilde{\mu}_i(\boldsymbol{x},t)+\widetilde{p}(\boldsymbol{x},t).\end{aligned} \tag{2.52}$$

Also, for the source terms we have that

$$\begin{aligned} S_i(\boldsymbol{x},t) &= -\lambda\left(\rho_{0,i}^{-1}\mu_i(\boldsymbol{x},t) - \rho_{0,0}^{-1}\mu_0(\boldsymbol{x},t) + \rho_{0,i}^{-1}p(\boldsymbol{x},t) - \rho_{0,0}^{-1}p(\boldsymbol{x},t)\right) \\ &= -\lambda\left(\rho_{0,i}^{-1}\mu_i(\boldsymbol{x},t) + \rho_{0,i}^{-1}p(\boldsymbol{x},t) - \rho_{0,0}^{-1}\widetilde{p}(\boldsymbol{x},t)\right) \\ &= -\lambda\left(\rho_{0,i}^{-1}\widetilde{\mu}_i(\boldsymbol{x},t) + \rho_{0,i}^{-1}\widetilde{p}(\boldsymbol{x},t) - \rho_{0,0}^{-1}\widetilde{p}(\boldsymbol{x},t)\right). \end{aligned} \tag{2.53}$$

The boundary conditions for these solution variables are similar to that of the old variables, as through some computations we see

$$\begin{aligned} -\nabla\widetilde{p}(\boldsymbol{x},t)\cdot\boldsymbol{n} &= -\nabla\left(\mu_0(\boldsymbol{x},t) + p(\boldsymbol{x},t)\right)\cdot\boldsymbol{n} \\ &= \beta(\mu_0(\boldsymbol{x},t) + p(\boldsymbol{x},t)) \quad \text{by (2.39)} \\ &= \beta\widetilde{p}(\boldsymbol{x},t) \end{aligned} \tag{2.54}$$

and similarly for μ_i

$$\begin{aligned} -\nabla\widetilde{\mu}_i(\boldsymbol{x},t)\cdot\boldsymbol{n} &= -\nabla\left(\mu_i(\boldsymbol{x},t) - \mu_0(\boldsymbol{x},t)\right)\cdot\boldsymbol{n} \\ &= -\nabla\mu_i(\boldsymbol{x},t)\cdot\boldsymbol{n} + \nabla\mu_0(\boldsymbol{x},t)\cdot\boldsymbol{n} \\ &= \beta_i\mu_i(\boldsymbol{x},t) + (\beta_i - \beta)p(\boldsymbol{x},t) - \beta\mu_0 \\ &= \beta_i(\mu_i - \mu_0) + (\beta_i - \beta)(\mu_0 + p) \quad \text{after adding } \pm\beta_i\mu_0(\boldsymbol{x},t) \text{ to the last line} \\ &= \beta_i\widetilde{\mu}_i(\boldsymbol{x},t) + (\beta_i - \beta_0)\widetilde{p}(\boldsymbol{x},t) \end{aligned} \tag{2.55}$$

Again, note that for any no-flow components we have $\beta_i = 0$ and

$$\begin{aligned} -\nabla\widetilde{\mu}_i(\boldsymbol{x},t)\cdot\boldsymbol{n} &= -\beta\widetilde{p}(\boldsymbol{x},t) \\ &= \nabla\widetilde{p}(\boldsymbol{x},t)\cdot\boldsymbol{n}. \end{aligned} \tag{2.56}$$

All that is left is to modify the equations for the chemical potentials by

$$\begin{aligned}\widetilde{\mu}_i(\boldsymbol{x},t) &= \mu_i(\boldsymbol{x},t) - \mu_0(\boldsymbol{x},t) \\ &= \frac{\partial f_h(\boldsymbol{\phi})}{\partial \phi_i} - \frac{\partial f_h(\boldsymbol{\phi})}{\partial \phi_0} - \epsilon_i^2 \Delta\phi_i(\boldsymbol{x},t) + \epsilon_0^2 \Delta\phi_0(\boldsymbol{x},t) \\ &= \frac{\partial f_h(\boldsymbol{\phi})}{\partial \phi_i} - \frac{\partial f_h(\boldsymbol{\phi})}{\partial \phi_0} - \epsilon_i^2 \Delta\phi_i(\boldsymbol{x},t) + \epsilon_0^2 \Delta\left(1 - \sum_{j\neq 0} \phi_j(\boldsymbol{x},t)\right) \quad \text{by (2.13)} \\ &= \frac{\partial f_h(\boldsymbol{\phi})}{\partial \phi_i} - \frac{\partial f_h(\boldsymbol{\phi})}{\partial \phi_0} - \epsilon_i^2 \Delta\phi_i(\boldsymbol{x},t) - \sum_{j\neq 0} \epsilon_0^2 \Delta\phi_j(\boldsymbol{x},t).\end{aligned} \tag{2.57}$$

Additionally, the terms

$$\frac{\partial f_h(\boldsymbol{\phi})}{\partial \phi_i} - \frac{\partial f_h(\boldsymbol{\phi})}{\partial \phi_0} \tag{2.58}$$

can be more compactly written in terms of the homogeneous free energy composed with the no voids constraint. We define

$$\widetilde{f}_h(\{\phi_k\}_{k\neq 0}) = f_h\left(1 - \sum_{i\neq 0} \phi_i, \phi_1, \phi_2, \ldots, \phi_N\right) \tag{2.59}$$

and we recognize via the chain rule

$$\frac{\partial \widetilde{f}_h(\{\phi_k\}_{k\neq 0})}{\partial \phi_i} = \frac{\partial f_h(\boldsymbol{\phi})}{\partial \phi_i} - \frac{\partial f_h(\boldsymbol{\phi})}{\partial \phi_0} \quad i \neq 0. \tag{2.60}$$

Abusing the notation for $\boldsymbol{\phi}$, we write

$$\widetilde{f}_h(\boldsymbol{\phi}) = \widetilde{f}_h(\{\phi_k\}_{k\neq 0}). \tag{2.61}$$

With these substitutions, the equations to be solved numerically are

$$\frac{\partial \phi_i(\boldsymbol{x},t)}{\partial t} - \nabla \cdot \left(\gamma_i \phi_i^2(\boldsymbol{x},t) \nabla \left(\widetilde{\mu}_i(\boldsymbol{x},t) + \widetilde{p}(\boldsymbol{x},t)\right)\right) = \rho_{0,i}^{-1} S_i(\boldsymbol{x},t) \tag{2.62}$$

$$\widetilde{\mu}_i(\boldsymbol{x},t) = \frac{\partial \widetilde{f}_h(\boldsymbol{\phi})}{\partial \phi_i} - \epsilon_i^2 \Delta\phi_i(\boldsymbol{x},t) - \sum_{j\neq 0} \epsilon_0^2 \Delta\phi_j(\boldsymbol{x},t). \tag{2.63}$$

$$S_i = -\lambda \left(\rho_{0,i}^{-1} \widetilde{\mu}_i(\boldsymbol{x},t) + \rho_{0,i}^{-1} \widetilde{p}(\boldsymbol{x},t) - \rho_{0,0}^{-1} \widetilde{p}(\boldsymbol{x},t)\right). \tag{2.64}$$

with the pressure Poisson equation

$$-\sum_{i=0}^{N}\nabla\cdot\left(\gamma_i\phi_i^2(\boldsymbol{x},t)\nabla\widetilde{p}(\boldsymbol{x},t)\right)-\sum_{i=1}^{N}\nabla\cdot\left(\gamma_i\phi_i^2(\boldsymbol{x},t)\nabla\widetilde{\mu}_i(\boldsymbol{x},t)\right)=\sum_{i=1}^{N}\left(\rho_{0,i}^{-1}-\rho_{0,0}^{-1}\right)S_i(\boldsymbol{x},t). \tag{2.65}$$

Note that the second sum excludes $i=0$, as the continuity equation for the zeroth component now reads

$$\frac{\partial\phi_0(\boldsymbol{x},t)}{\partial t}-\nabla\cdot\left(\gamma_0\phi_i^2(\boldsymbol{x},t)\nabla\left(\widetilde{p}(\boldsymbol{x},t)\right)\right)=\rho_{0,0}^{-1}\left[-\sum_{i=1}^{N}S_i(\boldsymbol{x},t)\right]. \tag{2.66}$$

Lastly, we include the boundary conditions

$$-\nabla\widetilde{p}(\boldsymbol{x},t)\cdot\boldsymbol{n}=\beta\widetilde{p}(\boldsymbol{x},t), \tag{2.67}$$

$$-\nabla\widetilde{\mu}_i(\boldsymbol{x},t)\cdot\boldsymbol{n}=\beta_i\widetilde{\mu}_i(\boldsymbol{x},t)+(\beta_i-\beta)\widetilde{p}(\boldsymbol{x},t) \tag{2.68}$$

and the no voids constraint

$$\phi_{sv}(\boldsymbol{x},t)=1-\sum_{i\neq sv}\phi_i(\boldsymbol{x},t). \tag{2.69}$$

2.3 The Flory Huggins Free Energy

The qualitative behavior of the time evolution of the solution is greatly influenced by the homogeneous free energy density f_h, and in the context of polymers a commonly used free energy is the Flory-Huggins homogeneous free energy density, which will be considered in this dissertation. Let $N_i,\rho_{0,i}$ be the polymer chain lengths and number densities, respectively. The Flory-Huggins energy for a binary mixture

$$\frac{f_h(\phi_0,\phi_1)}{kT}=\frac{\rho_{0,0}\phi_0}{N_0}\ln(\phi_0)+\frac{\rho_{0,1}\phi_1}{N_1}\ln\phi_1+\chi_{01}(\phi_0)(\phi_1) \tag{2.70}$$

so that

$$\frac{\widetilde{f}_h(\phi_1)}{kT}=\frac{\rho_{0,0}(1-\phi_1)}{N_0}\ln(1-\phi_1)+\frac{\rho_{0,1}\phi_1}{N_1}\ln\phi_1+\chi_{01}(\phi_0)(\phi_1) \tag{2.71}$$

which is plotted for various values of χ_{01} in Figure 2.1, assuming for now that $\rho_{0,0} = \rho_{0,1} = N_0 = N_1 = 1$. For values of χ_{01} greater than 2, for these parameters one can show via elementary calculus that the Flory-Huggins energy assumes a double-well potential. As the interaction parameter χ_{01} increases, the homogeneous free energy's minima will be located closer and closer to $\phi_1 = 0, 1$. This will cause the solution to phase separate into purer components since these states are more energetically favorable. The $N + 1$ component Flory-Huggins energy reads

$$\frac{f_h(\boldsymbol{\phi})}{kT} = \sum_{i=0}^{N} \frac{\rho_i \phi_i}{N_i} \ln \phi_i + \sum_{i \neq j} \chi_{ij} \phi_i \phi_j \tag{2.72}$$

This function, for a ternary system, is plotted on a Gibbs Triangle, as shown in Figure 2.2 and 2.3, since the no voids assumption (2.13) holds. In upcoming applications, qualitatively we identify pure component 0 to be energetically favorable. In order to ensure this, we introduce the term $-c \cdot \phi_0$ to the free energy, which modifies the free energy to

$$f_h(\phi_0, \phi_1, \phi_2) = \sum_{i} \frac{\rho_i \phi_i}{N_i} \ln \phi_i + \sum_{i \neq j} \chi_{ij} \phi_i \phi_j - c \cdot \phi_0. \tag{2.73}$$

The effect of this term is readily seen the plot of the free energy located in Figure 2.3, as the minimum of the function is clearly located near $\phi_0 \approx 1$.

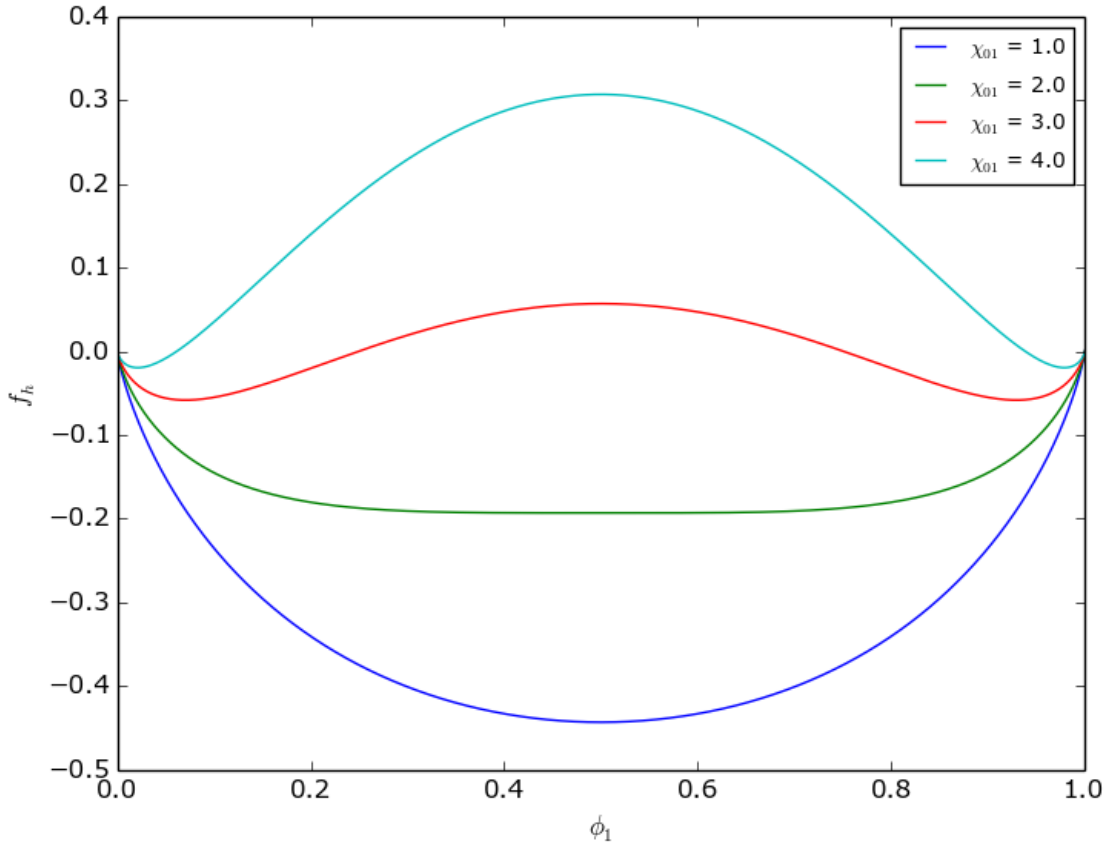

Figure 2.1: The binary free energy with varying Flory interaction parameter χ_{01} is shown with fixed parameters $\rho_0 = \rho_1 = N_0 = N_1 = 1.0$. As the Flory interaction parameter is increased, the Flory-Huggins free energy assumed a double-well potential, with minima ϕ_1 approaching 0 and 1.

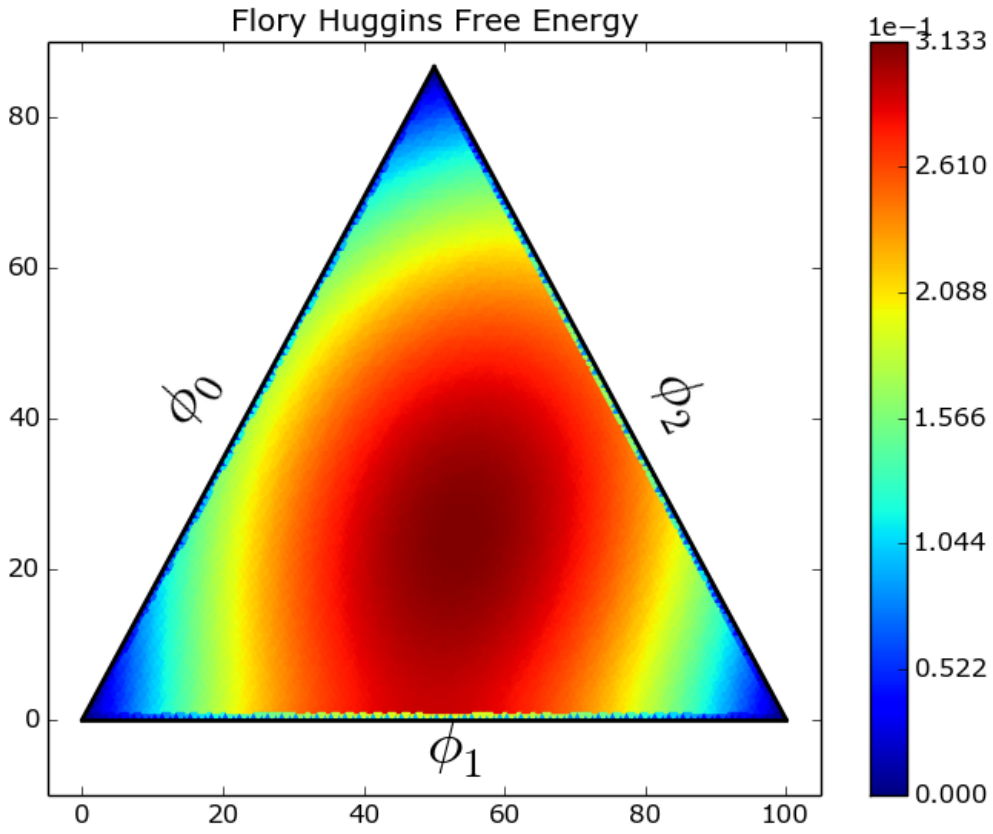

Figure 2.2: The ternary, unmodified Flory Huggins free energy is plotted with parameters $\rho_0 = .001$, $\rho_1 = \rho_2 = 1.0, \chi_{01} = \chi_{02} = 1.2$, $\chi_{12} = .9$. Note the comparison with 2.3, where the free energy minimum is located near $\phi_0 \approx 1$.

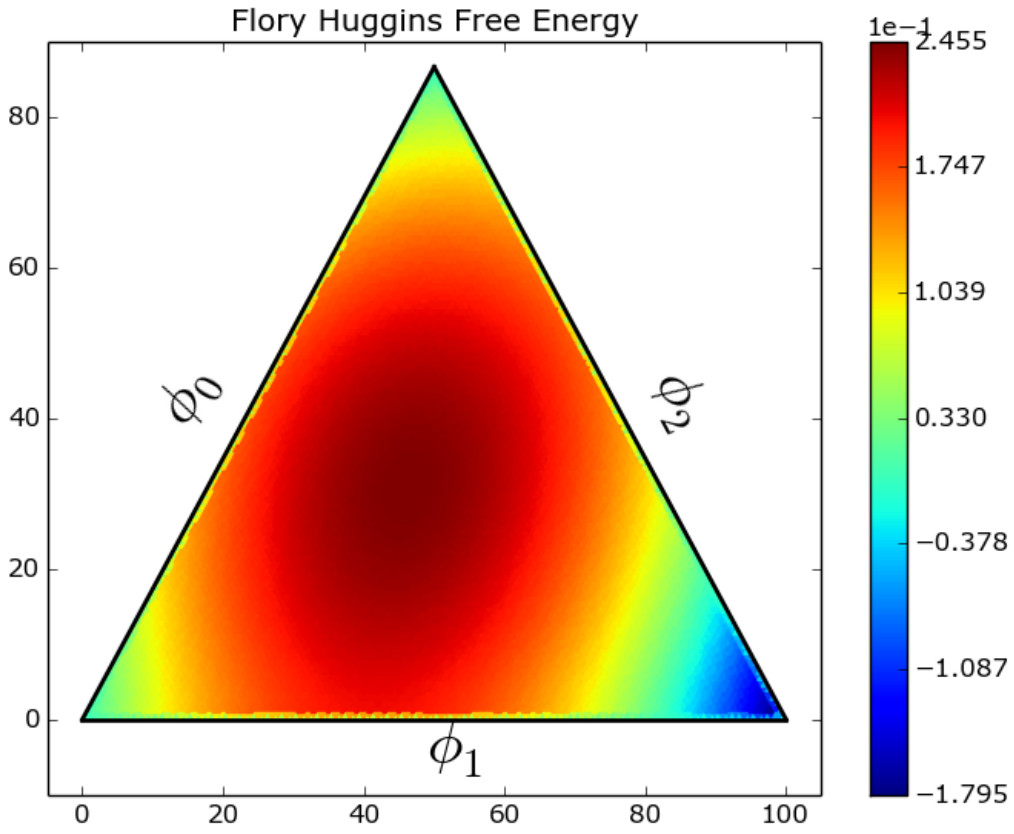

Figure 2.3: The ternary, modified Flory Huggins free energy is plotted with parameters $\rho_0 = 0.001$, $\rho_1 = \rho_2 = 1.0, \chi_{01} = \chi_{02} = 1.2$, $\chi_{12} = 0.9, c = 0.2$. Here, the free energy has minimum located at $\phi_0 \approx 1$ so that the solution energetically driven to be in the vapor phase.

2.4 Other Models

We have previously remarked that there are many choices for constitutive equations which dissipate the free energy, referring to (2.31), and we previously have examined the Darcy-like choices for the constitutive equations (2.32). There are a wealth of choices here that dissipate the energy, including various types of physics such as drag against a barycentric velocity, drag of one component against another, viscous effects, as well as many others. All of these have the common feature of prescribing some dissipation of the energy and deriving constitutive equations for the velocities which result in this dissipation [19, 18, 49]. We consider now other possibilities for the velocities to demonstrate the other physics that can be included.

2.4.1 A Cross-Diffusion Model

Recall we have from Equation (2.30)

$$\frac{dE}{dt} = \sum_{i=0}^{N} \int_{\Omega} \boldsymbol{Q}_i \cdot \boldsymbol{u}_i \, d\boldsymbol{x} - \sum_{i=0}^{N} \int_{\partial\Omega} r_i \, \boldsymbol{u}_i \cdot \boldsymbol{n} dS + \sum_{i=0}^{N} \int_{\Omega} q_i \, S_i \, d\boldsymbol{x}. \tag{2.74}$$

Define $\boldsymbol{Q}_i^r \in \mathbb{R}$ to be the rth component of $\boldsymbol{Q}_i$, and similarly for $\boldsymbol{u}_i^r$. Suppose that K is a symmetric, positive definite matrix with entries κ_{ij}, and suppose the constitutive relation

$$\boldsymbol{u}_i^r = -\sum_j \kappa_{ij} \boldsymbol{Q}_j^r. \tag{2.75}$$

Then

$$\begin{aligned} \int_{\Omega} \sum_{i=0}^{N} \boldsymbol{Q}_i \cdot \boldsymbol{u}_i d\boldsymbol{x} &= \int_{\Omega} \sum_{i=0}^{N} \sum_{r=1}^{d} \boldsymbol{Q}_i^r \cdot \boldsymbol{u}_i^r d\boldsymbol{x} \\ &= -\int_{\Omega} \sum_{i=0}^{N} \sum_{r=1}^{d} \boldsymbol{Q}_i^r \cdot \sum_{j=0}^{N} \kappa_{ij} \boldsymbol{Q}_j^r d\boldsymbol{x} \\ &= -\int_{\Omega} \sum_{r=1}^{d} \left(\sum_{i=0}^{N} \boldsymbol{Q}_i^r \cdot \sum_{j=0}^{N} \kappa_{ij} \boldsymbol{Q}_j^r \right) d\boldsymbol{x}. \end{aligned} \tag{2.76}$$

In a similar manner, for the other terms in (2.74) define W, $\Lambda \in \mathbb{R}^{(N+1)\times(N+1)}$ and $\boldsymbol{r}, \boldsymbol{q}$ to be the vectors with ith component r_i, q_i. Let $[W\boldsymbol{r}]_i, [\Gamma\boldsymbol{q}]_i$ be the ith component of $W\boldsymbol{r}$. Then set

$$\begin{aligned} \boldsymbol{u}_i \cdot \boldsymbol{n} &= [W\boldsymbol{r}]_i \\ S_i &= -[\Lambda \boldsymbol{q}]_i. \end{aligned} \tag{2.77}$$

If W, Λ are symmetric, positive definite matrices, then this will yield an energy dissipation

$$\frac{dE}{dt} = -\int_\Omega \sum_{r=1}^{d} \left(\sum_{i=0}^{N} \boldsymbol{Q}_i^r \cdot \sum_{j=0}^{N} \kappa_{ij} \boldsymbol{Q}_j^r \right) d\boldsymbol{x} - \int_{\partial\Omega} \boldsymbol{r} \cdot W\boldsymbol{r} dS - \int_\Omega \boldsymbol{q} \cdot \Lambda \boldsymbol{q} d\boldsymbol{x}. \tag{2.78}$$

2.4.2 A Darcy Drag Model

Consider a model where we require that the energy decreases as

$$\sum_{i=0}^{N} \int_\Omega \boldsymbol{Q}_i \cdot \boldsymbol{u}_i \, d\boldsymbol{x} = -\frac{1}{2} \sum_{i=0}^{N} \sum_{j=0}^{N} \int_\Omega \gamma_{i,j} \, |\boldsymbol{u}_i - \boldsymbol{u}_j|^2 \, d\boldsymbol{x}, \tag{2.79}$$

where $[\gamma_{i,j}] \in \mathbb{R}^{N+1\times N+1}$ is a symmetric matrix with positive entries. We can expand the right hand side of (2.79) to

$$\begin{aligned} &-\frac{1}{2} \sum_{i=0}^{N} \sum_{j=0}^{N} \int_\Omega \gamma_{i,j} \, |\boldsymbol{u}_i - \boldsymbol{u}_j|^2 \, d\boldsymbol{x} \\ &= -\frac{1}{2} \sum_{i=0}^{N} \sum_{j=0}^{N} \int_\Omega \gamma_{ij} \boldsymbol{u}_i (\boldsymbol{u}_i - \boldsymbol{u}_j) - \gamma_{ij} \boldsymbol{u}_j (\boldsymbol{u}_i - \boldsymbol{u}_j) d\boldsymbol{x} \\ &= -\frac{1}{2} \sum_{i=0}^{N} \sum_{j=0}^{N} \int_\Omega \gamma_{ij} \boldsymbol{u}_i (\boldsymbol{u}_i - \boldsymbol{u}_j) d\boldsymbol{x} + \frac{1}{2} \sum_{i=0}^{N} \sum_{j=0}^{N} \int_\Omega \gamma_{ij} \boldsymbol{u}_j (\boldsymbol{u}_i - \boldsymbol{u}_j) d\boldsymbol{x} \\ &= -\frac{1}{2} \sum_{i=0}^{N} \sum_{j=0}^{N} \int_\Omega \gamma_{ij} \boldsymbol{u}_i (\boldsymbol{u}_i - \boldsymbol{u}_j) d\boldsymbol{x} - \frac{1}{2} \sum_{i=0}^{N} \sum_{j=0}^{N} \int_\Omega \gamma_{ij} \boldsymbol{u}_j (\boldsymbol{u}_j - \boldsymbol{u}_i) d\boldsymbol{x}. \end{aligned} \tag{2.80}$$

By the symmetry of γ_{ij}, the second term in the last line of (2.80) is the same as the first, and so

$$\begin{aligned} &-\frac{1}{2}\sum_{i=0}^{N}\sum_{j=0}^{N}\int_{\Omega}\gamma_{i,j}\ |\boldsymbol{u}_i-\boldsymbol{u}_j|^2\ d\boldsymbol{x} \\ &=-\sum_{i=0}^{N}\sum_{j=0}^{N}\int_{\Omega}\gamma_{ij}\boldsymbol{u}_i\left(\boldsymbol{u_i}-\boldsymbol{u}_j\right)d\boldsymbol{x}. \end{aligned} \tag{2.81}$$

This implies for this energy dissipation that we should choose

$$\boldsymbol{Q}_i=-\sum_{j=0}^{N}\gamma_{ij}\left(\boldsymbol{u}_i-\boldsymbol{u}_j\right). \tag{2.82}$$

Chapter 3

Application: Modeling of Solvent Evaporation in Phase Separating Polymer Blends

Preparation of thin films by dissolving polymers in a common solvent followed by evaporation of the solvent has become a routine procedure. In this work, we present a methodology based on the free energy of dissipation, which allows systematic study of various effects such as the changes in the solvent properties due to transformation of its phase from liquid to vapor and polymer thermodynamics on the thin film formation. The methodology allows derivation of evaporative flux and boundary conditions near each surface for simulations of systems close to the equilibrium. The methodology is applied to study the thin film formation in phase segregating polymer blends dissolved in a common volatile solvent and deposited on a planar substrate. Effects of the evaporation rates and interactions of the polymers with the underlying substrate on the kinetics of thin film formation are studied.

Evaporation of liquid molecules is ubiquitous in nature and used in a number of applications including coatings [44, 29], organic electronics [9, 2] . Evaporation of liquids involves various non-equilibrium processes [15] coupled with the ones related to the equilibrium. For example, evaporation of any liquid involves phase transformation (which is an equilibrium concept) from liquid to vapor coupled with the transport (which is a non-equilibrium concept) of the molecules across liquid-vapor interface. Modeling of the

evaporation must take into account the coupling between the equilibrium and the non-equilibrium phenomena in an accurate manner. Need for accurate models providing insights into the evaporation for various phenomena occurring in nature and engineering cannot be overstated. The accurate models can help many engineering processes cost-effective and better by providing fundamental understanding of various processes involved in the evaporation.

A number of so-called moving boundary models [16, 27, 35, 46, 37, 47, 57, 30, 43, 39, 58, 40, 10, 38] have been developed and reported in the literature treating various aspects of the solvent evaporation within different levels of accuracy. A common aspect in almost all of these models is the treatment of the solvent evaporative flux in an *ad hoc* manner. Broadly, we can categorize these models into two classes. In one class of models, transport of the evaporating molecules across the liquid-vapor interface is treated by simply moving the liquid-vapor interface based on the local velocity of the evaporating molecules [35, 46, 37, 47, 57, 43, 58, 38] or simply removing the evaporating molecules at a given rate [30] In the other class of models, various expressions of the evaporative fluxes are either *assumed* [39] or derived [27, 16] based on the assumed shape and motion of the liquid-vapor interface. The boundary conditions are either taken to mimic a specific system [16, 27, 57, 42] or derived based on the balance of mass, energy and momentum at the interfaces. Although these models provide useful insights into various processes resulting from the moving liquid-vapor interface leading to an increase in density inside the film, there is no systematic methodology to improve on the shortcomings related to details of the liquid-vapor interface and the evaporative fluxes. Particle based simulations such as those based on the classical (Newtonian) molecular dynamics [51, 41, 36, 11] have been used to obtain additional insights. However, in case of processes occurring at widely disparate length and time scales (e.g., in the case of polymeric systems), particle based simulations become computationally expensive and sometimes challenging to execute.

Details of the liquid-vapor interface as well as the evaporative flux are the most important features, which need to be modeled in an accurate way. Experimental work on small molecular liquids such as water and ethanol provides some of the details. In particular, work by Ward et al [53, 52] has provided information about the details of the liquid-vapor

interfaces for solvents like water and ethanol. Experimentally, it has been shown that there is a discontinuity in temperature near the liquid-vapor interface, with the vapor phase having *higher* temperature than the liquid. For water, the temperature difference can be as high as 7.8 K. A statistical rate theory based on the concept of transition probability was used to derive an expression for the evaporative flux [53]. The expression was used to estimate the coefficients, which appear in the Hertz-Knudsen-Schrage relations for the evaporative flux based on the classical kinetic theory of gases [3]. These works [53, 52] have highlighted the importance of interfacial entropy production in the evaporation. A systematic method for solvent evaporation can be constructed using the ideas of irreversible thermodynamics for the systems close to the equilibrium. This can be realized in experiments, for example, when solvent evaporation is mainly used as a method for overcoming the free energy barriers to reach the global free energy minimum state characterizing the equilibrium. Solvent annealing for block copolymers [29] is an example.

In this application, we have developed a methodology to study solvent evaporation in multicomponent systems based on the concepts of irreversible thermodynamics [15]. The methodology is limited to the systems close to the equilibrium. However, it is quite general and allows systematic investigations of various non-trivial effects. For example, the methodology allows identification of a self-consistent expression for the evaporative flux and boundary conditions. Furthermore, the methodology simulates structure and dynamics of the liquid-vapor interface in a self-consistent manner rather than assuming a flat interface such as done in the models based on the Hertz-Knudsen-Schrage relations for the evaporative flux.

3.1 The Mathematical Model

We derive a thermodynamically consistent model for the time evolution of a quaternary vapor-solvent-polymer-polymer mixture where the solvent is volatile and evaporating into the vapor phase using energetic variational princicples and mass conservation laws described in Chapter 2. What results is a set of 3 coupled Cahn-Hilliard, Allen-Cahn-like equations along with a Poisson-like equation for the pressure.

Consider a mixture of two polymers (p and q) and solvent which can be present in the liquid phase (sl) or in the vapor phase (sv). Define $I = \{p, q, sl, sv\}$. Then for $i \in I$ we enforce the conservation of mass through the continuity equation

$$\frac{\partial \rho_i(\boldsymbol{x}, t)}{\partial t} + \nabla \cdot (\rho_i(\boldsymbol{x}, t)\boldsymbol{u}_i(\boldsymbol{x}, t)) = S_i(\boldsymbol{x}, t) \tag{3.1}$$

where $\rho_i(\boldsymbol{x}, t)$ is the number density of the ith component of the mixture and $S_i(\boldsymbol{x}, t)$ is a source term which will allow solvent molecules in the liquid phase to become solvent in the vapor phase, modeling the evaporation of the volatile solvent. We assume that this density function can be written as (2.3) and so

$$\frac{\partial \phi_i(\boldsymbol{x}, t)}{\partial t} + \nabla \cdot (\phi_i(\boldsymbol{x}, t)\boldsymbol{u}(\boldsymbol{x}, t)) = \rho_{0,i}^{-1} S_i(\boldsymbol{x}, t) \quad i \in I. \tag{3.2}$$

We also assume that there are no voids in the mixture so that

$$\sum_{i \in I} \phi_i(\boldsymbol{x}, t) \equiv 1 \tag{3.3}$$

and thus one of the phase variables, for which we choose the solvent in the vapor phase, can be algebraically solved in terms of the others as

$$\phi_{sv}(\boldsymbol{x}, t) = 1 - \sum_{i \neq sv} \phi_i(\boldsymbol{x}, t). \tag{3.4}$$

In this application, since the only source and sinks are due to that of the volatile solvent transitioning into the vapor phase we have that $S_p(\boldsymbol{x}, t) = S_q(\boldsymbol{x}, t) = 0$, and so

$$\begin{aligned} \frac{dM}{dt} &= \int_\Omega \sum_{i \in I} \rho_{0,i} \frac{\partial \phi_i(\boldsymbol{x}, t)}{\partial t} d\boldsymbol{x} \\ &= -\int_{\partial\Omega} \sum_{i \in I} \rho_{0,i} \phi_i(\boldsymbol{x}, t)\boldsymbol{u}_i(\boldsymbol{x}, t) \cdot \boldsymbol{n} dS + \int_\Omega S_{sv}(\boldsymbol{x}, t) + S_{sl}(\boldsymbol{x}, t) d\boldsymbol{x}. \end{aligned} \tag{3.5}$$

and so (2.7) reduces to

$$S_{sv}(\boldsymbol{x}, t) = -S_{sl}(\boldsymbol{x}, t). \tag{3.6}$$

The applicable free energy to this application is the chemical energy

$$E_{\text{chem}}(t) = \int_{\Omega} f_h(\boldsymbol{\phi}(\boldsymbol{x},t)) + \sum_{i\in I} \frac{\epsilon_i^2}{2} |\nabla \phi_i(\boldsymbol{x},t)|^2 d\boldsymbol{x}. \tag{3.7}$$

where $f_h(\boldsymbol{\phi})$ is the logarithmic Flory-Huggins free energy density, which is defined as

$$f_h(\boldsymbol{\phi}) = kT \left(\sum_i \frac{\rho_{0,i}}{N_i} \phi_i(\boldsymbol{x},t) \ln(\phi_i(\boldsymbol{x},t)) + \sum_{i\neq j} \chi_{ij} \phi_i(\boldsymbol{x},t) \phi_j(\boldsymbol{x},t) \right) \tag{3.8}$$

where k is the Boltzmann constant, T is the absolute temperature, χ_{ij} are the Flory interaction parameters between components i and j, and ϵ_i^2 are the gradient energy coefficients. The gradient energy coefficients are derived to be concentration dependent [14], however we assume them to be independent of the volume concentrations ϕ_i.

$$\epsilon_i^2 = \frac{\rho_{0,i} b_i^2 kT}{18} \tag{3.9}$$

is commonly used [45], where b_i is the Kuhn length. After computing the time derivative of the free energy as done in 2.19 we have

$$\begin{aligned} \frac{dE_{\text{chem}}}{dt} &= \sum_{i\in I} \int_{\Omega} \phi_i(\boldsymbol{x},t) \nabla \left(\mu_i(\boldsymbol{x},t) + p(\boldsymbol{x},t) \right) \cdot \boldsymbol{u}_i(\boldsymbol{x},t) dV \\ &+ \int_{\Omega} \left(\rho_{0,sl}^{-1} \mu_{sl}(\boldsymbol{x},t) - \rho_{0,sv}^{-1} \mu_{sv}(\boldsymbol{x},t) + (\rho_{0,sl}^{-1} - \rho_{0,sv}^{-1}) p(\boldsymbol{x},t) \right) S_{sl}(\boldsymbol{x},t) dV \\ &- \sum_{i\in I} \int_{\partial\Omega} \phi_i(\boldsymbol{x},t) \left(\mu_i(\boldsymbol{x},t) + p(\boldsymbol{x},t) \right) \boldsymbol{u}_i(\boldsymbol{x},t) \cdot \boldsymbol{n} dS. \end{aligned} \tag{3.10}$$

We make the definitions

$$\begin{aligned} q_{sl}(\boldsymbol{x},t) &= \rho_{0,sl}^{-1} \mu_{sl}(\boldsymbol{x},t) - \rho_{0,sv}^{-1} \mu_{sv}(\boldsymbol{x},t) + (\rho_{0,sl}^{-1} - \rho_{0,sv}^{-1}) p(\boldsymbol{x},t) \\ \boldsymbol{Q}_i(\boldsymbol{x},t) &= \phi_i(\boldsymbol{x},t) \nabla \left(\mu_i(\boldsymbol{x},t) + p(\boldsymbol{x},t) \right), \quad i \in I \\ r_i(\boldsymbol{x},t) &= \phi_i(\boldsymbol{x},t) \left(\mu_i(\boldsymbol{x},t) + p(\boldsymbol{x},t) \right) \quad i \in I \end{aligned} \tag{3.11}$$

and thus, the free energy of the system decreases as

$$\begin{aligned}\frac{dE_{\text{chem}}}{dt} &= \sum_{i\in I}\int_{\Omega} \boldsymbol{Q}_i(\boldsymbol{x},t)\cdot\boldsymbol{u}_i(\boldsymbol{x},t)dV \\ &+ \int_{\Omega} q_{sl}(\boldsymbol{x},t)S_{sl}(\boldsymbol{x},t)dV \\ &- \sum_{i\in I}\int_{\partial\Omega} r_i(\boldsymbol{x},t)\boldsymbol{u}_i(\boldsymbol{x},t)\cdot\boldsymbol{n}dS.\end{aligned} \tag{3.12}$$

We choose evolution laws for the velocities of this system to be the Darcy-like laws

$$\boldsymbol{u}_i(\boldsymbol{x},t) = -\phi_i(\boldsymbol{x},t)\gamma_i\nabla\left(\mu_i(\boldsymbol{x},t)+p(\boldsymbol{x},t)\right) \quad i\in I \tag{3.13}$$

and the source terms to be

$$S_{sl} = -\lambda\left(\rho_{0,sl}^{-1}\mu_{sl}(\boldsymbol{x},t) - \rho_{0,sv}^{-1}\mu_{sv}(\boldsymbol{x},t) + (\rho_{0,sl}^{-1}-\rho_{0,sv}^{-1})p(\boldsymbol{x},t)\right). \tag{3.14}$$

where γ_i, λ are positive constants, though could be positive operators more generally. In fact, we later use

$$\gamma_i = C\frac{\phi_{sl}}{\phi_i} \quad C>0 \tag{3.15}$$

to introduce a solvent dependent degenerate mobility that kinetically freezes the polymer mixture once the solvent has been completely removed from the system, as then the continuity equations for the polymers become

$$\frac{\partial\phi_i(\boldsymbol{x},t)}{\partial t} - \nabla\cdot\left(C\phi_{sl}\phi_i(\boldsymbol{x},t)\nabla\left(\mu_i(\boldsymbol{x},t)+p(\boldsymbol{x},t)\right)\right) = 0 \quad i=p,q. \tag{3.16}$$

Since the polymer mixture is typically deposited on some substrate which prevents outflow, we require the no-flow boundary conditions for the velocities on the bottom boundary. The top boundary, however, is an open boundary, and so we choose a law

$$\boldsymbol{u}_i(\boldsymbol{x},t)\cdot\boldsymbol{n} = \begin{cases}\omega_i r_i(\boldsymbol{x},t) & \text{on } \partial\Omega_{top} \\ 0 & \text{on } \partial\Omega_{bottom}\end{cases} \tag{3.17}$$

where ω_i is some positive operator. With these constitutive equations in hand we can eliminate the velocities and sources and write the governing equations purely in terms of the functions ϕ_i, μ_i, p as

$$\begin{aligned}&\frac{\partial \phi_{sv}(\boldsymbol{x},t)}{\partial t} - \nabla \cdot \left(\gamma_{sv}\phi_{sv}^2(\boldsymbol{x},t)\nabla\left(\mu_{sv}(\boldsymbol{x},t) + p(\boldsymbol{x},t)\right)\right) \\ &= \rho_{0,sv}^{-1}\lambda\left(\rho_{0,sl}^{-1}\mu_{sl}(\boldsymbol{x},t) - \rho_{0,sv}^{-1}\mu_{sv}(\boldsymbol{x},t) + (\rho_{0,sl}^{-1} - \rho_{0,sv}^{-1})p(\boldsymbol{x},t)\right)\end{aligned} \tag{3.18}$$

$$\begin{aligned}&\frac{\partial \phi_{sl}(\boldsymbol{x},t)}{\partial t} - \nabla \cdot \left(\gamma_{sl}\phi_{sl}^2(\boldsymbol{x},t)\nabla\left(\mu_{sl}(\boldsymbol{x},t) + p(\boldsymbol{x},t)\right)\right) \\ &= -\rho_{0,sl}^{-1}\lambda\left(\rho_{0,sl}^{-1}\mu_{sl}(\boldsymbol{x},t) - \rho_{sv}^{-1}\mu_{sv}(\boldsymbol{x},t) + (\rho_{0,sl}^{-1} - \rho_{sv}^{-1})p(\boldsymbol{x},t)\right)\end{aligned} \tag{3.19}$$

$$\frac{\partial \phi_i(\boldsymbol{x},t)}{\partial t} - \nabla \cdot \left(\gamma_i\phi_i^2(\boldsymbol{x},t)\nabla\left(\mu_i(\boldsymbol{x},t) + p(\boldsymbol{x},t)\right)\right) = 0 \quad i \neq sl, sv \tag{3.20}$$

$$\mu_i(\boldsymbol{x},t) = \frac{\partial f_h(\boldsymbol{\phi}}{\partial \phi_i} - \epsilon_i^2\Delta\phi_i(\boldsymbol{x},t). \tag{3.21}$$

Having eliminated the velocity $\boldsymbol{u}_i(\boldsymbol{x},t)$, we now specify appropriate boundary conditions for $\mu_i(\boldsymbol{x},t)$ and $p(\boldsymbol{x},t)$. On the left and right side boundaries we have periodic conditions for all variables so as to simulate an infinite domain in this direction. Since the bottom boundary is a no-flow boundary we specify homogeneous Neumann boundary conditions for $\mu_i(\boldsymbol{x},t)$ and $p(\boldsymbol{x},t)$, since if

$$\nabla\mu_i(\boldsymbol{x},t)\cdot\boldsymbol{n} = 0 \text{ and } \nabla p(\boldsymbol{x},t)\cdot\boldsymbol{n} = 0 \tag{3.22}$$

then

$$\boldsymbol{u}_i(\boldsymbol{x},t)\cdot\boldsymbol{n} = \phi_i(\boldsymbol{x},t)\gamma_i\nabla(\mu_i(\boldsymbol{x},t) + p(\boldsymbol{x},t))\cdot\boldsymbol{n} = 0. \tag{3.23}$$

The model must permit solvent in the vapor phase (and perhaps the liquid phase as well) to flux across top boundary, and so we combine (3.13) and (3.17) to obtain appropriate thermodynamically consistent boundary conditions for μ_{sv} and p. We must have that

$$-\nabla(\mu_{sv}(\boldsymbol{x},t) + p(\boldsymbol{x},t))\cdot\boldsymbol{n} = \beta\left(\mu_{sv}(\boldsymbol{x},t) + p(\boldsymbol{x},t)\right) \quad \text{where } \beta = \frac{\omega_{sv}}{\gamma_{sv}}, \tag{3.24}$$

and perhaps a natural way to enforce such a condition is to require the Robin boundary conditions for the variables $\mu_{sv}(\boldsymbol{x}, t)$ and $p(\boldsymbol{x}, t)$

$$-\nabla\mu_{sv}(\boldsymbol{x}, t)\cdot\boldsymbol{n} = \beta\mu_{sv}(\boldsymbol{x}, t) \quad -\nabla p(\boldsymbol{x}, t)\cdot\boldsymbol{n} = \beta p(\boldsymbol{x}, t) \quad \text{on } \partial\Omega_{top}. \tag{3.25}$$

This type of boundary condition is not desired for the polymers in the mixture, however, as the system does not lose or gain mass of the polymer by allowing the polymer to flux through the boundary. To enforce this we use the no flow boundary conditions

$$\boldsymbol{u}_i(\boldsymbol{x}, t)\cdot\boldsymbol{n} = 0 \quad \text{for } i = p, q \tag{3.26}$$

on the top boundary. Either boundary condition may be applicable for the solvent in the liquid phase, and simulations later are shown demonstrating the effect of the choice of this boundary condition. Again, if we enforce the boundary conditions

$$\nabla\mu_i(\boldsymbol{x}, t)\cdot\boldsymbol{n} = -\nabla p(\boldsymbol{x}, t)\cdot\boldsymbol{n} \tag{3.27}$$

for the chemical potential, then this clearly results in the no-flow boundary conditions of the ith component. For the boundary conditions for the solvent in the liquid phase, we either implement the no-flow boundary conditions or the derived boundary conditions

$$-\nabla\mu_{sl}(\boldsymbol{x}, t)\cdot\boldsymbol{n} = \beta_{sl}\mu_{sl} + (\beta_{sl} - \beta)\, p \tag{3.28}$$

Also in the model, we may have that the substrate on which the polymer film is deposited may like or dislike some of the components. In simulations, we assume that this affinity is for one of the polymers, and that is modeled through the energetic boundary energy term

$$f_s(\boldsymbol{\phi}) = \alpha_p\phi_p + \alpha_q\phi_q \tag{3.29}$$

The local thermodynamic equilibrium boundary conditions can be expressed in matrix form as

$$\begin{bmatrix} \epsilon_{sv}^2 + \epsilon_{sl}^2 & \epsilon_{sv}^2 & \epsilon_{sv}^2 \\ \epsilon_{sv}^2 & \epsilon_{sv}^2 + \epsilon_p^2 & \epsilon_{sv}^2 \\ \epsilon_{sv}^2 & \epsilon_{sv}^2 & \epsilon_{sv}^2 + \epsilon_{sv}^2 \end{bmatrix} \begin{bmatrix} \nabla\phi_{sl} \cdot \boldsymbol{n} \\ \nabla\phi_p \cdot \boldsymbol{n} \\ \nabla\phi_q \cdot \boldsymbol{n} \end{bmatrix} = \begin{bmatrix} 0 \\ -\alpha_p \\ -\alpha_q \end{bmatrix}. \tag{3.30}$$

In the specific instance that $\epsilon_i^2 = \epsilon^2$ is a constant and $\alpha_p = -\alpha_q$, this has the unique solution

$$\begin{aligned} \nabla\phi_{sl} \cdot \boldsymbol{n} &= 0 \\ \nabla\phi_p \cdot \boldsymbol{n} &= -\frac{\alpha_p}{\epsilon^2} \\ \nabla\phi_q \cdot \boldsymbol{n} &= -\frac{\alpha_q}{\epsilon^2}. \end{aligned} \tag{3.31}$$

Due to the no voids constraint (3.3), we do not solve the Cahn-Hilliard system associated with the solvent in the vapor phase, and instead derive the pressure Poisson equation as in Chapter 2 to be

$$-\sum_{i\in I} \nabla \cdot \left(\gamma_i \phi_i^2(\boldsymbol{x},t) \nabla \left(\mu_i(\boldsymbol{x},t) + p(\boldsymbol{x},t)\right)\right) = \left(\rho_{0,sl}^{-1} - \rho_{0,sv}^{-1}\right) S_{sl}(\boldsymbol{x},t). \tag{3.32}$$

This reduces the problem to solving the system of equations

$$\begin{aligned} &\frac{\partial \phi_{sl}(\boldsymbol{x},t)}{\partial t} - \nabla \cdot \left(\gamma_{sl} \phi_{sl}^2(\boldsymbol{x},t) \nabla \left(\mu_{sl}(\boldsymbol{x},t) + p(\boldsymbol{x},t)\right)\right) \\ &= -\rho_{0,sl}^{-1} \lambda \left(\rho_{0,sl}^{-1} \mu_{sl}(\boldsymbol{x},t) - \rho_{0,sv}^{-1} \mu_{sv}(\boldsymbol{x},t) + (\rho_{0,sl}^{-1} - \rho_{0,sv}^{-1}) p(\boldsymbol{x},t)\right) \end{aligned} \tag{3.33}$$

$$\frac{\partial \phi_i(\boldsymbol{x},t)}{\partial t} - \nabla \cdot \left(\gamma_i \phi_i^2(\boldsymbol{x},t) \nabla \left(\mu_i(\boldsymbol{x},t) + p(\boldsymbol{x},t)\right)\right) = 0 \quad i \neq sl, sv \tag{3.34}$$

$$\mu_i(\boldsymbol{x},t) = \frac{\partial f_h(\boldsymbol{\phi})}{\partial \phi_i} - \epsilon_i^2 \nabla \phi_i(\boldsymbol{x},t) \quad i = sl, p, q \tag{3.35}$$

After making the change of variables

$$\widetilde{p}(\boldsymbol{x},t) = \mu_{sv}(\boldsymbol{x},t) + p(\boldsymbol{x},t) \quad \text{and} \quad \widetilde{\mu}_i(\boldsymbol{x},t) = \mu_i(\boldsymbol{x},t) - \mu_{sv}(\boldsymbol{x},t) \text{ for } i = p, q, sl \tag{3.36}$$

In equations (3.33) - (3.34) the terms $\mu_i(\boldsymbol{x},t) + p(\boldsymbol{x},t)$ remain unchanged, as $\mu_i(\boldsymbol{x},t) - \mu_0(\boldsymbol{x},t) + \mu_0(\boldsymbol{x},t) + p(\boldsymbol{x},t) = \widetilde{\mu}_i(\boldsymbol{x},t) + \widetilde{p}(\boldsymbol{x},t)$, and the source term expressed in terms of

the changed variables is

$$\begin{aligned} S_{sl}(\boldsymbol{x},t) &= -\lambda\left(\rho_{0,sl}^{-1}\mu_{sl}(\boldsymbol{x},t) - \rho_{0,sv}^{-1}\mu_{sv}(\boldsymbol{x},t) + \rho_{0,sl}^{-1}p(\boldsymbol{x},t) - \rho_{0,sv}^{-1}p(\boldsymbol{x},t)\right) \\ &= -\lambda\left(\rho_{0,sl}^{-1}\mu_{sl}(\boldsymbol{x},t) + \rho_{0,sl}^{-1}p(\boldsymbol{x},t) - \rho_{0,sv}^{-1}\widetilde{p}(\boldsymbol{x},t)\right) \\ &= -\lambda\left(\rho_{0,sl}^{-1}\widetilde{\mu}_{sl}(\boldsymbol{x},t) + \rho_{0,sl}^{-1}\widetilde{p}(\boldsymbol{x},t) - \rho_{0,sv}^{-1}\widetilde{p}(\boldsymbol{x},t)\right). \end{aligned} \tag{3.37}$$

The boundary conditions on the flow portion of the boundary for $\widetilde{\mu}$ and $\widetilde{p}$ read

$$\begin{aligned} -\nabla\widetilde{p}(\boldsymbol{x},t)\cdot\boldsymbol{n} &= -\nabla\left(\mu_0(\boldsymbol{x},t) + p(\boldsymbol{x},t)\right)\cdot\boldsymbol{n} \\ &= \beta(\mu_0(\boldsymbol{x},t) + p(\boldsymbol{x},t)) \quad \text{by (2.39)} \\ &= \beta\widetilde{p}(\boldsymbol{x},t) \end{aligned} \tag{3.38}$$

$$\begin{aligned} -\nabla\widetilde{\mu}_i(\boldsymbol{x},t)\cdot\boldsymbol{n} &= -\nabla\left(\mu_i(\boldsymbol{x},t) - \mu_0(\boldsymbol{x},t)\right)\cdot\boldsymbol{n} \\ &= \beta_i\widetilde{\mu}_i(\boldsymbol{x},t) + (\beta_i - \beta)\widetilde{p}(\boldsymbol{x},t) \quad (2.40) \end{aligned} \tag{3.39}$$

for the flow portion of the boundary, with $\beta_i = 0$ if the ith component is a no-flow component on the flow boundary, as derived in the previous section. The chemical potentials become

$$\begin{aligned} \widetilde{\mu}_i(\boldsymbol{x},t) &= \mu_i(\boldsymbol{x},t) - \mu_{sv}(\boldsymbol{x},t) \\ &= \frac{\partial f_h(\boldsymbol{\phi})}{\partial\phi_i} - \frac{\partial f_h(\boldsymbol{\phi})}{\partial\phi_{sv}} - \epsilon_i^2\Delta\phi_i(\boldsymbol{x},t) - \sum_{j\neq sv}\epsilon_{sv}^2\Delta\phi_j(\boldsymbol{x},t). \end{aligned} \tag{3.40}$$

We can write the terms

$$\frac{\partial f_h(\boldsymbol{\phi})}{\partial\phi_i} - \frac{\partial f_h(\boldsymbol{\phi})}{\partial\phi_{sv}} \tag{3.41}$$

more compactly, and with a slight abuse of notation of $\boldsymbol{\phi}$ we write

$$\frac{\partial\widetilde{f}_h(\boldsymbol{\phi})}{\partial\phi_i} = \frac{\partial f_h(\boldsymbol{\phi})}{\partial\phi_i} - \frac{\partial f_h(\boldsymbol{\phi})}{\partial\phi_{sv}} \quad i \neq sv \tag{3.42}$$

with

$$\widetilde{f}_h(\boldsymbol{\phi}) = f_h(1 - \sum_{i\neq sv}\phi_i, \phi_{sl}, \phi_p, \phi_q). \tag{3.43}$$

With these substitutions, the equations to be solved numerically are

$$\frac{\partial \phi_{sl}(\boldsymbol{x},t)}{\partial t} - \nabla \cdot \left(\gamma_{sl}\phi_{sl}^2(\boldsymbol{x},t)\nabla\left(\widetilde{\mu}_{sl}(\boldsymbol{x},t) + \widetilde{p}(\boldsymbol{x},t)\right)\right) = \rho_{0,sl}^{-1} S_{sl}(\boldsymbol{x},t) \tag{3.44}$$

$$\frac{\partial \phi_{i}(\boldsymbol{x},t)}{\partial t} - \nabla \cdot \left(\gamma_{i}\phi_{i}^2(\boldsymbol{x},t)\nabla\left(\widetilde{\mu}_{i}(\boldsymbol{x},t) + \widetilde{p}(\boldsymbol{x},t)\right)\right) = 0 \quad \text{for } i = p,q \tag{3.45}$$

$$\widetilde{\mu}_i(\boldsymbol{x},t) = \frac{\partial \widetilde{f}_h(\boldsymbol{\phi})}{\partial \phi_i} - \epsilon_i^2 \Delta\phi_i(\boldsymbol{x},t) - \sum_{j\neq sv} \epsilon_{sv}^2 \Delta\phi_j(\boldsymbol{x},t). \tag{3.46}$$

$$S_{sl} = -\lambda\left(\rho_{0,sl}^{-1}\widetilde{\mu}_{sl}(\boldsymbol{x},t) + \rho_{0,sl}^{-1}\widetilde{p}(\boldsymbol{x},t) - \rho_{0,sv}^{-1}\widetilde{p}(\boldsymbol{x},t)\right). \tag{3.47}$$

with the pressure Poisson equation

$$-\sum_i \nabla\cdot\left(\gamma_i\phi_i^2(\boldsymbol{x},t)\nabla\widetilde{p}(\boldsymbol{x},t)\right) - \sum_{i\neq sv}\nabla\cdot\left(\gamma_i\phi_i^2(\boldsymbol{x},t)\nabla\widetilde{\mu}_i(\boldsymbol{x},t)\right) = \left(\rho_{0,sl}^{-1} - \rho_{0,sv}^{-1}\right) S_{sl}(\boldsymbol{x},t) \tag{3.48}$$

with the boundary conditions previously described and the no voids constraint

$$\phi_{sv}(\boldsymbol{x},t) = 1 - \sum_{i\neq sv}\phi_i(\boldsymbol{x},t) \tag{3.49}$$

3.2 Nondimensional Equations

We now turn our attention to nondimensionalizing the equations (3.44) - (3.48), and drop all overbars and tildes in them so that we may use them to indicate nondimensionalized operators and variables. Let L, τ be the characteristic length and time, and let $\widetilde{\boldsymbol{x}}, \widetilde{t}$ be nondimensionalized space and time

$$L\widetilde{\boldsymbol{x}} = \boldsymbol{x} \tag{3.50}$$

$$\tau\tilde{t} = t. \tag{3.51}$$

We write the dimensionless Flory-Huggins free energy as

$$\begin{aligned}\overline{f_h}(\boldsymbol{\phi}) &= \frac{\widetilde{f}_h(\boldsymbol{\phi})}{\rho_{0,sl}kT} \\ &= \sum_i \frac{\widetilde{\rho}_{0,i}}{N_i}\phi_i \ln(\phi_i) + \sum_{i\neq j}\widetilde{\chi}_{ij}\phi_i\phi_j\end{aligned} \tag{3.52}$$

where

$$\widetilde{\rho}_{0,i} = \frac{\rho_{0,i}}{\rho_{0,sl}}, \quad \widetilde{\chi}_{ij} = \frac{\chi_{ij}}{\rho_{0,sl}} \quad \text{and } \phi_{sv} = 1 - \sum_{i\neq sv}\phi_i \tag{3.53}$$

With this definition we have the nondimensional chemical potential

$$\widetilde{\mu}_i(\widetilde{\boldsymbol{x}},\widetilde{t}) = \frac{\mu_i(L\widetilde{\boldsymbol{x}},\tau\widetilde{t})}{\rho_{0,sl}kT} = \frac{\partial \overline{f}_h(\boldsymbol{\phi})}{\partial\phi_i} - \frac{\epsilon_i^2}{\rho_{0,sl}kTL^2}\widetilde{\Delta}\widetilde{\phi}_i(\widetilde{\boldsymbol{x}},\widetilde{t}) - \sum_{j\neq sv}\frac{\epsilon_{sv}^2}{\rho_{0,sl}kTL^2}\widetilde{\Delta}\widetilde{\phi}_j(\widetilde{\boldsymbol{x}},\widetilde{t}) \tag{3.54}$$

and the nondimensional pressure

$$\widetilde{p}(\widetilde{\boldsymbol{x}},\widetilde{t}) = \frac{p(L\widetilde{\boldsymbol{x}},\tau\widetilde{t})}{\rho_{0,sl}kT} \tag{3.55}$$

We define $\widetilde{S}_{sl}(\boldsymbol{x},t)$ so that $\widetilde{S}_{sl}(\boldsymbol{x},t) = \rho_{0,sl}^{-1}S_{sl}(L\widetilde{\boldsymbol{x}},\tau\widetilde{t})$ to introduce the density ratio to the continuity equations. Upon substituting the proposed length and time scaling we have

$$\frac{\partial}{\partial\widetilde{t}}\widetilde{\phi}_{sl}(\widetilde{\boldsymbol{x}},\widetilde{t}) - \widetilde{\nabla}\cdot\left(\frac{\tau}{L^2}\gamma_{sl}\rho_{0,sl}kT\widetilde{\phi}_{sl}^2(\widetilde{\boldsymbol{x}},\widetilde{t})\widetilde{\nabla}\left(\widetilde{\mu}_{sl}(\widetilde{\boldsymbol{x}},\widetilde{t}) + \widetilde{p}(\widetilde{\boldsymbol{x}},\widetilde{t})\right)\right) = \widetilde{\rho}_{0,sl}^{-1}\widetilde{S}_{sl}(\widetilde{\boldsymbol{x}},\widetilde{t}) \tag{3.56}$$

$$\frac{\partial}{\partial\widetilde{t}}\widetilde{\phi}_{i}(\widetilde{\boldsymbol{x}},\widetilde{t}) - \widetilde{\nabla}\cdot\left(\frac{\tau}{L^2}\gamma_{i}\rho_{0,sl}kT\phi_i^2(\widetilde{\boldsymbol{x}},\widetilde{t})\widetilde{\nabla}\left(\mu_i(\widetilde{\boldsymbol{x}},\widetilde{t}) + p(\widetilde{\boldsymbol{x}},\widetilde{t})\right)\right) = 0 \quad \text{for } i = p,q \tag{3.57}$$

where

$$\begin{aligned}\widetilde{S}_{sl}(\widetilde{\boldsymbol{x}},\widetilde{t}) &= -(\tau\lambda\rho_{0,sl}^{-1}kT)\left(\widetilde{\rho}_{0,sl}^{-1}\mu_{sl}(\widetilde{\boldsymbol{x}},\widetilde{t}) + \widetilde{\rho}_{0,sl}^{-1}p(\widetilde{\boldsymbol{x}},\widetilde{t}) - \widetilde{\rho}_{0,sv}^{-1}p(\widetilde{\boldsymbol{x}},\widetilde{t})\right) \\ &= -\widetilde{\lambda}\left(\widetilde{\rho}_{sl}^{-1}\mu_{sl}(\widetilde{\boldsymbol{x}},\widetilde{t}) + \widetilde{\rho}_{sl}^{-1}p(\widetilde{\boldsymbol{x}},\widetilde{t}) - \widetilde{\rho}_{sv}^{-1}p(\widetilde{\boldsymbol{x}},\widetilde{t})\right), \quad \widetilde{\lambda} = \tau\lambda\rho_{0,sl}kT.\end{aligned} \tag{3.58}$$

We set the nondimensionalized length L to be the radius of gyration of the long polymer $R_{gp} = \sqrt{\frac{N_p b_p^2}{6}}$. Upon assuming gradient energy coefficients of the form (3.9), the

nondimensional gradient energy coefficients are

$$\begin{aligned}\widetilde{\epsilon}_i^2 &= \frac{\rho_{0,i} b_i^2 kT}{18 R_{gp}^2 kT \rho_{0,sl}} \\ &= \frac{\widetilde{\rho}_i \widetilde{b}_i}{3N_p}.\end{aligned} \tag{3.59}$$

where $\widetilde{b}_i = \frac{b_i}{b_p}$. So as to approximate an appropriate characteristic time scale, consider simplifying the chemical potential of component i by neglecting terms in the chemical potential so that

$$\rho_{0,sl} kT \widetilde{\mu}_i(\widetilde{\boldsymbol{x}}, \widetilde{t}) \approx \frac{\widetilde{\rho}_i}{N_i}(1 + \ln(\widetilde{\phi}_i(\widetilde{\boldsymbol{x}}, \widetilde{t}))). \tag{3.60}$$

and

$$\nabla \mu_i(\boldsymbol{x}, t) \approx \frac{\widetilde{\rho}_i \rho_{0,sl} kT}{L N_i} \widetilde{\nabla} \widetilde{\mu}_i(\widetilde{\boldsymbol{x}}, \widetilde{t}) \approx \frac{\widetilde{\rho}_i \rho_{0,sl} kT}{L \widetilde{\phi}_i(\boldsymbol{x}, t) N_i} \widetilde{\nabla} \widetilde{\phi}_i(\widetilde{\boldsymbol{x}}, \widetilde{t}). \tag{3.61}$$

With this approximation the Cahn-Hilliard equation resembles the diffusion equation

$$\frac{\partial}{\partial \widetilde{t}} \widetilde{\phi}_i(\widetilde{\boldsymbol{x}}, \widetilde{t}) - \widetilde{\nabla} \cdot \left(\frac{\tau}{L^2} \frac{\widetilde{\rho}_{0,i} \rho_{0,sl} kT \gamma_i \widetilde{\phi}_i(\widetilde{\boldsymbol{x}}, \widetilde{t})}{N_i} \nabla \widetilde{\phi}_i(\widetilde{\boldsymbol{x}}, \widetilde{t}) \right) = 0 \tag{3.62}$$

with diffusivity $D_i = \frac{\widetilde{\rho}_{0,i} \rho_{0,sl} kT \gamma_i \phi_i}{N_i}$. Using the Rouse model from polymer dynamics gives a similar diffusion equation in the form of

$$\frac{\partial}{\partial \widetilde{t}} \widetilde{\phi}_i(\widetilde{\boldsymbol{x}}, \widetilde{t}) - \widetilde{\nabla} \cdot \left(\frac{\tau}{L^2} D_{Ri} \widetilde{\nabla} \widetilde{\phi}_i(\widetilde{\boldsymbol{x}}, \widetilde{t}) \right) \tag{3.63}$$

where

$$D_{Ri} = \frac{kT}{N_i \zeta_i} \tag{3.64}$$

is the diffusion coefficient for the Rouse model with associated time scale

$$\tau_{Ri} = \frac{R_{gi}^2}{D_{Ri}}. \tag{3.65}$$

Assuming that $\phi_i(\boldsymbol{x}, t) = C$ is a constant, we readily identify

$$C \rho_{0,sl} \gamma_i \widetilde{\rho}_i = \frac{1}{\zeta_i}. \tag{3.66}$$

If we choose the time scale to be the Rouse time of polymer p, and the length scale to be the radius of gyration so that

$$\tau = \tau_{Rp} \quad L = R_{gp}, \tag{3.67}$$

upon substituting this time scale into the nondimensional equations we have

$$\begin{aligned} 0 &= \frac{\partial \phi_i(\boldsymbol{x},t)}{\partial t} - \nabla \cdot \left(\frac{\tau}{L^2} \frac{\rho_{0,sl} kT \gamma_i \phi_i(\boldsymbol{x},t) \widetilde{\rho}_i}{N_i} \nabla \phi_i(\boldsymbol{x},t) \right) \\ &= \frac{\partial \phi_i(\boldsymbol{x},t)}{\partial t} - \nabla \cdot \left(\frac{\tau}{R_{gp}^2} D_i \nabla \phi_i(\boldsymbol{x},t) \right) \\ &= \frac{\partial \phi_i(\boldsymbol{x},t)}{\partial t} - \nabla \cdot \left(\frac{D_i}{D_{Rp}} \nabla \phi_i(\boldsymbol{x},t) \right) \end{aligned} \tag{3.68}$$

so that the nondimensional mobilities in the Cahn-Hilliard equations are

$$\frac{D_i}{D_{Rp}} = \frac{N_p \gamma_p}{N_i \gamma_i}. \tag{3.69}$$

For example, a time scale for a diffusivity of $D_p = 10^{-10} \frac{cm^2}{s}$ and radius of gyration $R_g = 1nm$, the time scale τ is on the order of 10^{-4}s.

3.3 Numerical Method

We discretize the system of equations in 2 dimensions for convenience of notation in a cell-centered finite difference framework and remark that the discretization in 3 dimensions is a straightforward extension. Assume a uniform step in space and time of $s, h = h_x = h_y$. Though uniform meshes are not used, in any applied adaptivity the use of structured meshes makes the uniform space step assumption useful. It is well known that explicit methods for multi-component Cahn-Hilliard models suffer a time step restriction of $\Delta t = \mathcal{O}(h^4)$ [28, 12]. Here we consider a semi-implicit method.

3.3.1 The Regularized Logarithm

To improve stability and ensure logarithms are not evaluated for values less than or equal to zero, we regularize the logarithm [4, 5, 28] to be the Taylor expansion of the logarithm

function about δ when $x < \delta$ as

$$\ln_\delta(x) = \begin{cases} \ln(x) & x > \delta \\ \ln(\delta) + 2\frac{x}{\delta} - \frac{x^2}{2\delta^2} - 1.5 & x \leq \delta \end{cases} \tag{3.70}$$

for a small parameter δ which is taken to be 10^{-3} in simulations. This is an approximation to the logarithm function which is C^2 and has the property that on $[\delta, \infty)$ its derivative and second derivative match that of the logarithm function, as

$$\frac{d}{dx} \ln_\delta(x)\Big|_{x=\delta} = \frac{2}{\delta} - \frac{1}{\delta} = \frac{1}{\delta} \tag{3.71}$$

and

$$\frac{d^2}{dx^2} \ln_\delta(x)\Big|_{x=\delta} = -\frac{1}{\delta^2}. \tag{3.72}$$

For all logarithms, we instead use the regularized logarithm (3.70).

We consider the set of nondimensional equations previously derived as

$$\frac{\partial \phi_{sl}}{\partial t} - \nabla \cdot (M_{sl}(\boldsymbol{\phi}) \nabla (\mu_{sl} + p)) = \rho_{0,sl}^{-1} S_{sl} \tag{3.73}$$

$$\frac{\partial \phi_i}{\partial t} - \nabla \cdot (M_i(\boldsymbol{\phi}) \nabla (\mu_i + p)) = 0 \quad \text{for } i = p, q \tag{3.74}$$

$$\mu_i = \frac{\partial f_h(\boldsymbol{\phi})}{\partial \phi_i} - \epsilon_i^2 \Delta \phi_i - \sum_{j \neq sv} \epsilon_{sv}^2 \Delta \phi_j. \tag{3.75}$$

$$S_{sl} = -\lambda \left(\rho_{0,sl}^{-1} \mu_{sl} + \rho_{0,sl}^{-1} p - \rho_{0,sv}^{-1} p \right). \tag{3.76}$$

$$-\sum_{i \in I} \nabla \cdot (M_i(\boldsymbol{\phi}) \nabla p) - \sum_{i \neq sv} \nabla \cdot (M_i(\boldsymbol{\phi}) \nabla \mu_i) = \left(\rho_{0,sl}^{-1} - \rho_{0,sv}^{-1} \right) S_{sl} \tag{3.77}$$

with

$$f_h(\boldsymbol{\phi}) = \sum_{i \in I} \frac{\rho_{0,i}}{N_i} \phi_i \ln_\delta(\phi_i) + \sum_{i \neq j} \chi_{ij} \phi_i \phi_j - c \cdot \phi_{sv} \quad \text{with } \phi_{sv} = 1 - \sum_{i \neq sv} \phi_i. \tag{3.78}$$

The boundary conditions are periodic on the left and right side for all variables. The local thermodynamic equilibrium boundary conditions applied for $\nabla \phi_i \cdot \boldsymbol{n}$ are derived in (3.30),

and for the chemical potentials and pressure we enforce the previously derived boundary conditions for the top boundary

$$-\nabla p(\boldsymbol{x},t)\cdot\boldsymbol{n}=\beta p \quad -\nabla\mu_i(\boldsymbol{x},t)\cdot\boldsymbol{n}=\beta_i\mu_i+(\beta_i-\beta)\,p \tag{3.79}$$

with $\beta_p = \beta_q = 0$, and homogeneous Neumann boundary conditions for all chemical potentials and pressures on the bottom boundary.

3.3.2 A Semi-Implicit Method

In this numerical approximation, we first discretize via a first order method semi-implicitly in time

$$\phi_{sl}^{n+1}-s\nabla\cdot\left(M_{sl}(\boldsymbol{\phi}^n)\nabla\left(\mu_{sl}^{n+1}+p^{n+1}\right)\right)-s\rho_{0sl}^{-1}S_{sl}^{n+1}=\phi_{sl}^{n} \tag{3.80}$$

$$\phi_{i}^{n+1}-s\nabla\cdot\left(M_{i}(\boldsymbol{\phi}^n)\nabla\left(\mu_{i}^{n+1}+p^{n+1}\right)\right)=\phi_{i}^{n} \quad i=p,q \tag{3.81}$$

$$S_{sl}=-\lambda\left(\rho_{0,sl}^{-1}\mu_{sl}^{n+1}+(\rho_{0,sl}^{-1}-\rho_{0,sv}^{-1})p^{n+1}\right) \tag{3.82}$$

$$\mu_i^{n+1}+\epsilon_i^2\Delta\phi_i^{n+1}+\epsilon_{sv}^2\Delta\left(\sum_{j\neq sv}\phi_j^{n+1}\right)=\frac{\partial f_h(\boldsymbol{\phi}^n)}{\partial\phi_i} \tag{3.83}$$

$$\sum_{i\neq sv}\nabla\cdot\left(M_i(\boldsymbol{\phi}^n)\nabla\mu_i^{n+1}\right)+\sum_{i}\nabla\cdot\left(M_i(\boldsymbol{\phi}^n)\nabla p^{n+1}\right)+\left(\rho_{0,sv}^{-1}-\rho_{0,sl}^{-1}\right)S_{sl}^{n+1}=0. \tag{3.84}$$

We discretize in space via the second order central difference scheme. Let $u_i(j,k)$ be a generic grid function at node j,k, with i an index that will later indicate the component of the mixture. We define

$$M_i(j+\frac{1}{2},k)=\frac{1}{2}\left(M_i(j,k)+M_i(j+1,k)\right) \tag{3.85}$$

with similar definitions for $M_i(j-\frac{1}{2},k), M_i(j,k+\frac{1}{2}), M_i(j,k-\frac{1}{2})$, and we define

$$\begin{aligned}(\nabla_h \cdot M_i \nabla_h u_i)(j,k) &= \frac{1}{h^2}\left(M_i(j+\frac{1}{2},k)u_i(j+1,k) + M_i(j-\frac{1}{2},k)u_i(j-1,k)\right) \\ &+ \frac{1}{h^2}\left(M_i(j,k+\frac{1}{2})u_i(j,k+1) + M_i(j,k-\frac{1}{2})u_i(j,k-1)\right) \\ &- \frac{1}{h^2}\left(\left((M_i(j+\frac{1}{2},k) + M_i(j-\frac{1}{2},k) + M_i(j,k+\frac{1}{2}) + M_i(j,k-\frac{1}{2})\right)u_i(j,k)\right),\end{aligned} \tag{3.86}$$

the standard second order finite difference approximation. By introducing this discretized operator into the time discretized system we obtain a fully discretized system which results in the large, sparse linear system

$$\phi_{sl} - s\nabla_h \cdot (M_{sl}\nabla_h(\mu_{sl}+p)) - s\rho_{0,sl}^{-1}S_{sl} = F_{\phi_{sl}} \tag{3.87}$$

$$\phi_i - s\nabla_h \cdot (M_i\nabla_h(\mu_i+p)) = F_{\phi_i} \quad i = p,q \tag{3.88}$$

$$S_{sl} = -\lambda\left(\rho_{0,sl}^{-1}\mu_{sl} + (\rho_{0,sl}^{-1} - \rho_{0,sv}^{-1})p\right) \tag{3.89}$$

$$\mu_i + \epsilon_i^2\Delta_h\phi_i + \epsilon_{sv}^2\Delta_h\left(\sum_{j\neq sv}\phi_j\right) = F_{\mu_i} \tag{3.90}$$

$$\sum_{i\neq sv}\nabla_h\cdot(M_i\nabla_h\mu_i) + \sum_i \nabla_h\cdot(M_i\nabla_h p) + \left(\rho_{0,sv}^{-1} - \rho_{0,sl}^{-1}\right)S_{sl} = 0. \tag{3.91}$$

where the superscript $n+1$ indicating the time step has been suppressed. Note that the $M_i, F_{\phi_i}, F_{\mu_i}$ depend on the previous data ϕ_i^n, so in this linear system the mobilities M_i and forcing terms F_i are spatially dependent but do not depend on the current solution. We solve this system using the Full Approximation Storage (FAS) multigrid method based on the two-level algorithm [50], which is extended into an adaptive algorithm as in [54]. For the equations (3.87) - (3.91) we define the solution variables and operators compactly as

$$\mathbf{\Phi}(j,k) = (\phi_{sl}(j,k), \mu_{sl}(j,k), \phi_p(j,k), \mu_p(j,k), \phi_q(j,k), \mu_q(j,k), p(j,k)), \tag{3.92}$$

$\boldsymbol{N}$ the operator on the left hand side, $\boldsymbol{S}$ the right hand side, so that we are solving $\boldsymbol{N}(\boldsymbol{\Phi}) = \boldsymbol{S}$. We define $\boldsymbol{\Phi}_m, \boldsymbol{N}_m, \boldsymbol{S}_m$ to be the solution, operator, and right hand side for the mth level grid. The two level method is then written as

Initialize $\boldsymbol{\Phi}_m^0 = \boldsymbol{\Phi}_m^{n+1,0} \longleftarrow \boldsymbol{\Phi}_m^n$, the solved solution at the last time step;

Initialize $\boldsymbol{S}_m = \boldsymbol{S}_m^{n+1}$;

while $\|\boldsymbol{N}_m(\boldsymbol{\Phi}_m^r) - \boldsymbol{S}_m\| > tol$ **do**

$\boldsymbol{\Phi}_m^r = \text{Smooth}^\lambda(\boldsymbol{\Phi}_m^r, \boldsymbol{N}_m, \boldsymbol{S}_m)$;

$\boldsymbol{r}_m^r = \boldsymbol{S}_m - \boldsymbol{N}_m(\boldsymbol{\Phi}_m^r)$;

Restrict $\boldsymbol{r}_{m-1}^r = I_m^{m-1}\boldsymbol{r}_m^r, \boldsymbol{\Phi}_{m-1}^r = I_m^{m-1}\boldsymbol{\Phi}_m^r$;

Solve $\boldsymbol{N}_{m-1}(\boldsymbol{\Psi}_{m-1}^r) = \boldsymbol{N}_{m-1}(\boldsymbol{\Phi}_{m-1}^r) + \boldsymbol{r}_{m-1}^r$;

$\boldsymbol{e}_{m-1}^r = \boldsymbol{\Psi}_{m-1}^r - \boldsymbol{\Phi}_{m-1}^r$;

Prolongate $\boldsymbol{\Phi}_m^r = \boldsymbol{\Phi}_m^r + I_{m-1}^m \boldsymbol{e}_{m-1}^r$;

$\boldsymbol{\Phi}_m^r = \text{Smooth}^\lambda(\boldsymbol{\Phi}_m^r, \boldsymbol{N}_m, \boldsymbol{S}_m)$;

end

Algorithm 1: Two-level Algorithm

To implement the boundary conditions, we extend the grid to include one layer of ghost cells, and require that the ghost cells' values satisfy the discrete boundary conditions. So, for example, on the bottom boundary for (3.30) we solve

$$\frac{\phi_p(j,0) - \phi_p(j,1)}{h} = -\frac{\alpha_i}{\epsilon_i^2} \tag{3.93}$$

where $\phi_q(j,0)$ represents the value of ϕ_q on a ghost cell. We do remark that the boundary conditions for the pressure and chemical potentials may appear coupled in (3.79) on first glance, however, once the pressure is updated through the first equation

$$-\nabla p(\boldsymbol{x},t) \cdot \boldsymbol{n} = \beta p \tag{3.94}$$

we use this value to update the ghost cells for the rest of chemical potentials so that no linear system needs to be solved for the boundary conditions. The smoother used for the multigrid method is a Red-Black Gauss-Seidel smoother, though we present one that is more Jacobi-like, as the implementation of the Gauss-Seidel method iterating over the black and

red cells resembles the Jacobi method. Define $u_i^l(j,k)$ to be the lth Gauss-Seidel iterate. Then we apply the method to update the $l+1$ iterate as solving the system of equations

$$\begin{aligned}
&\phi_i^{l+1}(j,k) + \frac{s}{h^2}\left(M_i(j+\frac{1}{2},k) + M_i(j-\frac{1}{2},k) + M_i(j,k+\frac{1}{2}) + M_i(j,k-\frac{1}{2})\right)\mu_i^{l+1}(j,k) \\
&\quad - \frac{s}{h^2}\left(M_i(j-\frac{1}{2},k)\mu_i^l(j-1,k) + M_i(j+\frac{1}{2},k)\mu_i^l(j+1,k)\right) \\
&\quad - \frac{s}{h^2}\left(M_i(j,k-\frac{1}{2})\mu_i^l(j,k-1) + M_i(j,k+\frac{1}{2})\mu_i^l(j,k+1)\right) \\
&\quad + \frac{s}{h^2}\left(M_i(j+\frac{1}{2},k) + M_i(j-\frac{1}{2},k) + M_i(j,k+\frac{1}{2}) + M_i(j,k-\frac{1}{2})\right)p_i^{l+1}(j,k) \\
&\quad - \frac{s}{h^2}\left(M_i(j-\frac{1}{2},k)p_i^l(j-1,k) + M_i(j+\frac{1}{2},k)p_i^l(j+1,k)\right) \\
&\quad - \frac{s}{h^2}\left(M_i(j,k-\frac{1}{2})p_i^l(j,k-1) + M_i(j,k+\frac{1}{2})p_i^l(j,k+1)\right) \\
&\quad - s\rho_{0,i}^{-1}S_i^{l+1}(j,k) \\
&\quad = F_{\phi_i}
\end{aligned} \tag{3.95}$$

$$S_{sl}^{l+1}(j,k) = -\lambda\left(\rho_{0,sl}^{-1}\mu_{sl}^{l+1}(j,k) + (\rho_{0,sl}^{-1} - \rho_{0,sv}^{-1})p^{l+1}(j,k)\right) \tag{3.96}$$

$$\begin{aligned}
&\mu_i^{l+1}(j,k) - \frac{4(\epsilon_i^2+\epsilon_{sv}^2)}{h^2}\phi_i^{l+1}(j,k) \\
&\quad + \frac{(\epsilon_i^2+\epsilon_{sv}^2)}{h^2}\left(\phi_i^l(j+1,k) + \phi_i^l(j-1,k) + \phi_i^l(j,k+1) + \phi_i^l(j,k-1)\right) \\
&\quad - \sum_{\alpha\neq i,\alpha\neq sv}\frac{4\epsilon_{sv}^2}{h^2}\phi_\alpha^{l+1}(j,k) \\
&\quad + \sum_{\alpha\neq i,\alpha\neq sv}\frac{\epsilon_{sv}^2}{h^2}\left(\phi_\alpha^l(j+1,k) + \phi_\alpha^l(j-1,k) + \phi_\alpha^l(j,k+1) + \phi_\alpha^l(j,k-1)\right) \\
&\quad = F_{\mu_i}
\end{aligned} \tag{3.97}$$

$$
\begin{aligned}
&\frac{1}{h^2}\left(M_p(j+\frac{1}{2},k)+M_p(j-\frac{1}{2},k)+M_p(j,k+\frac{1}{2})+M_p(j,k-\frac{1}{2})\right)p^{l+1}(j,k)\\
&-\frac{1}{h^2}\left(M_p(j+\frac{1}{2},k)p^l(j+1,k)+M_p(j,k+\frac{1}{2})p^l(j,k+1)\right)\\
&-\frac{1}{h^2}\left(M_p(j-\frac{1}{2},k)p^l(j-1,k)+M_xp(j,k-\frac{1}{2})p^l(j,k-1)\right)\\
&+\sum_{\alpha\neq sv}\left(\frac{1}{h^2}\left(M_\alpha(j+\frac{1}{2},k)+M_\alpha(j-\frac{1}{2},k)+M_\alpha(j,k+\frac{1}{2})+M_\alpha(j,k-\frac{1}{2})\right)\mu_\alpha^{l+1}(j,k)\right.\\
&-\frac{1}{h^2}\left(M_\alpha(j+\frac{1}{2},k)\mu_\alpha^l(j,k)+M_\alpha(j,k+\frac{1}{2})\mu_\alpha^l(j,k+1)\right)\\
&\left.-\frac{1}{h^2}\left(M_\alpha(j-\frac{1}{2},k)\mu_\alpha^l(j-1,k)+M_\alpha(j,k-\frac{1}{2})\mu_\alpha^l(j,k-1)\right)\right)\\
&+(-\rho_{0,sl}^{-1}+\rho_{0,sv}^{-1})S_i^{l+1}(j,k)=0.\quad(\text{here } M_p=\sum_k M_i).
\end{aligned}
\tag{3.98}
$$

For this system, at every grid point we must solve the system of equations of the form

$$
\begin{bmatrix}
a_{11} & a_{12} & 0 & 0 & 0 & 0 & a_{17}\\
a_{21} & a_{22} & a_{23} & 0 & a_{25} & 0 & 0\\
0 & 0 & a_{33} & a_{34} & 0 & 0 & a_{37}\\
a_{41} & 0 & a_{43} & a_{44} & a_{45} & 0 & 0\\
0 & 0 & 0 & 0 & a_{55} & a_{56} & a_{57}\\
a_{61} & 0 & a_{63} & 0 & a_{65} & a_{66} & 0\\
0 & a_{72} & 0 & a_{74} & 0 & a_{76} & a_{77}
\end{bmatrix}
\begin{bmatrix}
\phi_{sl}^{l+1}(j,k)\\
\mu_{sl}^{l+1}(j,k)\\
\phi_p^{l+1}(j,k)\\
\mu_p^{l+1}(j,k)\\
\phi_q^{l+1}(j,k)\\
\mu_q^{l+1}(j,k)\\
p^{l+1}(j,k)
\end{bmatrix}
= RHS.
\tag{3.99}
$$

Typically some decoupling strategy takes place in the smoother so as to reduce computation time, since solving this 7x7 system of equations at every grid point for this fully coupled system can be computationally expensive. There is some practical trade-off here in the sense that the more you decouple, the easier the system can be solved, but the smoother (and thus the multigrid solver) may perform more poorly, increasing the number of multigrid iterations required to solve one time step. One effective strategy to decouple the system is to move the pressure coupling terms a_{17}, a_{37},and a_{67} in the ϕ_i equations and the all of the coupling

terms in the μ_i equations, except the corresponding ϕ_i term, to the right hand side to get the system

$$\begin{bmatrix} a_{11} & a_{12} & 0 & 0 & 0 & 0 & 0 \\ a_{21} & a_{22} & 0 & 0 & 0 & 0 & 0 \\ 0 & 0 & a_{33} & a_{34} & 0 & 0 & 0 \\ 0 & 0 & a_{43} & a_{44} & 0 & 0 & 0 \\ 0 & 0 & 0 & 0 & a_{55} & a_{56} & 0 \\ 0 & 0 & 0 & 0 & a_{65} & a_{66} & 0 \\ 0 & a_{72} & 0 & a_{74} & 0 & a_{76} & a_{77} \end{bmatrix} \begin{bmatrix} \phi_{sl}^{l+1}(j,k) \\ \mu_{sl}^{l+1}(j,k) \\ \phi_{p}^{l+1}(j,k) \\ \mu_{p}^{l+1}(j,k) \\ \phi_{q}^{l+1}(j,k) \\ \mu_{q}^{l+1}(j,k) \\ p^{l+1}(j,k) \end{bmatrix} = RHS - \begin{bmatrix} a_{17}p^l(j,k) \\ a_{23}\phi_p^l(j,k) + a_{25}\phi_q^l(j,k) \\ a_{37}p^l(j,k) \\ a_{41}\phi_{sl}^l(j,k) + a_{45}\phi_q^l(j,k) \\ a_{57}p^l(j,k) \\ a_{61}\phi_{sl}^l(j,k) + a_{63}\phi_p^l(j,k) \\ 0 \end{bmatrix}. \tag{3.100}$$

This results in 3 block 2 by 2 matrix equations which are trivial to invert. Then, once those chemical potentials have been updated, the pressure Poisson equation can be solved. Another possible smoother can be derived my moving *all* ϕ_i variables in the chemical potential equations to the right hand side and keep the pressure terms implicit in the smoother,

which leads to the linear system

$$\begin{bmatrix} a_{11} & a_{12} & 0 & 0 & 0 & 0 & a_{17} \\ 0 & a_{22} & 0 & 0 & 0 & 0 & 0 \\ 0 & 0 & a_{33} & a_{34} & 0 & 0 & a_{37} \\ 0 & 0 & 0 & a_{44} & 0 & 0 & 0 \\ 0 & 0 & 0 & 0 & a_{55} & a_{56} & a_{57} \\ 0 & 0 & 0 & 0 & 0 & a_{66} & 0 \\ 0 & a_{72} & 0 & a_{74} & 0 & a_{76} & a_{77} \end{bmatrix} \begin{bmatrix} \phi_{sl}^{l+1}(j,k) \\ \mu_{sl}^{l+1}(j,k) \\ \phi_{p}^{l+1}(j,k) \\ \mu_{p}^{l+1}(j,k) \\ \phi_{q}^{l+1}(j,k) \\ \mu_{q}^{l+1}(j,k) \\ p^{l+1}(j,k) \end{bmatrix} = RHS$$
$$- \begin{bmatrix} 0 \\ a_{21}\phi_{sl}^{l}(j,k) + a_{23}\phi_{p}^{l}(j,k) + a_{25}\phi_{q}^{l}(j,k) \\ 0 \\ a_{41}\phi_{sl}^{l}(j,k) + a_{43}\phi_{p}^{l}(j,k) + a_{45}\phi_{q}^{l}(j,k) \\ 0 \\ a_{61}\phi_{sl}^{l}(j,k) + a_{63}\phi_{p}^{l}(j,k) + a_{65}\phi_{q}^{l}(j,k) \\ 0 \end{bmatrix} \tag{3.101}$$

which is attractive as this is an upper triangular upon rearrangement of the variables, and as such can be solved through back substitution by first solving for the μ_i components, then the pressure, then the ϕ_i components

3.3.3 A Numerical Experiment on Smoothers

We consider here a numerical experiment to demonstrate the effectiveness of possible smoothers. We consider the problem posed on a computational domain $[0, 100]$x$[0, 100]$ with seven levels of refinement, so that the finest level has 128 grid points in each direction. The solution is initially set so that $\phi_{sl}(x, y) = \phi_p(x, y) = \phi_q(x, y) = 10^{-8}$, so that $\phi_{sv} \approx 1$ in this region. For $y < 75$ we set $\phi_{sv} = 10^{-8}$ and $\phi_p = 0.1 + \text{rand}(x, y)$ where $\text{rand}(x, y)$ is a random number strictly between -0.1 and 0.1, $\phi_q = 0.15$ and ϕ_{sl} to satisfy the no voids constraint

$$\sum_{i \in I} \phi_i = 1. \tag{3.102}$$

Table 3.1: Parameters for Numerical Experiment on Smoothers for Multigrid

Gradient Energy Coefficients		Mobilities		Densities	
ϵ_{sv}^2	0.7	γ_{sv}	5.0	$\rho_{0,sv}$	0.010
ϵ_{sl}^2	0.7	γ_{sl}	5.0	$\rho_{0,sl}$	1.0
ϵ_{p}^2	0.7	γ_{p}	1.0	$\rho_{0,p}$	1.0
ϵ_{q}^2	0.7	γ_{q}	1.0	$\rho_{0,q}$	1.0

Interaction Parameters	
$\chi_{sv,sl}$	1.7
$\chi_{sv,p}$	1.7
$\chi_{sv,q}$	1.7
$\chi_{sl,p}$	.40
$\chi_{sl,q}$	.90
$\chi_{p,q}$	1.0

Miscellaneous Parameters	
β	1.000
λ	.001
δ	.001
c	5.0
N_2	89.0
N_3	7.0

We run a solver with smoother based on (3.101) with time step $s = 10^{-4}$ until $t = 100$. Then, using the solved solution at $t = 100$ as initial data, we run the solver with different smoothers, using 1 presmooth and 1 postsmooth in the multigrid iteration. For the smoother based on (3.99), after allowing the solver to run until $t \approx 100.5$, 4 to 6 multigrid iterations are required for convergence. In using the decoupled smoother (3.101), at $t \approx 100.5$ we require between 8 and 11 iterations for convergence. For smoother (3.100) at $t \approx 100.5$, again between 4 and 6 iterations are required, demonstrating that the decoupling (3.100) is practically as efficient as (3.99), though computationally much faster due to its block decoupled structure.

3.4 Simulations of Polymer Mixtures with an Evaporating Solvent

We now present simulations that demonstrate the model's effectiveness by varying parameters and presenting the time-evolution of the numerical solution. For clarity, we write the implemented (nondimensional) equations

$$\frac{\partial \phi_{sl}}{\partial t} - \nabla \cdot \left(M_{sl}(\boldsymbol{\phi}) \nabla \left(\mu_{sl} + p \right) \right) = \rho_{0,sl}^{-1} S_{sl} \tag{3.103}$$

$$\frac{\partial \phi_i}{\partial t} - \nabla \cdot \left(M_i(\boldsymbol{\phi}) \nabla \left(\mu_i + p \right) \right) = 0 \tag{3.104}$$

$$S_{sl} = -\lambda \left(\rho_{0,sl}^{-1} \mu_{sl} + \rho_{0,sl}^{-1} p - \rho_{0,sv}^{-1} p \right) \tag{3.105}$$

where the mobilities $M_i(\boldsymbol{\phi}) = \gamma_i \phi_i^2$ unless otherwise noted. Notice here that previously in the model derivation γ_i could indicate some function of the concentrations. In this section, it is some (constant) parameter. The chemical potential equations are

$$\mu_i = \frac{\partial f_h}{\partial \phi_i} - \epsilon_i^2 \Delta \phi_i - \epsilon_{sv}^2 \sum_{\substack{j \neq i \\ j \neq sv}} \Delta \phi_j. \tag{3.106}$$

with the Flory-Huggins free energy

$$f_h(\boldsymbol{\phi}) = \sum_{i \in I} \left(\rho_{0,i} \phi_i \ln_\delta(\phi_i) \right) + \sum_{i \neq j} \chi_{ij} \phi_i \phi_j \quad \text{with } \phi_{sv} = 1 - \sum_{i \neq sv} \phi_i \tag{3.107}$$

and the pressure Poisson equation is

$$-\sum_{i \in I} \nabla \cdot \left(M_i(\boldsymbol{\phi}) \nabla p \right) - \sum_{\substack{i \in I \\ i \neq sv}} \nabla \cdot \left(M_i(\boldsymbol{\phi}) \nabla \mu_i \right) = \left(\rho_{0,sl}^{-1} - \rho_{0,sv}^{-1} \right) S_{sl}. \tag{3.108}$$

3.4.1 Simulations in One Space Dimension

Presented in this section are simulations analyzing the dependence of the model on the parameters β and λ. Plots of the vapor phase volume fraction (ϕ_{sv}) are presented. Each simulation is run on a computational domain of $[0, 100]$. For $x < 75$ all simulations are initialized with $\phi_p = 0.1 + \text{rand}(x)$ where rand(x) is a random number between -0.1 and 0.1, so that ϕ_p is some number chosen randomly between 0.0 and 0.2. The other variables are initilized as $\phi_q = 0.15$ and $\phi_{sv} = 10^{-8}$, with ϕ_{sl} initialized to satisfy the no voids constraint

$$\sum_{i \in I} \phi_i = 1. \tag{3.109}$$

This region is to model the polymer mixture, with the solvent in the vapor phase above it. Thus for $x > 75$ we will initialize all the volume fractions except that of the solvent

in the vapor phase to be approximately zero. We choose to set $\phi_{sl} = \phi_p = \phi_q = 10^{-8}$, with $\phi_{sv} = 1.0 - 3 \times 10^{-8}$ in this region satisfying the no voids condition. The first two simulations comprise of two simulations for each set of parameters given, one with the Robin-type boundary conditions for $\boldsymbol{u}_{sv}$ *and* $\boldsymbol{u}_{sl}$ so that on $\partial\Omega_{\text{top}}$

$$\begin{aligned} -\nabla\mu_{sv}(\boldsymbol{x},t)\cdot\boldsymbol{n} &= \beta\mu_{sv}(\boldsymbol{x},t) \quad -\nabla\mu_{sl}(\boldsymbol{x},t)\cdot\boldsymbol{n} = \beta\mu_{sl}(\boldsymbol{x},t) \\ -\nabla p(\boldsymbol{x},t)\cdot\boldsymbol{n} &= \beta p(\boldsymbol{x},t) \end{aligned} \tag{3.110}$$

and another with the no flow boundary conditions for $\boldsymbol{u}_{sl}$. The nonzero Robin-type boundary conditions for $\boldsymbol{u}_{sl}$ allow for $\boldsymbol{u}_{sl}\cdot\boldsymbol{n}$ to be nonzero on the boundary, and thus allows for solvent in the liquid phase to flux across the boundary at $x = 100$. The first two simulations show that this effect dominates the effect of the other parameters on the speed of the interface between the solvent in the vapor phase and the polymer mixture. All simulations were done on a grid with 128 spatial grid points and time step $s = .001$, and the surface energy term $f_s(\boldsymbol{\phi})$ is set to zero for the entire set of one-dimensional simulations, which leads to the homogeneous Neumann boundary conditions for the volume fractions $\nabla\phi_i\cdot\boldsymbol{n} = 0$ via (3.30).

One Dimensional Simulation 1

The set of parameters for this simulation are given in Table 3.2. The general qualitative behavior observed is what one might expect in a mixture with an evaporating solvent. There initially is a small vapor phase indicated by $\phi_{sv} \approx 1$ on top of the polymer mixture where $\phi_{sv} \approx 0$. As can be seen in the Figures 3.1 and 3.2, the solvent in the liquid phase evaporates and the vapor phase grows until the solvent in the liquid phase has completely left the system, after which the vapor phase cannot grow anymore since the governing equations do not permit a change in mass of the polymers p or q. In Figure 3.1 we have a simulation with the flow boundary conditions for $\boldsymbol{u}_{sl}$, specifically $\beta_{sl} = \beta = \beta_{sv}$, as given in Table 3.2. Comparing the simulations in Figures 3.1 and 3.2, we see that this boundary condition has a drastic effect on the time scale of evaporation. Additionally included is a plot of the polymer p volume fraction ϕ_p in Figure 3.3, which shows 1 dimensional "layers" of pure polymer phase forming as the solvent is removed from the system.

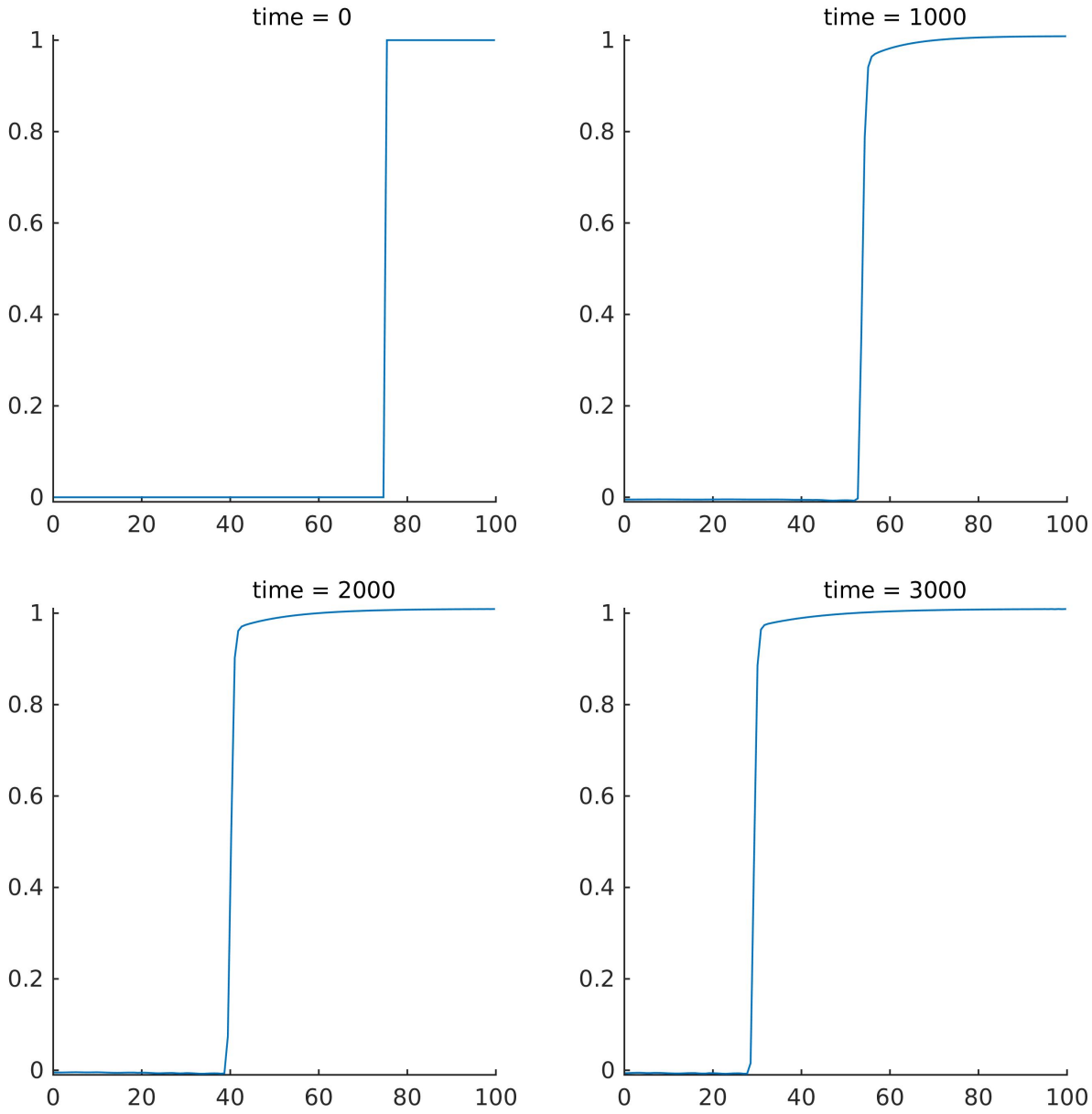

Figure 3.1: In this simulation we plot ϕ_{sv} at multiple times, and we use parameters from Table 3.2 with the flow boundary conditions on $\boldsymbol{u}_{sl}$. The important qualitative behavior that is observed in this simulation is that there is a pronounced interface between the vapor phase ($\phi_{sv} \approx 1$) and the polymer mixture ($\phi_{sv} \approx 0$), and that the polymer mixture shrinks in height until the solvent in the liquid phase has fully evaporated.

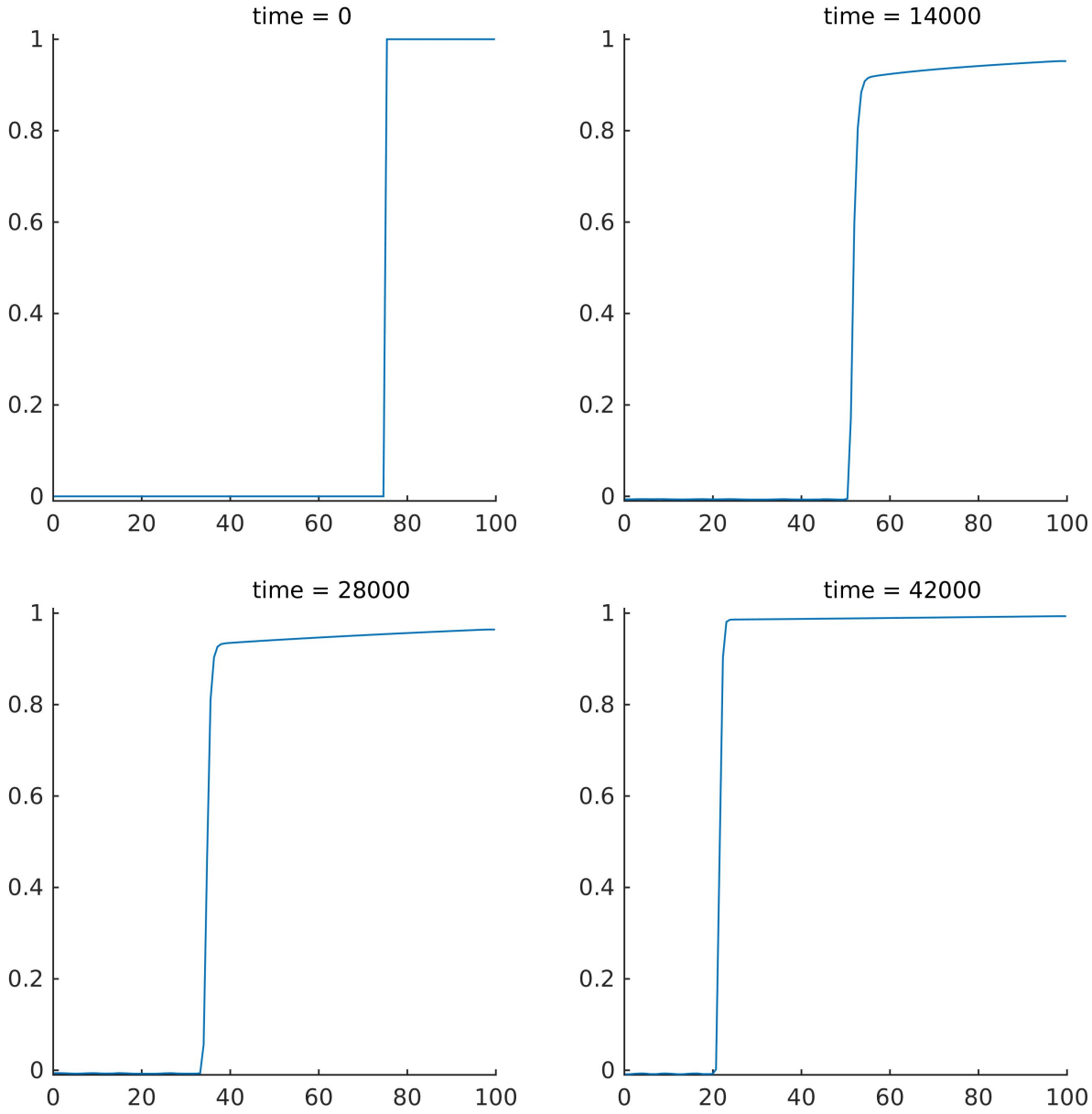

Figure 3.2: In this simulation we plot ϕ_{sv} at multiple times, and we use parameters from Table 3.2 with the no-flow boundary conditions on $\boldsymbol{u}_{sl}$. Similar to the simulation in Figure 3.1, the qualitative behavior that is observed in this simulation is that there is a pronounced interface between the vapor phase ($\phi_{sv} \approx 1$) and the polymer mixture ($\phi_{sv} \approx 0$), and that the polymer mixture shrinks in height until the solvent in the liquid phase has fully evaporated. Note there is a significant time scale difference between this simulation and the simulation in Figure 3.1 due to the no-flow boundary conditions applied to $\boldsymbol{u}_{sl}$ here.

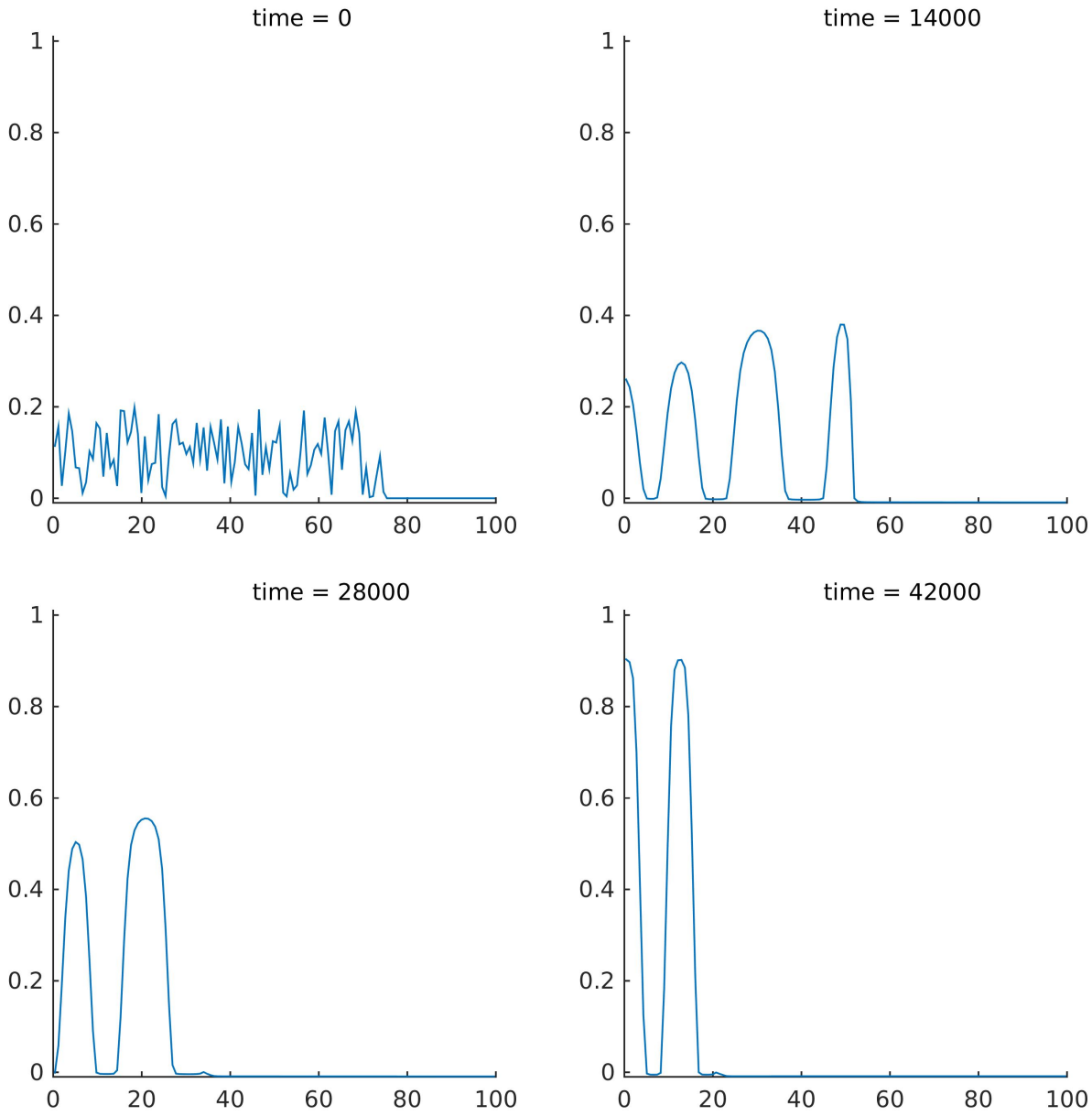

Figure 3.3: In this simulation we plot ϕ_p at multiple times, and we use parameters from Table 3.2 with the no-flow boundary conditions on $\boldsymbol{u}_{sl}$. This plot of the polymer p volume fraction is from the same simulation from that of Figure 3.2. We observe that as the solvent in the liquid phase is exiting the polymer mixture, the volume fraction of the polymer is increasing while the total size of the polymer mixture is decreasing. Shortly after the last plot shown at nondimensional time t = 42000, the solvent in the liquid phase has fully evaporated from the system ($\phi_{sl} \approx 0$), and all that is left are the two polymers.

Table 3.2: Parameters for One Dimensional Simulation 1 with Solvent Evaporation

Gradient Energy Coefficients		Mobilities		Densities	
ϵ_{sv}^2	1.00	γ_{sv}	5.0	$\rho_{0,sv}$	0.010
ϵ_{sl}^2	1.00	γ_{sl}	5.0	$\rho_{0,sl}$	1.0
ϵ_{p}^2	1.00	γ_{p}	1.0	$\rho_{0,p}$	1.0
ϵ_{q}^2	1.00	γ_{q}	1.0	$\rho_{0,q}$	1.0

Interaction Parameters	
$\chi_{sv,sl}$	1.7
$\chi_{sv,p}$	1.7
$\chi_{sv,q}$	1.7
$\chi_{sl,p}$	.40
$\chi_{sl,q}$	.90
$\chi_{p,q}$	1.0

Miscellaneous Parameters	
β	1.000
λ	.001
δ	.001
c	5.0
N_2	89.0
N_3	7.0

One Dimensional Simulation 2

Relative to simulation 1, this simulation increases β by a factor of 10 from $\beta = 1.0$ in simulation 1 (see table 3.2) to $\beta = 10.0$. The other parameters used in this simulation are listed in Table 3.3 and are identical to those in simulation 1. The effect of increasing this parameter on the mathematical model is made transparent when recalling the relationship of β_i to ω_i in 2.32 as $\beta_i = \frac{\omega_i}{\gamma_i}$. Increasing β_i increases ω_i, which increases the effect $r_i(\boldsymbol{x}, t)$ has on $\boldsymbol{u}_i \cdot \boldsymbol{n}$, defined in 2.29. In comparing Figures 3.1 and 3.4 we see that this increase in β has little effect on rate at which the interface moves when the flow boundary conditions are specified for $\boldsymbol{u}_{sl}$. However, when we set the no-flow boundary conditions for $\boldsymbol{u}_{sl}$, we see in comparing Figures 3.2 with 3.5 the interface speed is much faster than the previous simulation.

One Dimensional Simulation 3

For this simulation all parameters the same as simulation 1, with the exception of λ, the parameter which describes the rate at which solvent in the liquid phase becomes solvent in the vapor phase through the mechanism of the source term $S_{sl}(\boldsymbol{x}, t)$. This parameter has been decreased by a factor of 100 from 10^{-3} to 10^{-5}. We see that, comparing Figure 3.2 with Figure 3.6, this drastically reduces the speed of the interface. We only present a simulation

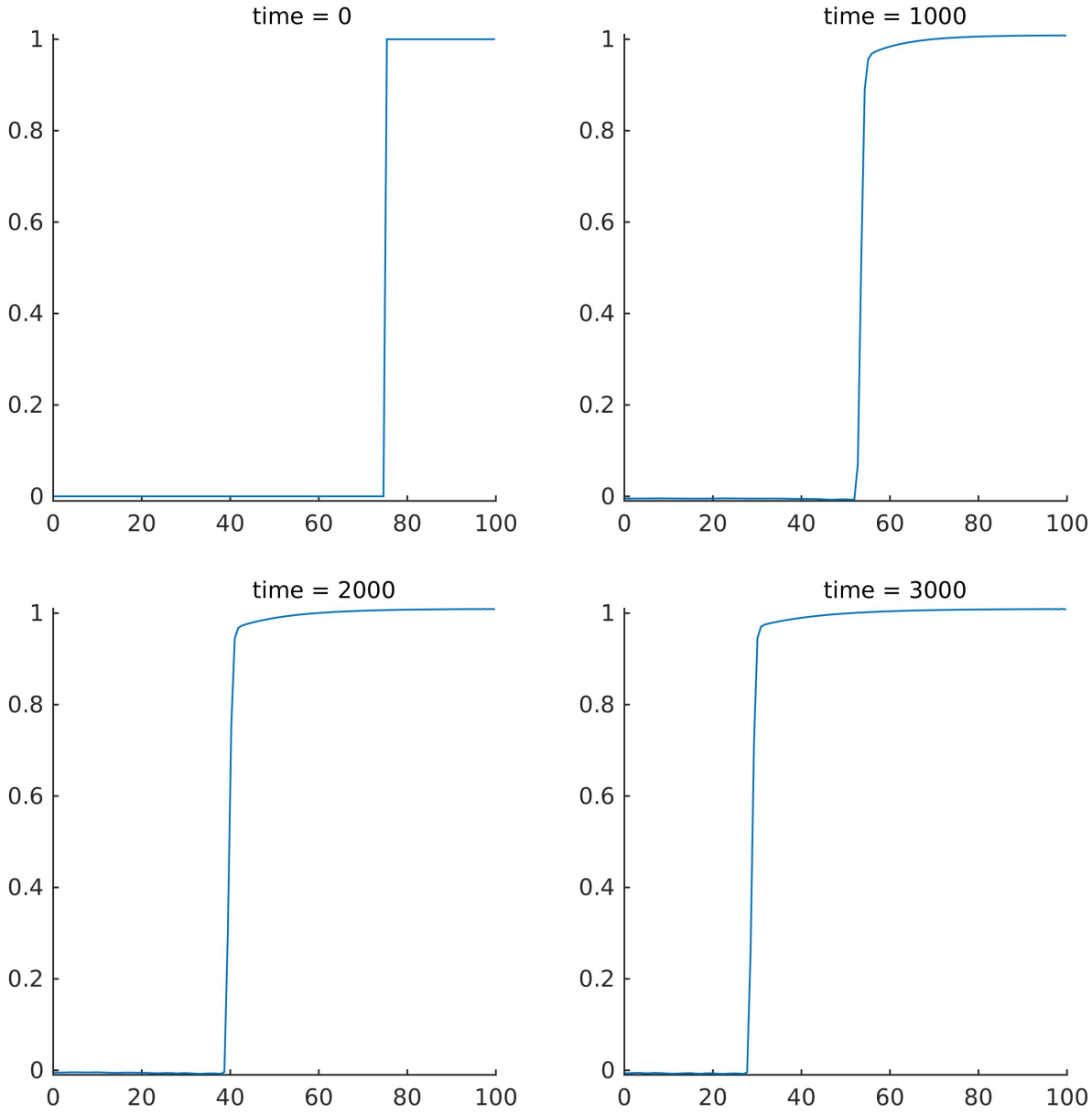

Figure 3.4: In this simulation we plot ϕ_{sv} at multiple times, and we use parameters from Table 3.3 with the flow boundary conditions on $\boldsymbol{u}_{sl}$. We see the same qualitative behavior as that of the previous simulations. Important to note in this simulation is that even though β has been increased by an order of magnitude, this has little effect as the flow boundary conditions for $\boldsymbol{u}_{sl}$ dominate the speed of the interface, in contrast to the relationship between the simulation presented in Figures 3.5 and 3.2 for which we see a large change in the time required for the solvent in the liquid phase to fully evaporate.

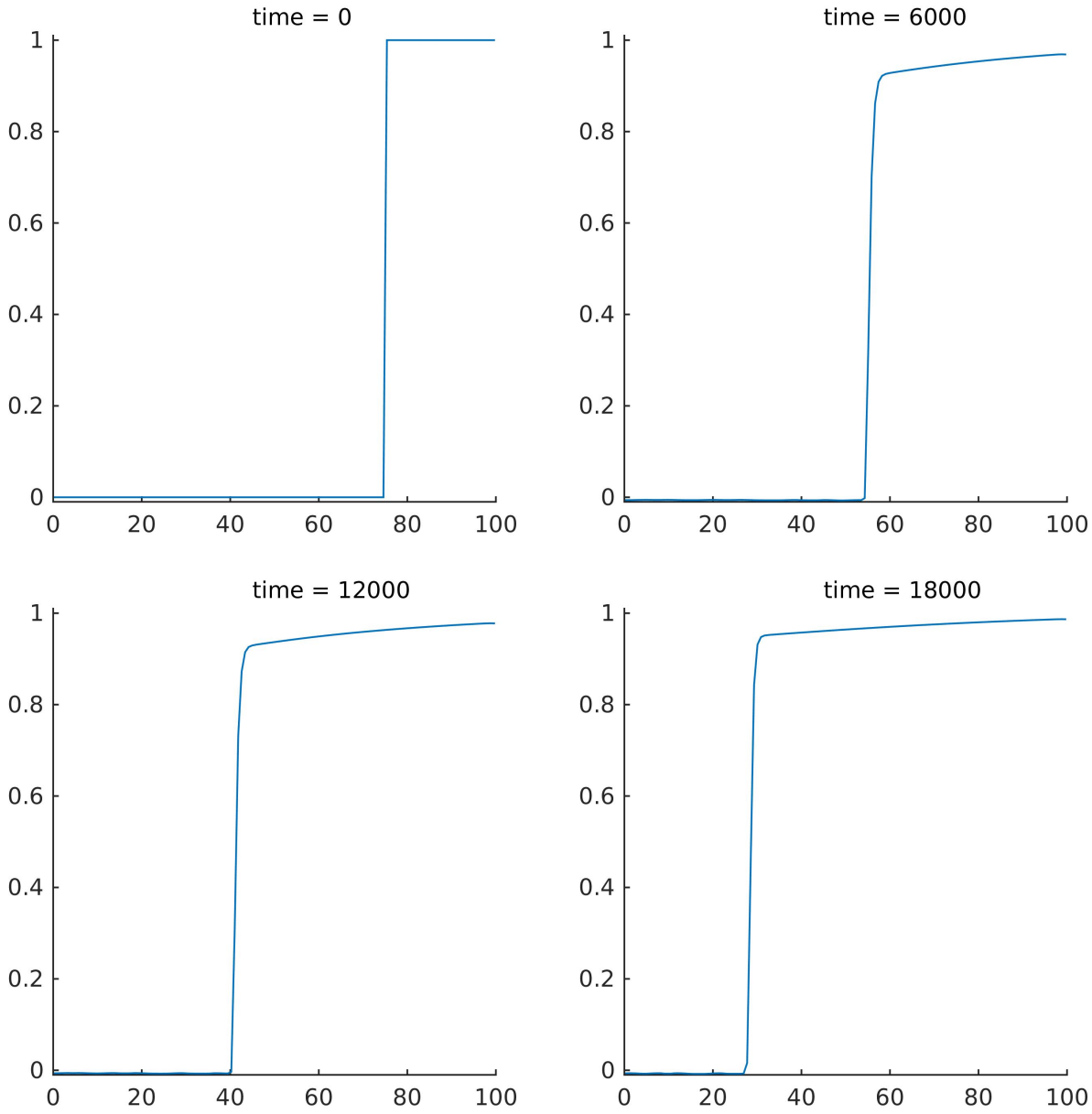

Figure 3.5: In this simulation we plot ϕ_{sv} at multiple times, and we use parameters from Table 3.3 with the no-flow boundary conditions on $\boldsymbol{u}_{sl}$. Soon after the final simulation plot is shown at t=18000 above, the solvent in the liquid phase has fully evaporated, so $\phi_{sl} \approx 0$. In comparing to the simulation shown in Figure 3.2, we observe that the time required for this to occur is much smaller due to the increase in β.

Table 3.3: Parameters for One Dimensional Simulation 2 with Solvent Evaporation

Gradient Energy Coefficients		Mobilities		Densities	
ϵ_{sv}^2	1.00	γ_{sv}	5.0	$\rho_{0,sv}$	0.010
ϵ_{sl}^2	1.00	γ_{sl}	5.0	$\rho_{0,sl}$	1.0
ϵ_{p}^2	1.00	γ_{p}	1.0	$\rho_{0,p}$	1.0
ϵ_{q}^2	1.00	γ_{q}	1.0	$\rho_{0,q}$	1.0

Interaction Parameters	
$\chi_{sv,sl}$	1.7
$\chi_{sv,p}$	1.7
$\chi_{sv,q}$	1.7
$\chi_{sl,p}$	.40
$\chi_{sl,q}$	.90
$\chi_{p,q}$	1.0

Miscellaneous Parameters	
β	10.000
λ	.001
δ	.001
c	5.0
N_2	89.0
N_3	7.0

for the no-flow boundary condition on $\boldsymbol{u}_{sl}$, but we note that similar behavior occurs to the previous two simulations when prescribing the flow boundary conditions for $\boldsymbol{u}_{sl}$. That is, changing the λ parameter does *not* have a significant effect on the speed of the vapor interface when the flow boundary conditions for $\boldsymbol{u}_{sl}$ are specified.

Dependence of Interface Velocity on the Parameters

With many plots of ϕ_{sv} already have been given, we present more compactly the dependence of the interface on the parameters. Presented below are time plots of the interface location for various β and λ parameters. The parameters in Table 3.5 remain the same for each of the simulations done.

The interface location is defined here to be the x such that $\phi_{sv}(x) = 0.5$ (which is unique for these simulations). Increasing the parameter β introduced in (3.17) corresponds to varying ω_i for fixed γ_i, which increases the flux of vapor particles across the boundary. Increasing λ increases the rate at which solvent particles in the liquid phase transition to solvent particles in the vapor phase (and possibly vice versa). All of these simulations were run with the no flow boundary conditions on $\boldsymbol{u}_{sl}$, as we have already remarked previously that the flow boundary conditions on $\boldsymbol{u}_{sl}$ dominate the effect of the other parameters. The no-flow boundary conditions for $\boldsymbol{u}_{sl}$ implies that solvent particles in the liquid form cannot

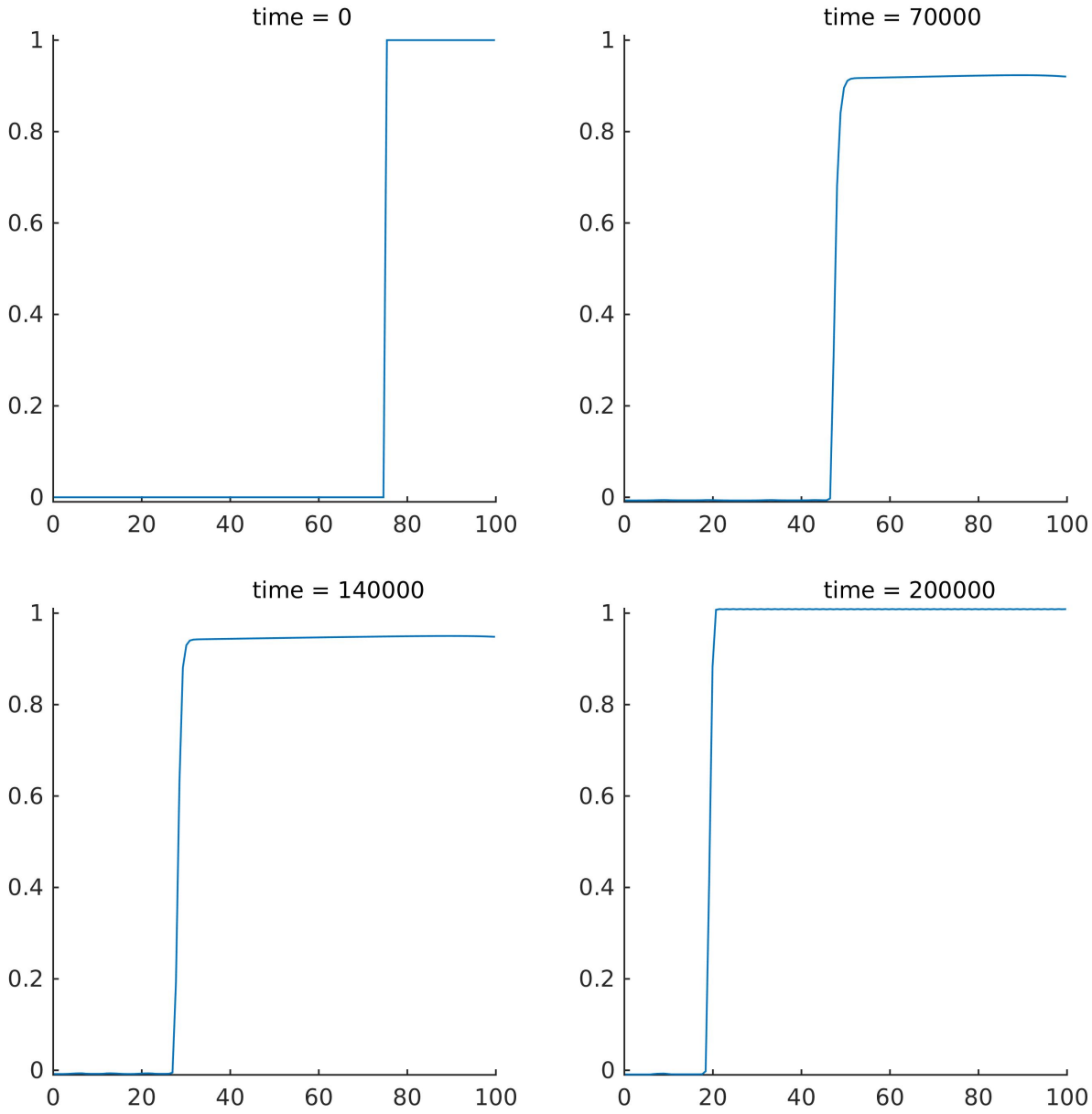

Figure 3.6: In this simulation we plot ϕ_{sv} at multiple times, and we use parameters from Table 3.4 with the no flow boundary conditions on $\boldsymbol{u}_{sl}$. In this simulation, however, we have a decreased λ, which decreases the rate at which solvent particles in the liquid phase transition into solvent particles in the vapor phase via the mechanism S_{sl}. This significantly increases the time required for all of the solvent to exit the system.

Table 3.4: Parameters for One Dimensional Simulation 3 with Solvent Evaporation

Gradient Energy Coefficients		Mobilities		Densities	
ϵ_{sv}^2	1.00	γ_{sv}	5.0	$\rho_{0,sv}$	0.010
ϵ_{sl}^2	1.00	γ_{sl}	5.0	$\rho_{0,sl}$	1.0
ϵ_{p}^2	1.00	γ_{p}	1.0	$\rho_{0,p}$	1.0
ϵ_{q}^2	1.00	γ_{q}	1.0	$\rho_{0,q}$	1.0

Interaction Parameters	
$\chi_{sv,sl}$	1.7
$\chi_{sv,p}$	1.7
$\chi_{sv,q}$	1.7
$\chi_{sl,p}$	.40
$\chi_{sl,q}$	.90
$\chi_{p,q}$	1.0

Miscellaneous Parameters	
β	1.000
λ	10^{-5}
δ	.001
c	5.0
N_2	89.0
N_3	7.0

directly flux in and out of the domain through the right side boundary, but instead must transition first into vapor phase particles through the mechanism of the source terms S_{sl}. These simulations were run with 256 spatial grid points on the domain $[0, 100]$ with a time step of $s = .001$.

In Figure 3.7, where we fix $\lambda = 10^{-4}$ and vary β, we observe increasing β increases the speed of the interface. We also observe that if $\beta = 0$, the interface does not move even though $\lambda \neq 0$. This is a consequence of a combination of 1) of the mismatch in density between the vapor and the liquid phase and 2) the mass time derivative computation (2.33). We observe in (2.33) the mass change is due to the flow boundary conditions, since the sources sum to zero (2.7). When $\beta = 0$, there are no-flow boundary conditions for *all* of the velocities, so that even though solvent in the liquid phase may transition to solvent in the vapor phase and vice versa through S_{sl}, it must do so in a mass conservative way.

In Figure 3.8, where we fix $\beta = 1.0$ and vary λ, we observe that increasing λ also increases the speed of the interface. Additionally, we observe that if $\lambda = 0$ we do not have motion of the interface, since solvent in the liquid phase cannot transition to solvent in the vapor phase in this case.

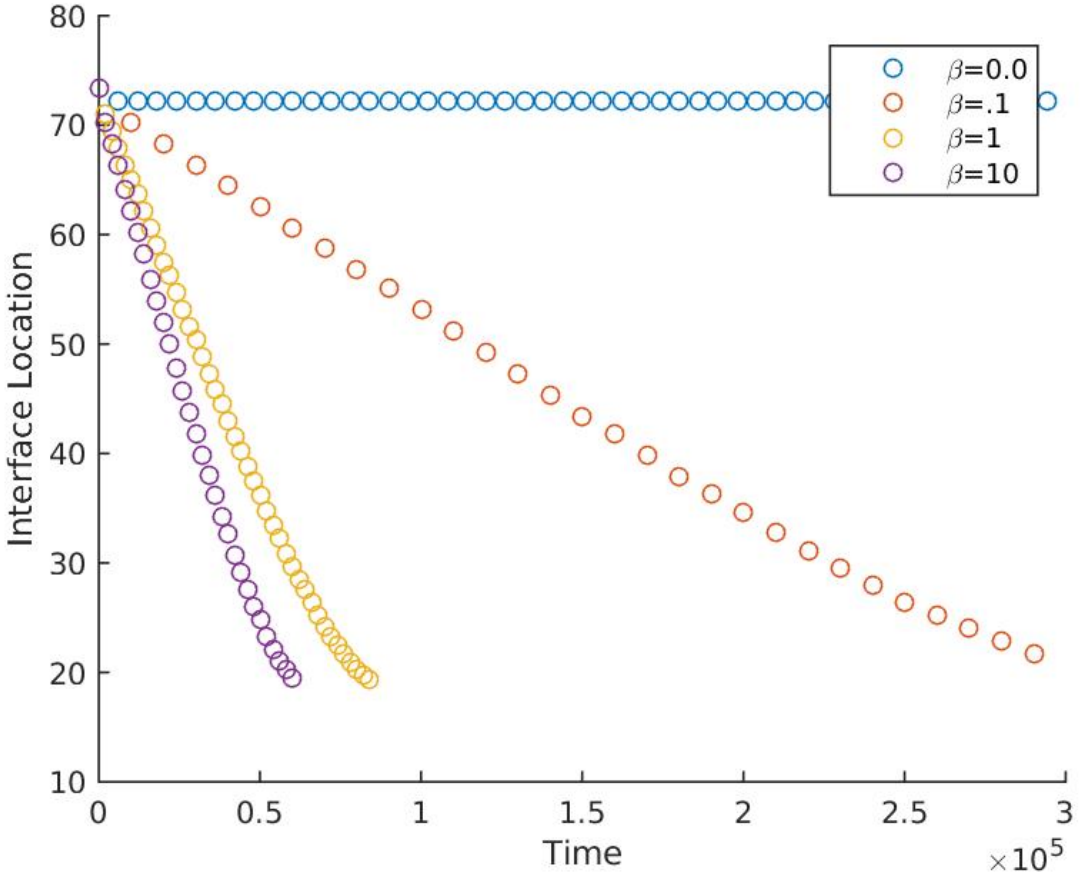

Figure 3.7: We plot the interface location of the vapor-polymer interface for several simulations against time, while only varying the β parameter with λ fixed at 10^{-4}. For $\beta = 0.0$ we see that, even though the source term is active ($\lambda > 0$), the interface does not move. This is due to the mass conservation law 2.33.

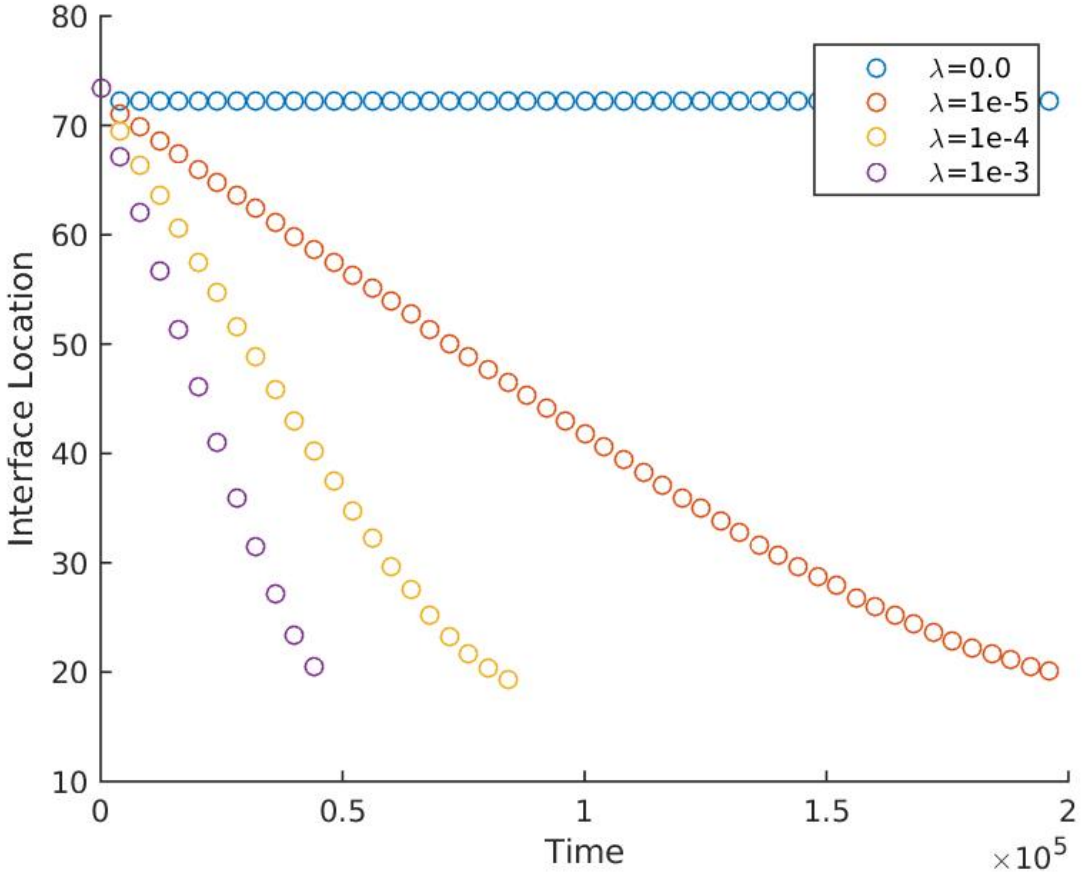

Figure 3.8: In this simulation we plot the interface location of the vapor-polymer interface for several simulation against time, while only varying λ, with β fixed at 1.0. We see that, as we increase λ, the speed of the interface increases as well, as there is more transfer of solvent in the liquid phase to solvent in the vapor phase via S_{sl}.

Table 3.5: Parameters for One Dimensional Simulations Varying λ, β with Solvent Evaporation

Gradient Energy Coefficients		Mobilities		Densities	
ϵ_{sv}^2	1.00	γ_{sv}	5.0	$\rho_{0,sv}$	0.010
ϵ_{sl}^2	1.00	γ_{sl}	5.0	$\rho_{0,sl}$	1.0
ϵ_{p}^2	1.00	γ_{p}	1.0	$\rho_{0,p}$	1.0
ϵ_{q}^2	1.00	γ_{q}	1.0	$\rho_{0,q}$	1.0

Interaction Parameters	
$\chi_{sv,sl}$	1.7
$\chi_{sv,p}$	1.7
$\chi_{sv,q}$	1.7
$\chi_{sl,p}$	.40
$\chi_{sl,q}$	.90
$\chi_{p,q}$	1.0

Miscellaneous Parameters	
δ	.001
c	5.0
N_2	89.0
N_3	7.0

3.4.2 Simulations in Two Space Dimensions

Presented in this section are simulations varying key parameters. These simulations include the boundary energy terms

$$f_s(\boldsymbol{\phi}) = \alpha_p \phi_p + \alpha_q \phi_q \tag{3.111}$$

where α_i are constants, which lead to the boundary conditions in (3.30). In each simulation we use interaction parameters $\chi_{sv,i}$ which are large enough so that solvent in the vapor phase mixing with other components is highly energetically unfavorable. The other interaction parameters are chosen so that solvent in the liquid form prefers polymer p over polymer q, and that polymer p and q are energetically unfavorable to mix. Plots of either polymer p or q are provided, along with a red line indicating the interface of the polymer mixture and the solvent in the vapor phase. This red line is the contour line $\phi_{sv} = .5$. All simulations were done on block structured adaptive mesh with the finest resolution at 128 spatial grid points in both the x and y direction along with a temporal step of $s = 10^{-4}$ using the semi-implicit described in 3.3.2. Initialization of the volume fractions were, for $y < 75$ $\phi_p = .1 + \text{rand}(x, y)$ where $\text{rand}(x, y)$ is a random number between -0.1 and 0.1, $\phi_q = .15$, $\phi_{sv} = 10^{-8}$, and ϕ_{sl} satisfying the no voids constraint. For $y > 75$ (the initial vapor phase), we have that $\phi_{sl} = \phi_q = \phi_p = 10^{-8}$ with $\phi_{sv} \approx 1$ satisfying the no voids constraint.

Table 3.6: Parameters for Two Dimensional Simulation 1 with Solvent Evaporation

Gradient Energy Coefficients		Mobilities		Densities	
ϵ^2_{sv}	1.00	γ_{sv}	1.0	$\rho_{0,sv}$	0.010
ϵ^2_{sl}	1.00	γ_{sl}	1.0	$\rho_{0,sl}$	1.0
ϵ^2_{p}	1.00	γ_{p}	1.0	$\rho_{0,p}$	1.0
ϵ^2_{q}	1.00	γ_{q}	1.0	$\rho_{0,q}$	1.0

Interaction Parameters	
$\chi_{sv,sl}$	1.7
$\chi_{sv,p}$	1.7
$\chi_{sv,q}$	1.7
$\chi_{sl,p}$	.40
$\chi_{sl,q}$	.90
$\chi_{p,q}$	1.0

Miscellaneous Parameters	
β	1.0
λ	0.001
δ	.001
c	5.0
N_2	89.0
N_3	7.0

Simulation 1

Plotted in Figure 3.9 is ϕ_p and in Figure 3.10 ϕ_{sl}. This simulation has boundary energy with $\alpha_p = -0.02$, $\alpha_q = 0.02$, and $\alpha_{sl} = \alpha_{sv} = 0$ on the bottom boundary so that the bottom boundary energetically prefers polymer p. The model removes the solvent in the liquid phase near the interface of the polymer mixture and solvent in the vapor phase, and as a result the concentration of polymers p and q increases near the location of the interface, as can be seen in 3.9 at time $t = 700$. Since χ_{pq} is large enough, it is energetically more favorable for polymers p and q to phase separate at these concentrations. As enough time passes, the solvent is completely removed f rom the system so that $\phi_{sl} \approx 0$, and the final structure that is formed are pillar-like pure phases of the two polymers.

Simulation 2

This simulation uses parameters from Table 3.7 which are similar to that of simulation 1 save that we increase the gradient energy coefficients, penalizing gradients in the solution so that fewer interfaces form. Again, polymer p is plotted in figures 3.11 through 3.13, and we see similar behavior in the time-evolution of the polymer structure with notably fewer regions of relatively pure polymer p and q. We use a boundary energy term in this case of $\alpha_p = -.04, \alpha_q = .04$.

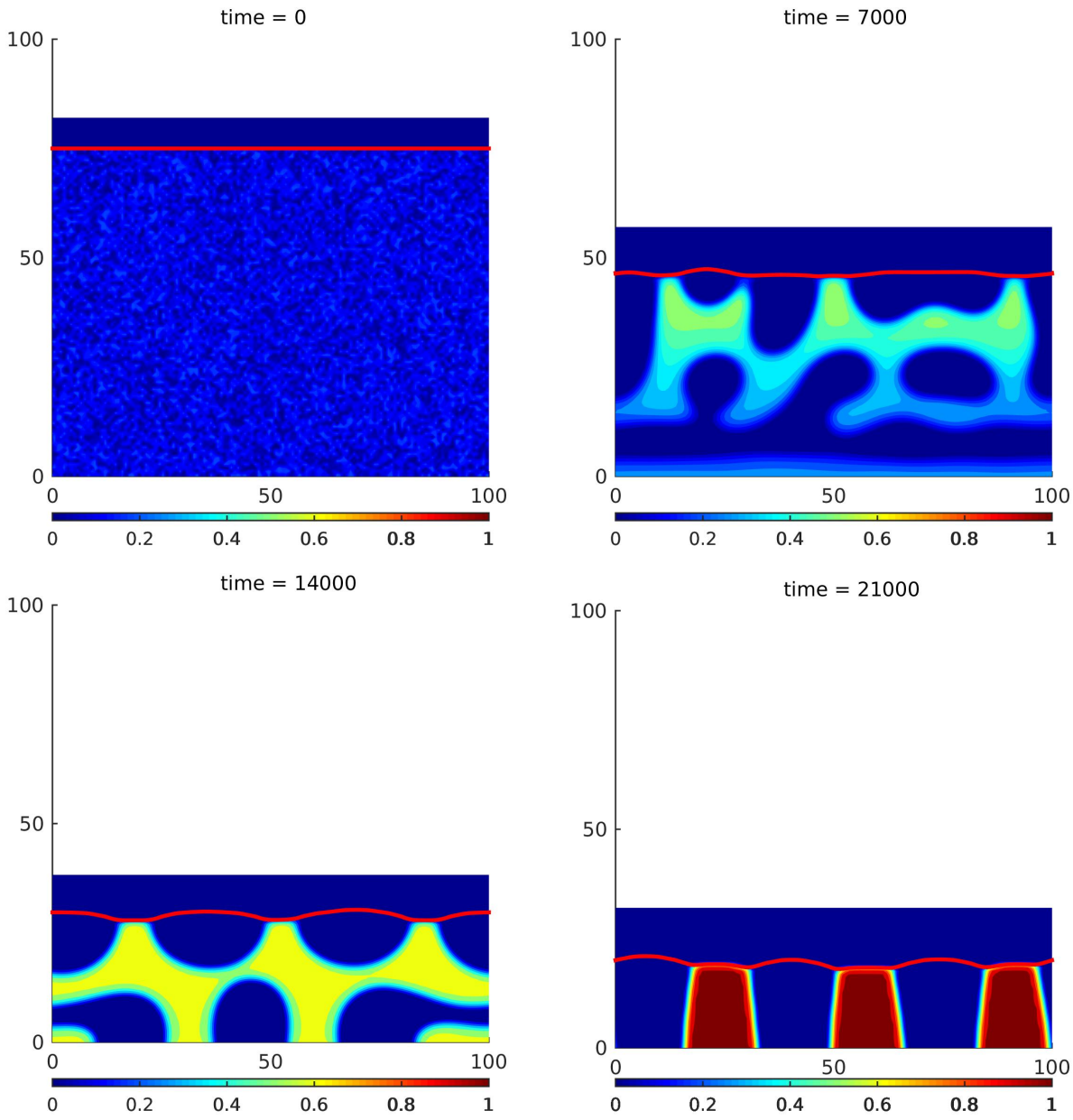

Figure 3.9: We plot the volume fraction of polymer p, ϕ_p, at multiple times with parameters from table 3.6. We see the beginnings of phase separation at time $t = 700$, more pronounced near the red line which indicates the interface between the mixture and the solvent in the vapor phase, since the solvent in the liquid phase is less concentrated here (see Figure 3.10). We also see the effect of the boundary energy term in two ways: at $t = 700$ we see the increase in the volume fraction near the bottom boundary, and the non-perpendicular contact angles at the final time $t = 21000$.

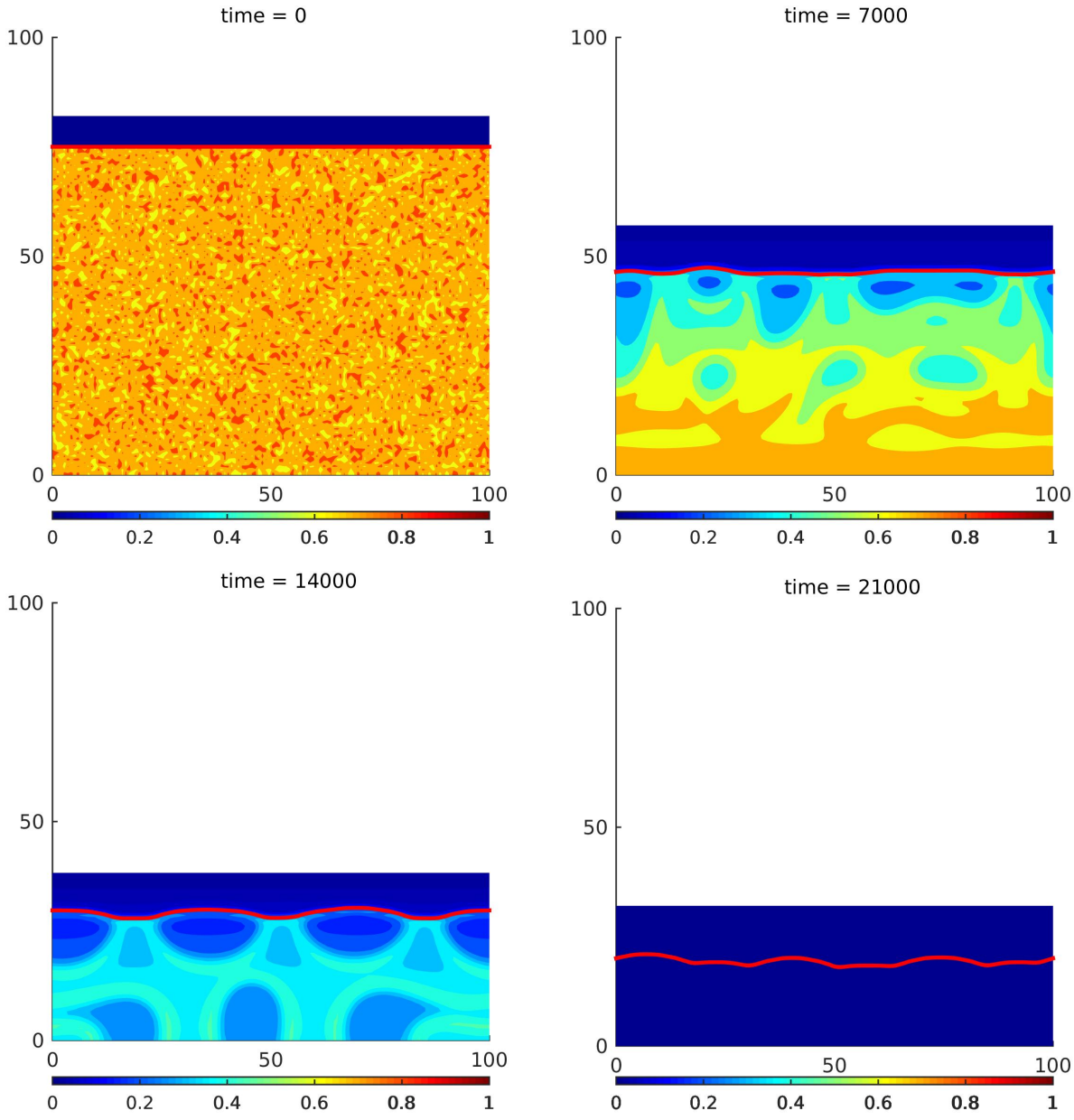

Figure 3.10: We plot the solvent volume fraction ϕ_{sl} at multiple times with parameters from table 3.6. We see the qualitative behavior that the solvent transitions into the vapor phase near the boundary, and eventually completely exits the system. Also notable is that, due to the solvents higher affinity for the polymer p due to $\chi_{sl,p} < \chi_{sl,q}$, the solvent volume fraction is larger in regions where ϕ_p is larger (compare to 3.9).

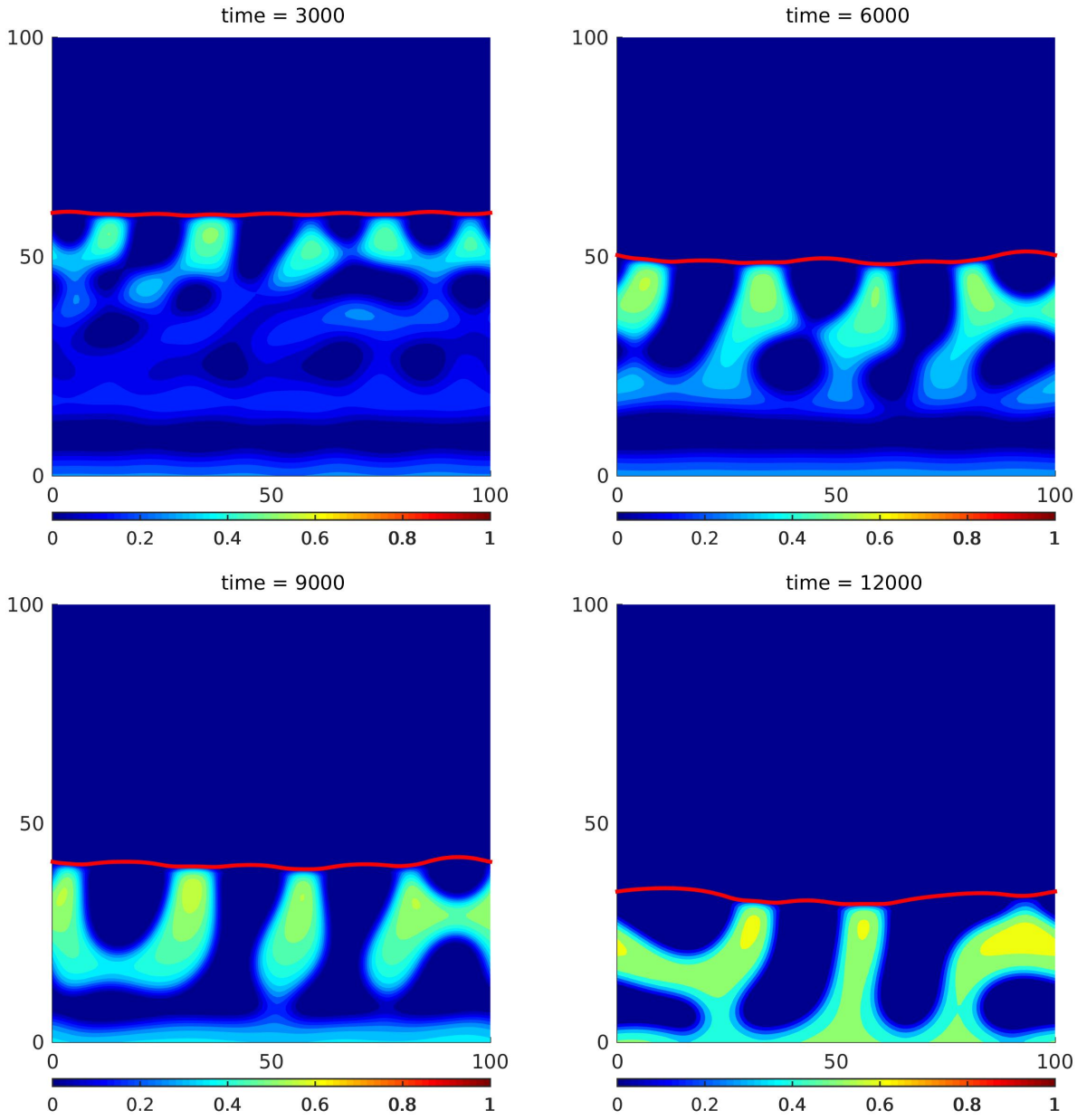

Figure 3.11: We plot the volume fraction of polymer p, ϕ_p, at multiple times with parameters from table 3.7. We see the start of the same qualitative behavior that was previously observed in Figure 3.9. However, as the simulation continues we see that fewer pillars form in the next slides (see 3.13) due to the increase in the gradient energy coefficients.

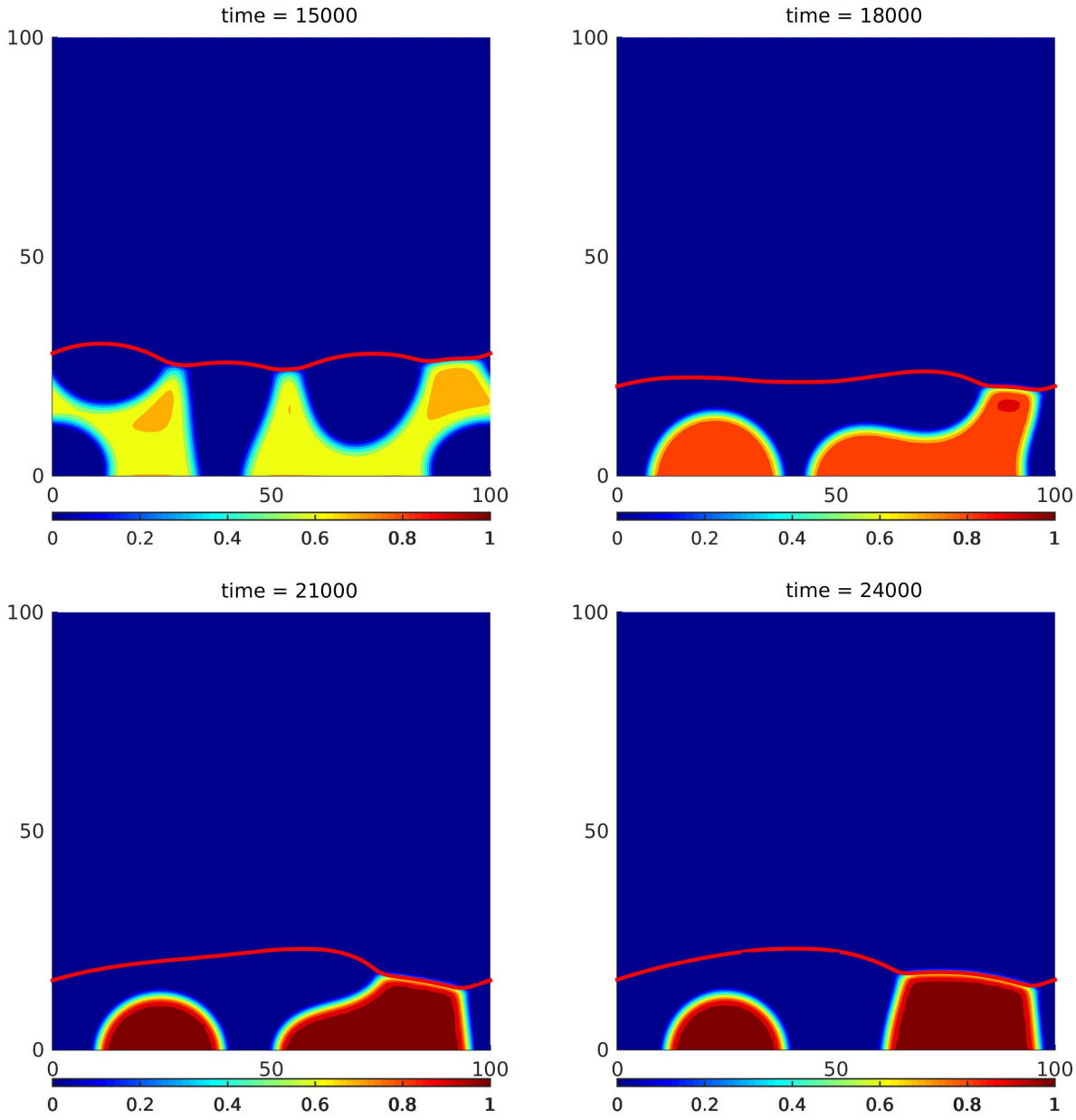

Figure 3.12: We plot the volume fraction of polymer p, ϕ_p, at multiple times with parameters from table 3.7. We see the start of the same qualitative behavior that was previously observed in Figure 3.9, save for the fewer number of regions where there is pure polymer p due to the larger gradient energy coefficients.

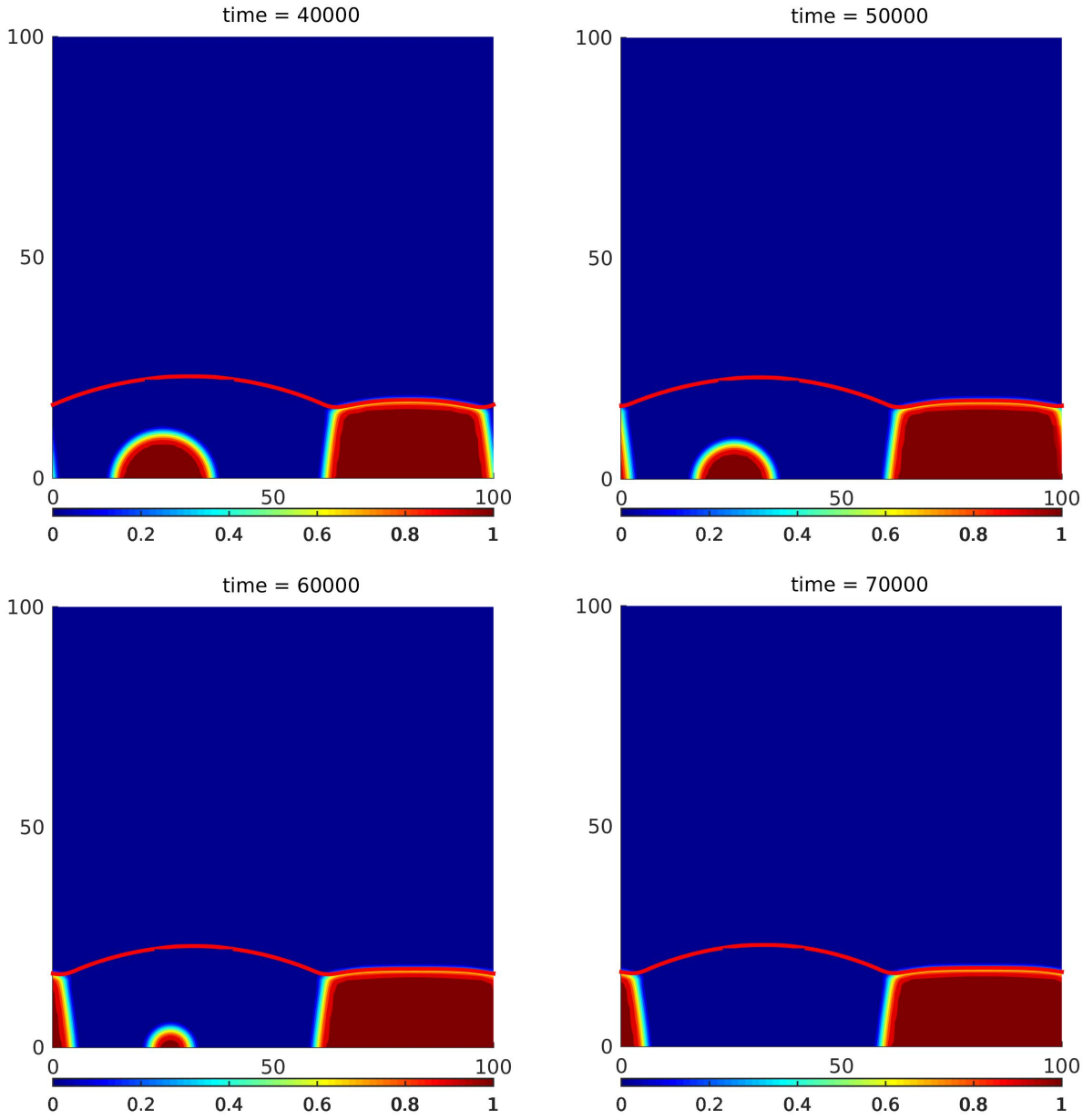

Figure 3.13: We plot the volume fraction of polymer p, ϕ_p, at multiple times with parameters from table 3.7. We see the start of the same qualitative behavior that was previously observed in Figure 3.9, save for the fewer number of regions where there is pure polymer p due to the larger gradient energy coefficients.

Table 3.7: Parameters for Two Dimensional Simulation 2 with Solvent Evaporation

Gradient Energy Coefficients		Mobilities		Densities	
ϵ_{sv}^2	2.00	γ_{sv}	1.0	$\rho_{0,sv}$	0.010
ϵ_{sl}^2	2.00	γ_{sl}	1.0	$\rho_{0,sl}$	1.0
ϵ_{p}^2	2.00	γ_{p}	1.0	$\rho_{0,p}$	1.0
ϵ_{q}^2	2.00	γ_{q}	1.0	$\rho_{0,q}$	1.0

Interaction Parameters	
$\chi_{sv,sl}$	1.7
$\chi_{sv,p}$	1.7
$\chi_{sv,q}$	1.7
$\chi_{sl,p}$	.40
$\chi_{sl,q}$	.90
$\chi_{p,q}$	1.0

Miscellaneous Parameters	
β	1.0
λ	0.001
δ	.001
c	5.0
N_2	89.0
N_3	7.0

Simulation 3

This simulation increases the mobility of the solvent and vapor phase by a factor of 5 and decreases the ϵ_i^2 terms, as listed in Table 3.9. It is quite physical for the mobilities of the solvent to be larger than that of the polymers. We also note that $\alpha_p = -.02$, $\alpha_q = .02$ as in the first simulation. The increased mobility of solvent and vapor allows for faster interface motion, reducing the total time required to remove the solvent in the liquid phase completely, and the decreased ϵ_i^2 terms allow for more interfaces to form. A key difference in this simulation is that instead of the previously used ϕ_i^2 term in the mobility, we use $\phi_{sl}\phi_i$, which in our derivation of the model corresponds to choosing γ_i according to (3.15) for the polymer continuity equations. This results in the polymer continuity equations implemented as

$$\frac{\partial \phi_i(\boldsymbol{x},t)}{\partial t} - \nabla \cdot (\gamma_i \phi_i \phi_{sv}(\boldsymbol{x},t) \nabla \left(\mu_i(\boldsymbol{x},t) + p(\boldsymbol{x},t)\right)) = 0 \quad i = p,q. \tag{3.112}$$

This mobility degenerates as solvent evaporates, which kinetically freezes the polymer in place after the solvent has evaporated. For comparison, consider the images in Figures 3.12 and 3.13, where even though at time $t = 21000$ the solvent has almost been almost completely removed from the system, the polymer is able to diffuse from the left side of the domain to the right side of the domain. In Figures 3.14-3.17 we observe that the degenerate mobility has

Table 3.8: Parameters for Two Dimensional Simulation 3 with Solvent Evaporation

Gradient Energy Coefficients		Mobilities		Densities	
ϵ^2_{sv}	0.700	γ_{sv}	5.0	$\rho_{0,sv}$	0.010
ϵ^2_{sl}	0.700	γ_{sl}	5.0	$\rho_{0,sl}$	1.0
ϵ^2_{p}	0.700	γ_{p}	1.0	$\rho_{0,p}$	1.0
ϵ^2_{q}	0.700	γ_{q}	1.0	$\rho_{0,q}$	1.0

Interaction Parameters	
$\chi_{sv,sl}$	1.7
$\chi_{sv,p}$	1.7
$\chi_{sv,q}$	1.7
$\chi_{sl,p}$	.40
$\chi_{sl,q}$	.90
$\chi_{p,q}$	1.0

Miscellaneous Parameters	
β	1.0
λ	0.001
δ	.001
c	5.0
N_2	89.0
N_3	7.0

frozen the polymer structure once the solvent in the liquid form has been removed from the system. The final structures that result are much more irregular than the pillars that form in the previous simulations. In contrast to the previous simulations, polymer q is plotted.

Simulation 4

This simulation has parameters exactly that of simulation 3 listed in Table 3.9, the only difference being the Cahn-Hilliard mobility is $\gamma_i\phi_i^2$ instead of $\gamma_i\phi_i\phi_{sl}$. We see again in Figures 3.18-3.21 that if the mobilities do not degenerate as the solvent in the liquid phase exits the polymer mixture, we get the more regular pillar-like structures. Here $\alpha_p = -.014$, $\alpha_q = .014$. Again, polymer q is plotted.

3.5 Future Directions

There are a wealth of directions that one could develop further on this model. We briefly remark to the varying constitutive relations, especially for the velocities, that are referenced in 2.4. Here, we consider a new numerical approximation by altering the time discretization, and show the advantage of this discretization in computation.

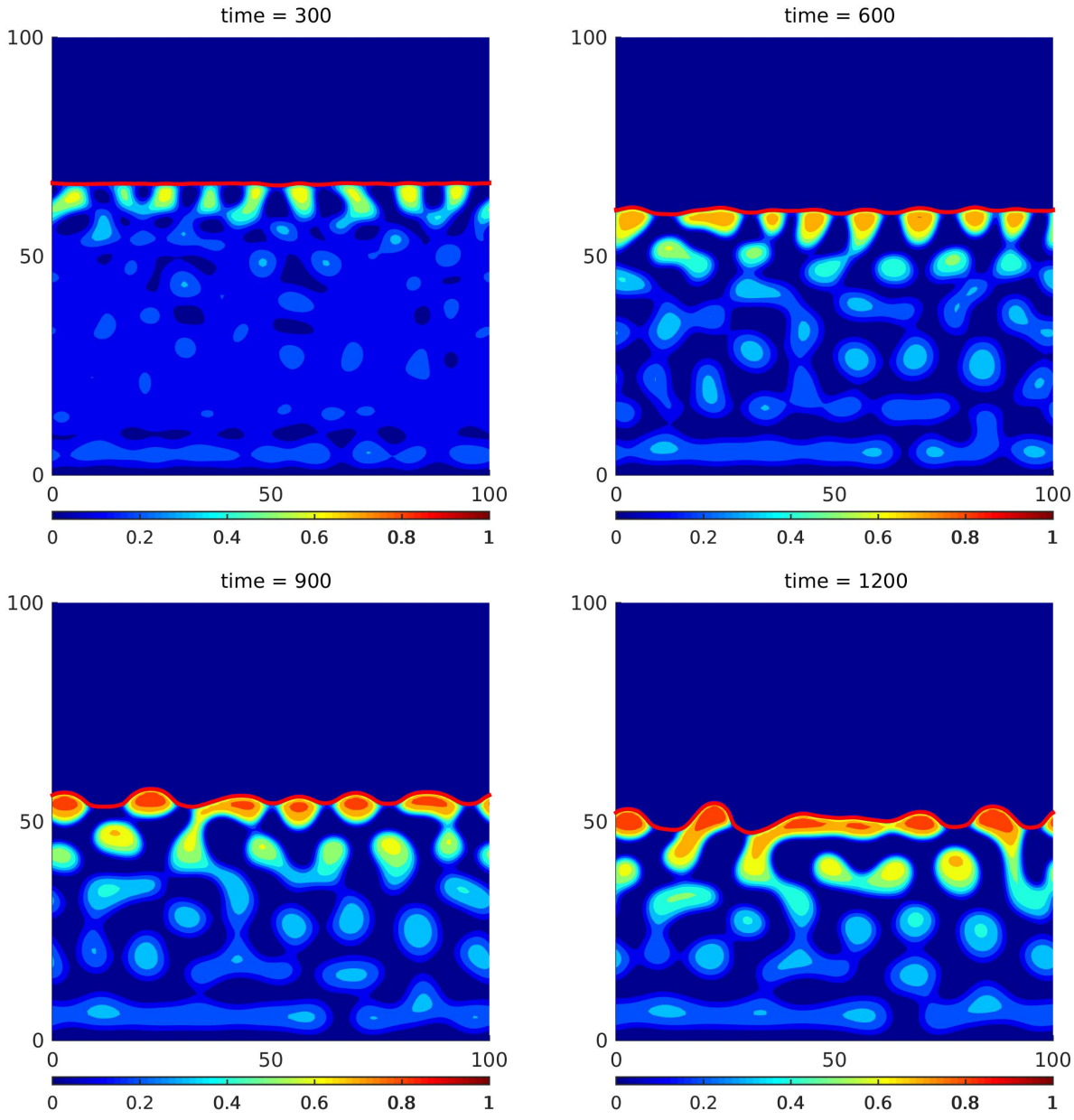

Figure 3.14: We plot the volume fraction of polymer q, ϕ_q, at multiple times with parameters from Table 3.8. As the solvent is removed from the system, the mobility begins to degenerate (see (3.112)) for all components except the vapor phase, which results in the structure of the polymer to become frozen in place. We observe much more irregular structures compared to the previous simulations.

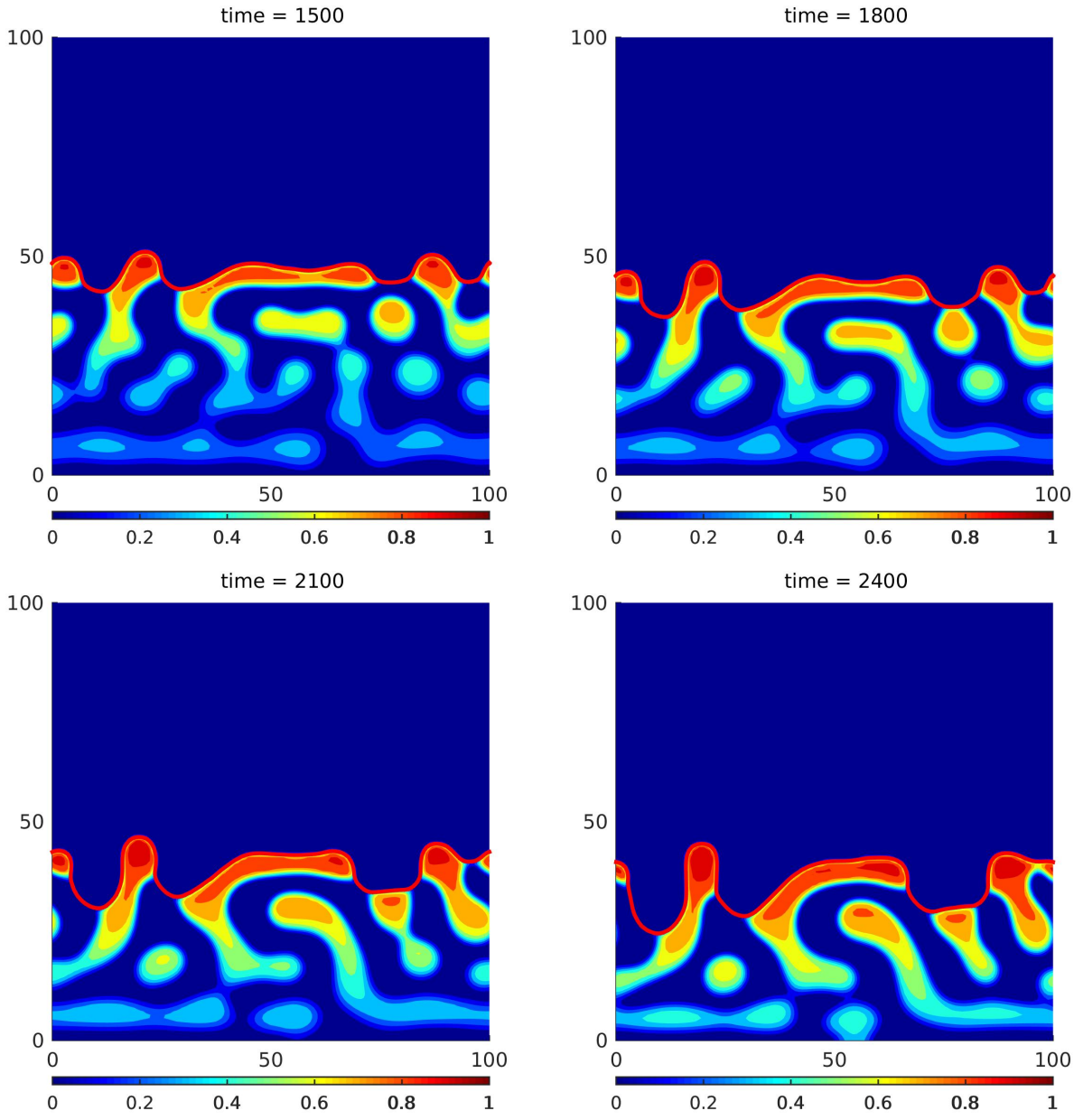

Figure 3.15: We plot the volume fraction of polymer q, ϕ_q, at multiple times with parameters from Table 3.8. As the solvent is removed from the system, the mobility begins to degenerate (see (3.112)) for all components except the vapor phase, which results in the structure of the polymer to become frozen in place. We observe much more irregular structures compared to the previous simulations.

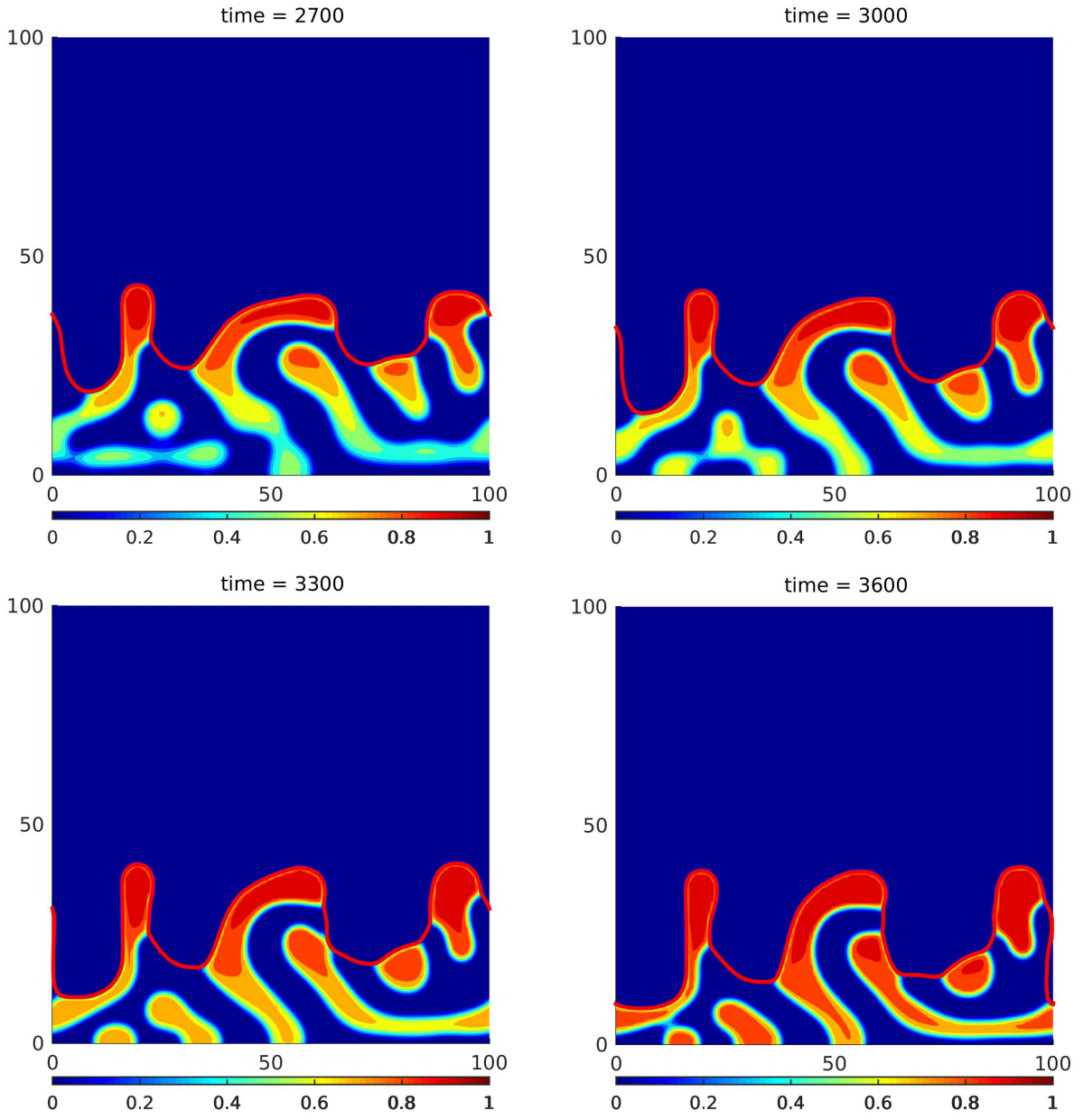

Figure 3.16: We plot the volume fraction of polymer q, ϕ_q, at multiple times with parameters from Table 3.8. As the solvent is removed from the system, the mobility begins to degenerate (see (3.112)) for all components except the vapor phase, which results in the structure of the polymer to become frozen in place. We observe much more irregular structures compared to the previous simulations.

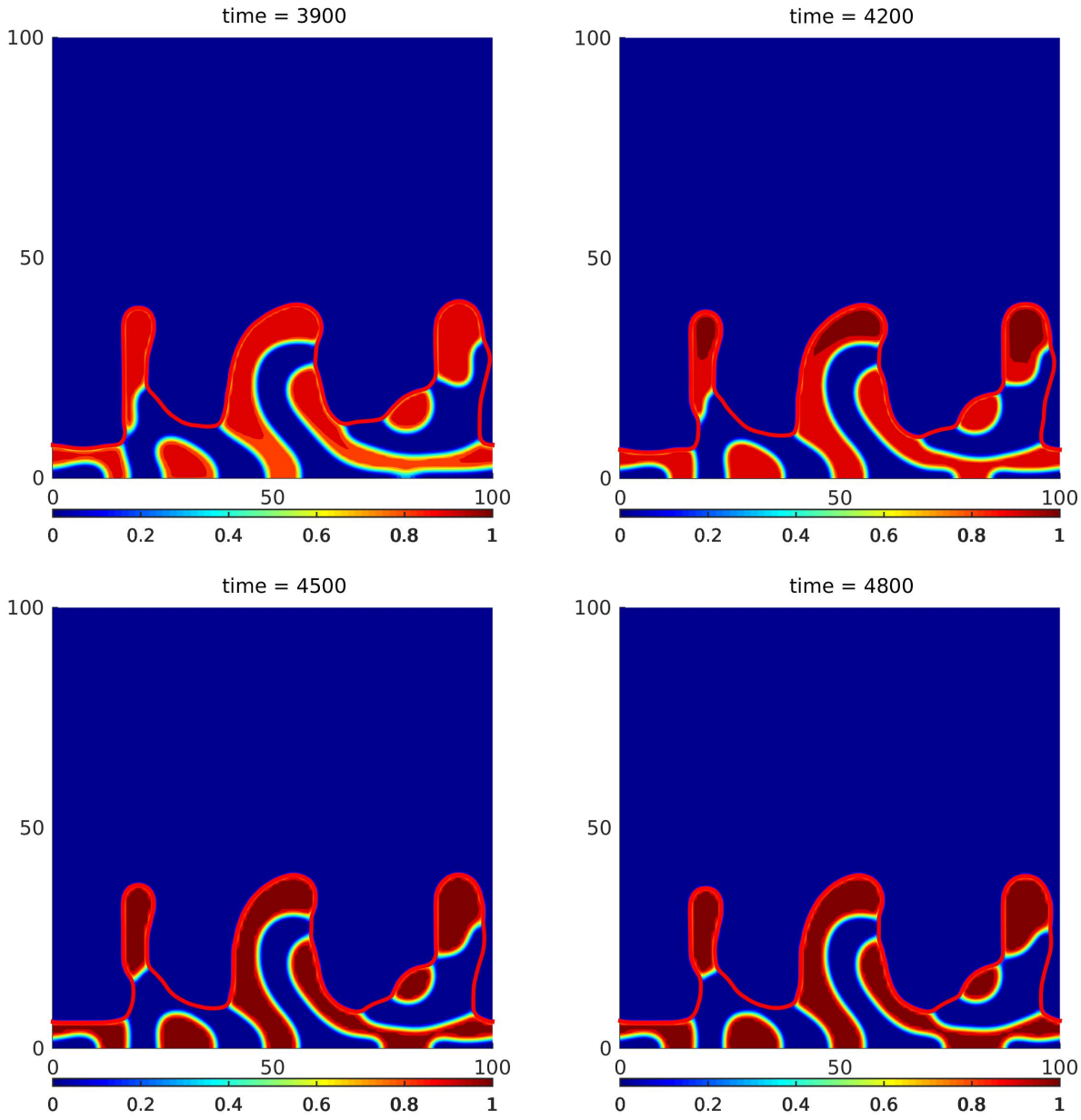

Figure 3.17: We plot the volume fraction of polymer q, ϕ_q, at multiple times with parameters from Table 3.8. As the solvent is removed from the system, the mobility begins to degenerate (see (3.112)) for all components except the vapor phase, which results in the structure of the polymer to become frozen in place. We observe much more irregular structures compared to the previous simulations.

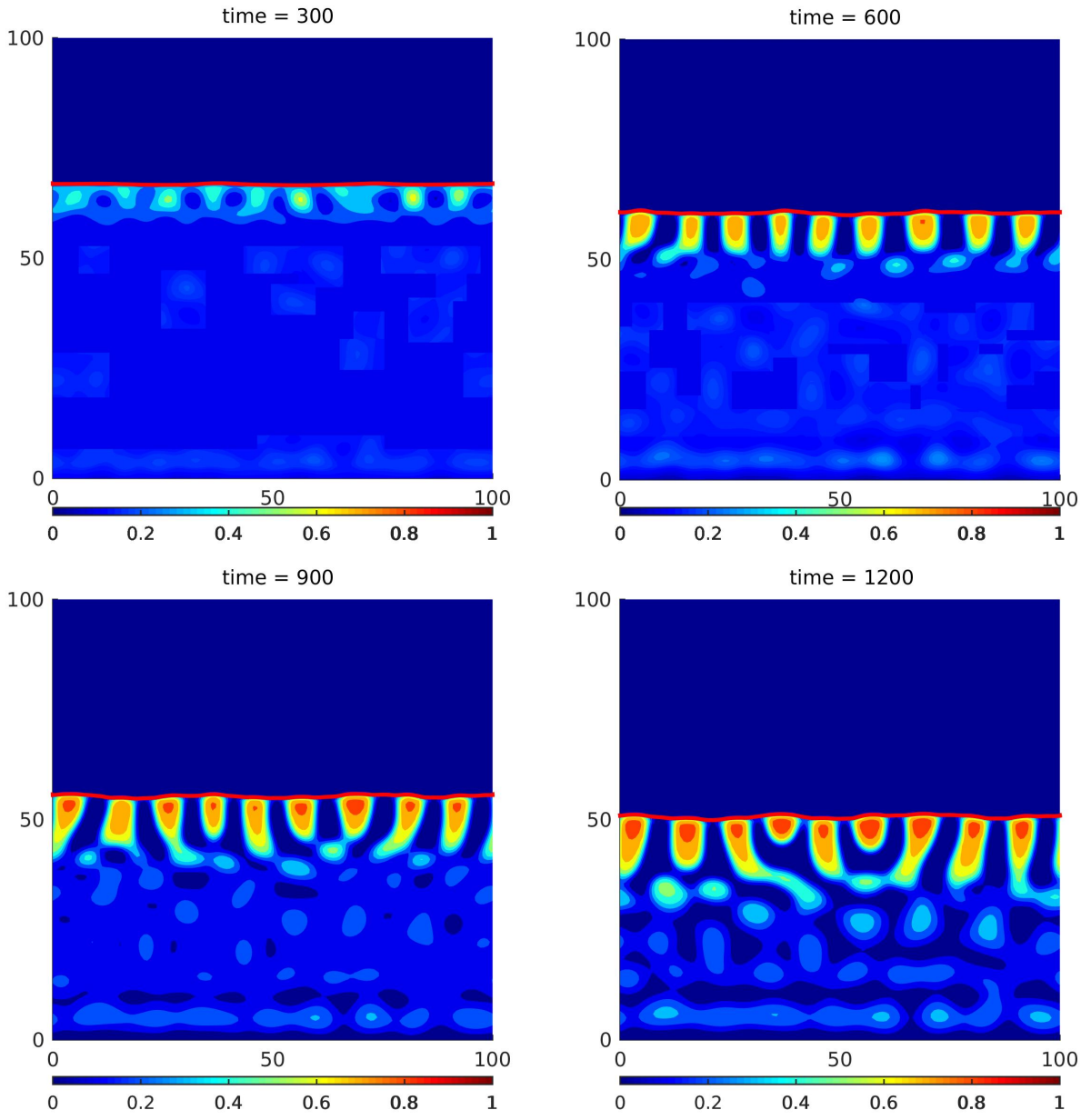

Figure 3.18: We plot the volume fraction of polymer q, ϕ_q, at multiple times with parameters from Table 3.9. With lower gradient energy terms than the simulation shown in Figures 3.9-3.10, the structure of the polymer has more interfaces. Also of note is the difference in structures to the simulation in Figures 3.14-3.17 resulting from the mobility which does not degenerate as the solvent in the liquid phase is removed from the system.

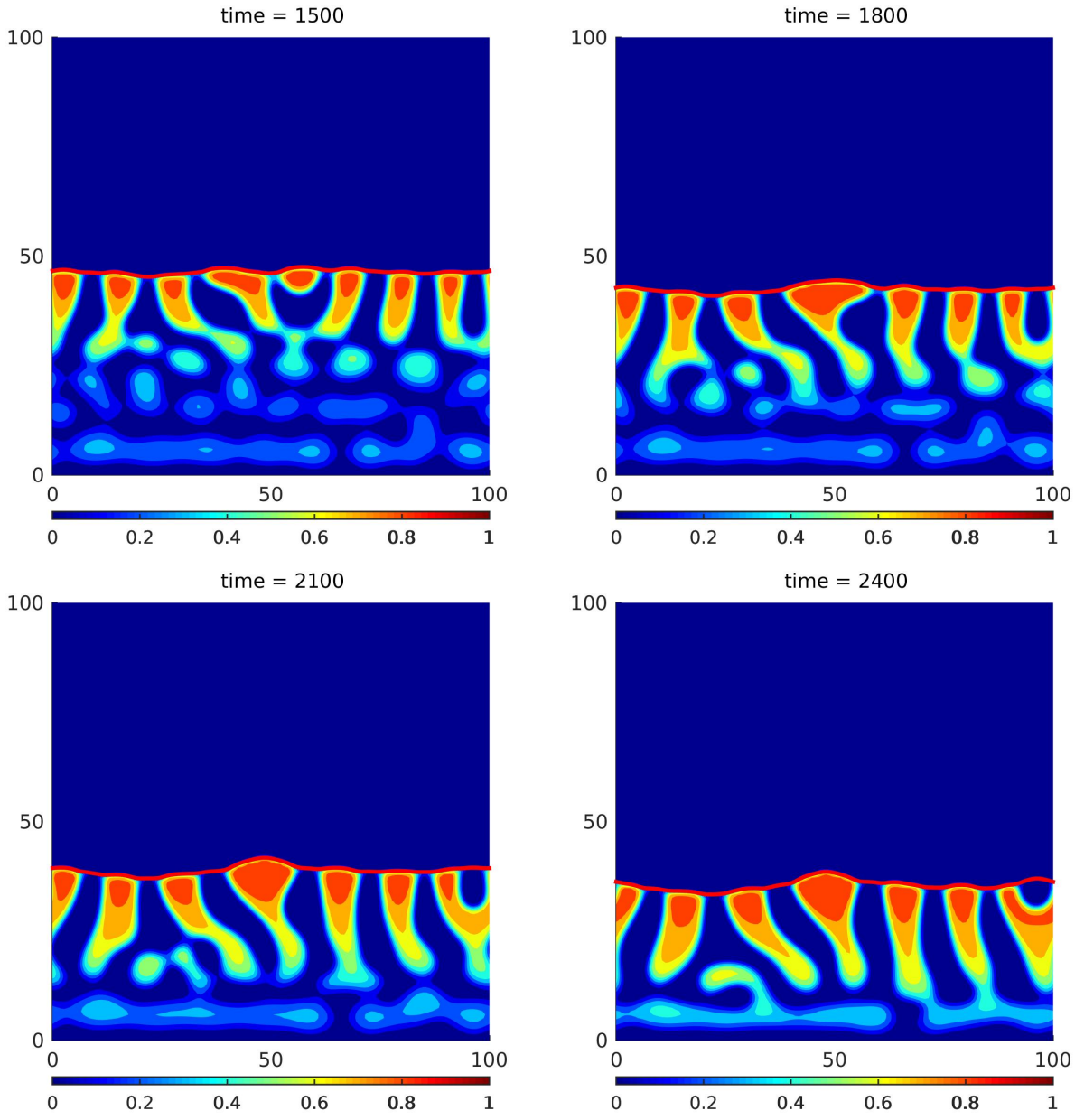

Figure 3.19: We plot the volume fraction of polymer q, ϕ_q, at multiple times with parameters from Table 3.9. With lower gradient energy terms than the simulation shown in Figures 3.9-3.10, the structure of the polymer has more interfaces. Also of note is the difference in structures to the simulation in Figures 3.14-3.17 resulting from the mobility which does not degenerate as the solvent in the liquid phase is removed from the system.

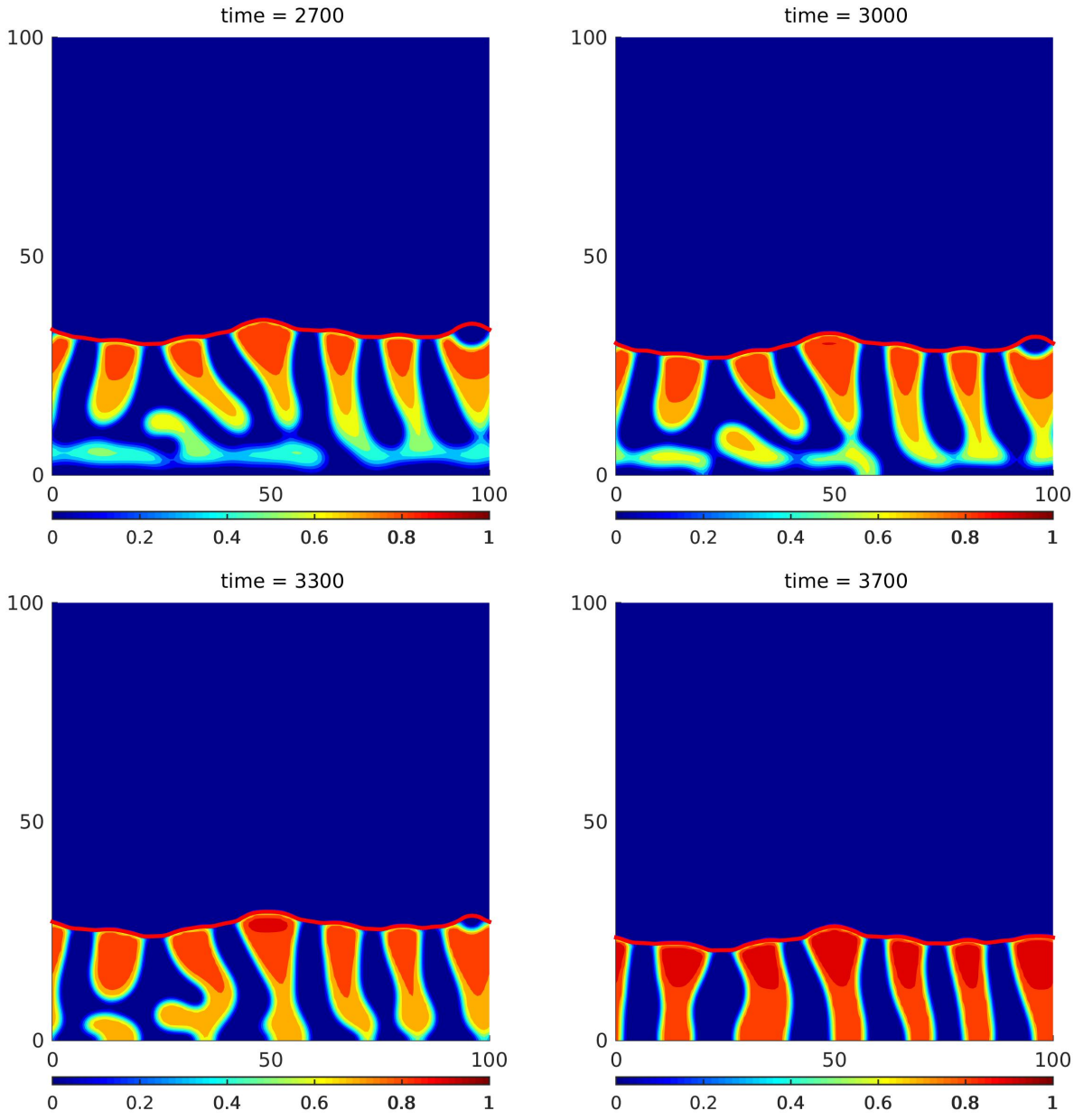

Figure 3.20: We plot the volume fraction of polymer q, ϕ_q, at multiple times with parameters from Table 3.9. With lower gradient energy terms than the simulation shown in Figures 3.9-3.10, the structure of the polymer has more interfaces. Also of note is the difference in structures to the simulation in Figures 3.14-3.17 resulting from the mobility which does not degenerate as the solvent in the liquid phase is removed from the system.

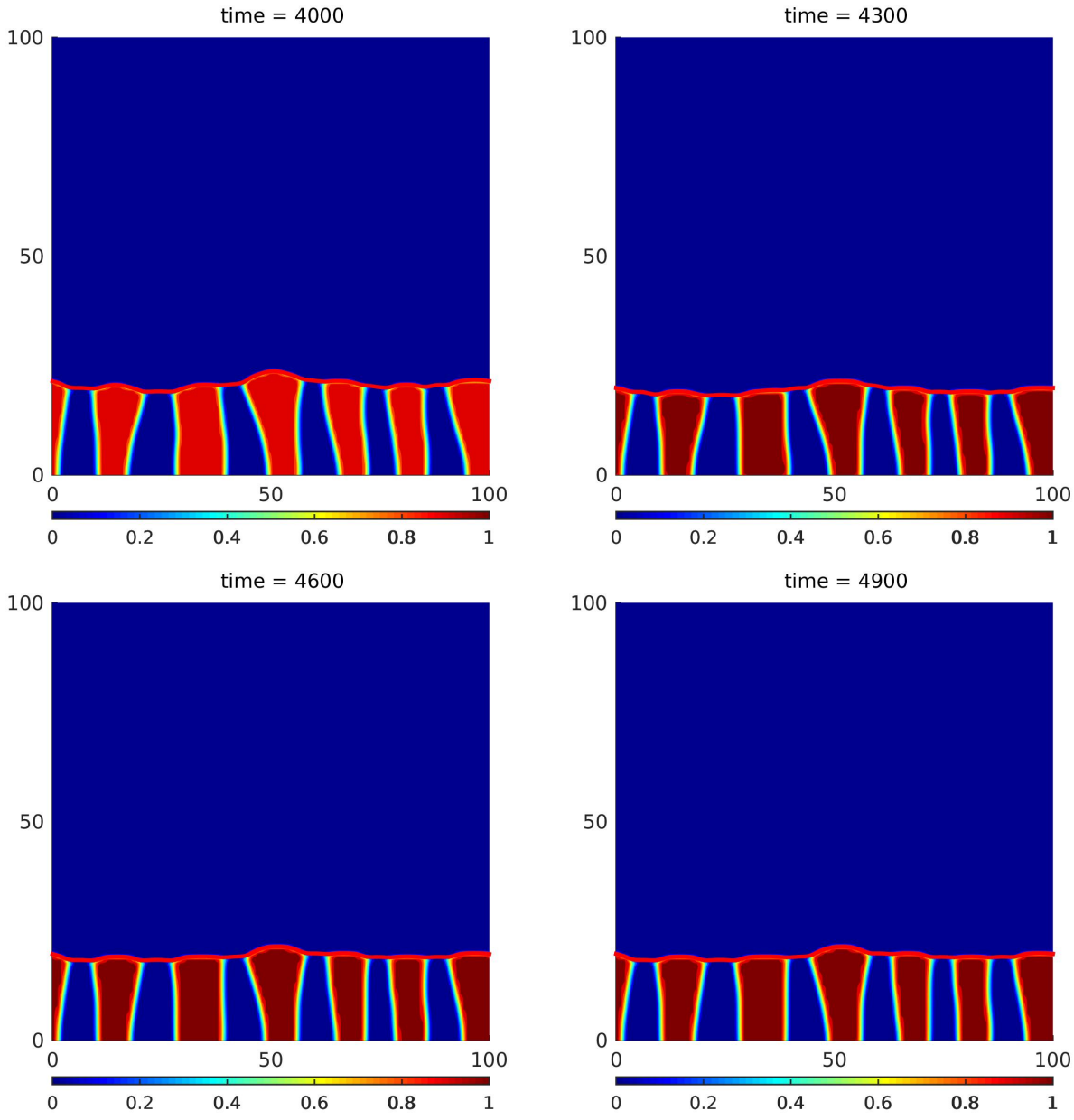

Figure 3.21: We plot the volume fraction of polymer q, ϕ_q, at multiple times with parameters from Table 3.9. With lower gradient energy terms than the simulation shown in Figures 3.9-3.10, the structure of the polymer has more interfaces. Also of note is the difference in structures to the simulation in Figures 3.14-3.17 resulting from the mobility which does not degenerate as the solvent in the liquid phase is removed from the system.

Table 3.9: Parameters for Two Dimensional Simulation 4 with Solvent Evaporation

Gradient Energy Coefficients		Mobilities		Densities	
ϵ_{sv}^2	0.700	γ_{sv}	5.0	$\rho_{0,sv}$	0.010
ϵ_{sl}^2	0.700	γ_{sl}	5.0	$\rho_{0,sl}$	1.0
ϵ_{p}^2	0.700	γ_{p}	1.0	$\rho_{0,p}$	1.0
ϵ_{q}^2	0.700	γ_{q}	1.0	$\rho_{0,q}$	1.0

Interaction Parameters	
$\chi_{sv,sl}$	1.7
$\chi_{sv,p}$	1.7
$\chi_{sv,q}$	1.7
$\chi_{sl,p}$	.40
$\chi_{sl,q}$	.90
$\chi_{p,q}$	1.0

Miscellaneous Parameters	
β	1.0
λ	0.001
δ	.001
c	5.0
N_2	89.0
N_3	7.0

3.5.1 A New Semi-Implicit Method

We now discuss a method which treats the nonlinear logarithmic term implicitly. We discretize the equations as

$$\phi_{sl}^{n+1} - s\nabla\cdot\left(M_{sl}(\boldsymbol{\phi}^n)\nabla\mu_{sl}^{n+1}\right) = \phi_{sl}^n + s\nabla\cdot(M_{sl}(\boldsymbol{\phi}^n)\nabla p^n) - s\rho_{sl}^{-1}\lambda\left(\rho_{sl}^{-1}\mu_{sl}^n + (\rho_{sl}^{-1}-\rho_{sv}^{-1})p^n\right) \tag{3.113}$$

$$\phi_{i}^{n+1} - s\nabla\cdot\left(M_{i}(\boldsymbol{\phi}^n)\nabla\mu_{i}^{n+1}\right) = \phi_{i}^n + s\nabla\cdot(M_{i}(\boldsymbol{\phi}^n)p^n) \quad i=p,q \tag{3.114}$$

$$\mu_i^{n+1} + (\epsilon_i^2+\epsilon_{sv}^2)\Delta\phi_i^{n+1} - \frac{\partial f_h(\boldsymbol{\phi}^{n+1},\boldsymbol{\phi}^n)}{\partial\phi_i} = -\epsilon_{sv}^2\Delta\left(\sum_{j\neq sv,i}\phi_j^n\right) \tag{3.115}$$

$$f_h(\boldsymbol{\phi}^{n+1},\boldsymbol{\phi}^n) = \sum_{i\in I}\phi_i^{n+1}\ln_\delta(\phi_i^{n+1}) + \sum_{i\neq j}\chi_{ij}\phi_i^n\phi_j^n - c\phi_{sv}^n; \qquad \phi_{sv} = 1-\sum_{i\neq sv}\phi_i \tag{3.116}$$

$$\sum_i \nabla\cdot\left(M_i(\boldsymbol{\phi}^n)\nabla p^{n+1}\right)+\lambda\left(\rho_{0,sl}^{-1}-\rho_{0,sv}^{-1}\right)^2 p^{n+1} = -\sum_{i\neq sv}\nabla\cdot(M_i(\boldsymbol{\phi}^n)\nabla\mu_i^n)-\lambda\rho_{0,sl}^{-1}(\rho_{0,sl}^{-1}-\rho_{0,sv}^{-1})\mu_{sl}^n. \tag{3.117}$$

The inspiration for this time discretization relates to convex splitting techniques developed by Eyre [20], which are well known to have desirable energy stability properties. In the homogeneous free energy, the convex terms of the form $\phi\ln(\phi)$ are treated implicitly in time, while the non-convex terms are treated explicitly in time. This discretization leads to a system of nonlinear partial differential equations at each time step, as opposed to the previously described system (3.80)-(3.84) which is linear. The FAS multigrid method that was implemented for previous simulations is designed for the solution of nonlinear systems [50, 54]. All that is needed is an appropriate smoother. With the time discretization done as in (3.113)-(3.117), and spatial discretization as done previously in this section, development of a smoother leads to a nonlinear system that is, with the exception of the nonlinear term, decoupled into three 2x2 blocks representing the Cahn-Hilliard equations and a 1x1 block for the pressure Poisson equation. We use a local Newton approximation to the nonlinearity so as to approximate the system as a linear system. We define

$$G_i^I(\boldsymbol{\phi}) = \frac{\partial}{\partial\phi_i}\sum_{k\in I}\phi_k\ln_\delta(\phi_k) \tag{3.118}$$

$$G_i^E(\boldsymbol{\phi}) = \frac{\partial}{\partial\phi_i}\left(\sum_{k\neq j}\chi_{kj}\phi_k\phi_j - c\cdot\phi_{sv}\right) \tag{3.119}$$

and

$$\frac{\partial f_h(\boldsymbol{\phi}^{n+1},\boldsymbol{\phi}^n)}{\partial\phi_i} = G_i^I(\boldsymbol{\phi}^{n+1})+G_i^E(\boldsymbol{\phi}^n). \tag{3.120}$$

With these definitions we rewrite (3.115) as

$$\mu_i^{n+1}+(\epsilon_i^2+\epsilon_{sv}^2)\Delta\phi_i^{n+1}-G_i^I(\boldsymbol{\phi}^{n+1}) = -\epsilon_{sv}^2\Delta\left(\sum_{j\neq sv,i}\phi_j^n\right)+G_i^E(\boldsymbol{\phi}^n). \tag{3.121}$$

Let $\boldsymbol{\phi}^{n+1,l+1}$ be the $l+1$ Gauss-Seidel iterate. We make the linear approximation

$$G_i^I(\boldsymbol{\phi}^{n+1,l+1}) \approx G_i^I(\boldsymbol{\phi}^{n+1,l}) + \frac{\partial G_i^I(\boldsymbol{\phi}^{n+1,l})}{\partial \phi_i}\left(\phi_i^{n+1,l+1} - \phi_i^{n+1,l}\right). \tag{3.122}$$

We then smooth, using the notation from 3.3.2, as

$$\mu_i^{n+1,l+1}(j,k) - \left(\frac{4(\epsilon_i^2 + \epsilon_{sv}^2)}{h^2} - \frac{\partial G_i^I(\boldsymbol{\phi}^{n+1,l})}{\partial \phi_i}\right)\phi_i^{n+1,l+1}(j,k) = RHS \tag{3.123}$$

coupled with the other equations in the same manner as done in 3.3.2. Notice that in the Newton-like approximation 3.122 we do *not* include the entire gradient, as typically one writes

$$F(\boldsymbol{x}^{l+1}) \approx F(\boldsymbol{x}^l) + \nabla F(\boldsymbol{x}^l) \cdot \left(\boldsymbol{x}^{l+1} - \boldsymbol{x}^l\right). \tag{3.124}$$

If one uses (3.124), then the 7x7 system of equations that result in the smoother no longer has the block structure previously described, which is one of the advantages in this discretization.

Not only is this discretization easier to implement than the discretization used in 3.3.2, but it is also more stable in the sense that the allowable time step is much larger. When using parameters in Table 3.9 on a base 64x64 mesh with 2 levels of adaptive refinement, shown in Figure 3.22 with this discretization we can take time steps on the order of 10^{-2}. In the previous simulations with a 64 by 64 base grid and 1 level of adaptive refinement we could take time steps no larger than 10^{-3}. Further development for this method such as higher order methods in time and sophisticated a-posteriori error estimators could increase accuracy and efficiency of these simulations tremendously.

3.6 Conclusions

Via an application of the general mixture model developed in Chapter 2 we have presented a framework for studying a system of a quaternary mixture with a volatile, evaporating component by using energetic variational techniques which results in a Cahn-Hilliard-like diffuse interface model. This mathematical model is developed with the processing of the active layer of OPVs in mind, where a mixture of a volatile solvent and two polymers

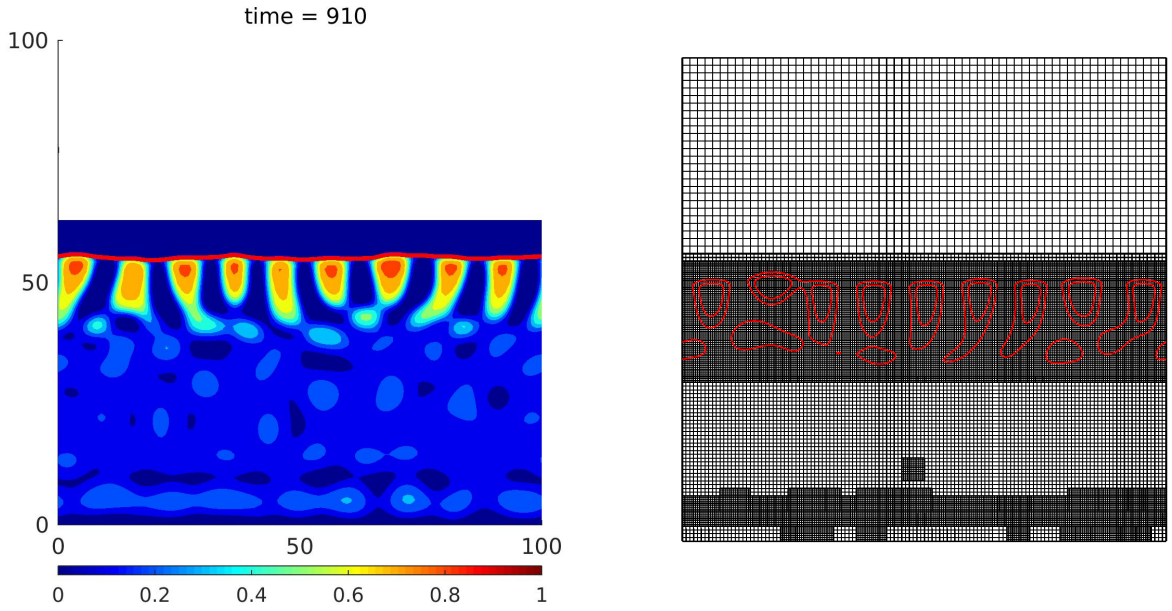

(a) Contour Plot

(b) Mesh

Figure 3.22: We plot ϕ_q on an adaptive mesh which has a base level of 64 by 64 cells and 2 levels of adaptive refinement with parameters from Table 3.9. On the left we see similar behavior to Figure 3.18. On the right we plot the adaptive mesh with red contour lines to indicate $\phi_q = .3, .7$.

phase separate while the solvent evaporates. The model is general enough to include density differences the components of the volatile solvent in its liquid and vapor phases as well as the parameters that are typically needed to model such a system, such as the Flory-interaction parameters, gradient energy coefficients, and boundary energy terms. We demonstrate that, through a unique set of flow boundary conditions and source and sink terms, we are able to adjust the parameters that directly affect the speed of the interface location between the polymer mixture and the vapor phase. We implement a semi-implicit method for approximating the solution through cell-centered finite differences which are first order in time, second order in space. The result is a large, sparse system of linear equations which we solve using FAS multigrid using BSAM. After demonstrating the time evolution of multiple microstructures with different parameters, we introduce a future direction of a new discretization which offers greater stability.

Chapter 4

Future Application: Ionic Fluids

4.1 Modeling Ionic Fluids

Consider now that we have a mixture where the components are charged under some electric field. We define ε_0 is the (constant) vacuum permittivity, $\varepsilon_r(\boldsymbol{\phi})$ to be the relative permittivity of the system, which we assume may depend on the volume fractions, and ϱ_e is the charge density. We assume that the charge density has the form

$$\begin{aligned} \varrho_e(\boldsymbol{x}, t) &= \varrho_{0,e}(\boldsymbol{x}) + \sum_{i=0}^{N} e z_i \rho_i(\boldsymbol{x}, t) \\ &= \varrho_{0,e}(\boldsymbol{x}) + \sum_{i=0}^{N} e z_i \rho_{0,i} \phi_i(\boldsymbol{x}, t) \end{aligned} \tag{4.1}$$

where e is the charge of an electron, z_i is the (signed) valency, and $\varrho_{0,e}$ is the fixed charge density of the system. We define

$$\varepsilon(\boldsymbol{\phi}(\boldsymbol{x}, t)) = \varepsilon_0 \varepsilon_r(\boldsymbol{\phi}(\boldsymbol{x}, t)). \tag{4.2}$$

We define the electrostatic contribution to the Helmholtz free energy of the system to be

$$E_{\text{elec}}(t) = \int_\Omega \varrho_e(\boldsymbol{x}, t)\psi(\boldsymbol{x}, t) - \frac{\varepsilon(\boldsymbol{\phi}(\boldsymbol{x}, t))}{2} |\nabla \psi(\boldsymbol{x}, t)|^2 d\boldsymbol{x} - \int_{\partial\Omega} \frac{\varepsilon(\boldsymbol{\phi}(\boldsymbol{x}, t))}{2\eta} (\psi(\boldsymbol{x}, t) - \psi_0(\boldsymbol{x}))^2 dS \tag{4.3}$$

where η is a length parameter and ψ is the electrostatic potential. Similar to previous sections, consider taking the time derivative of the electrostatic free energy as

$$\begin{aligned}\frac{dE_{\text{elec}}}{dt} &= \int_\Omega \left(\varrho_e \frac{\partial \psi}{\partial t} + \psi \frac{\partial \varrho_e}{\partial t}\right) d\boldsymbol{x} \\ &+ \int_\Omega -\varepsilon(\boldsymbol{\phi}) \nabla\psi \cdot \nabla \frac{\partial \psi}{\partial t} - \frac{1}{2}|\nabla\psi|^2 \sum_{i=0}^{N} \frac{\partial \varepsilon(\boldsymbol{\phi})}{\partial \phi_i} \frac{\partial \phi_i}{\partial t} d\boldsymbol{x} \\ &- \int_{\partial\Omega} \frac{(\psi - \psi_0(\boldsymbol{x}))^2}{2\eta} \sum_{i=0}^{N} \frac{\partial \varepsilon(\boldsymbol{\phi})}{\partial \phi_i} \frac{\partial \phi_i}{\partial t} dS \\ &- \int_{\partial\Omega} \frac{\varepsilon(\boldsymbol{\phi})}{\eta} (\psi - \psi_0(\boldsymbol{x})) \frac{\partial \psi}{\partial t} dS.\end{aligned} \tag{4.4}$$

Via integration by parts

$$\begin{aligned}-\int_\Omega \varepsilon(\boldsymbol{\phi}) \nabla\psi(\boldsymbol{x},t) \cdot \nabla \frac{\partial \psi(\boldsymbol{x},t)}{\partial t} d\boldsymbol{x} &= \int_\Omega \frac{\partial \psi(\boldsymbol{x},t)}{\partial t} \nabla \cdot \varepsilon(\boldsymbol{\phi}) \nabla\psi(\boldsymbol{x},t) d\boldsymbol{x} \\ &- \int_{\partial\Omega} \frac{\partial \psi(\boldsymbol{x},t)}{\partial t} \varepsilon(\boldsymbol{\phi}) \nabla\psi \cdot \boldsymbol{n} dS.\end{aligned} \tag{4.5}$$

After applying this to 4.4 and the specific form for the charge density when time derivatives are needed, we have that

$$\begin{aligned}\frac{dE_{\text{elec}}}{dt} &= \int_\Omega \left[\nabla \cdot (\varepsilon(\boldsymbol{\phi}) \nabla\psi) + \varrho_e\right] \frac{\partial \psi}{\partial t} d\boldsymbol{x} \\ &+ \int_\Omega \sum_{i=0}^{N} \left[-\frac{\partial \varepsilon(\boldsymbol{\phi})}{\partial \phi_i} \frac{|\nabla\psi|^2}{2} + \psi e z_i \rho_{0,i}\right] \frac{\partial \phi_i}{\partial t} d\boldsymbol{x} \\ &+ \int_{\partial\Omega} \left[-\frac{\varepsilon(\boldsymbol{\phi})}{\eta} (\psi - \psi_0) - \varepsilon(\boldsymbol{\phi}) \nabla\psi \cdot \boldsymbol{n}\right] \frac{\partial \psi}{\partial t} dS \\ &+ \int_{\partial\Omega} -\sum_{i=0}^{N} \frac{\partial \varepsilon(\boldsymbol{\phi})}{\partial \phi_i} \frac{(\psi - \psi_0)^2}{2\eta} \frac{\partial \phi_i}{\partial t} dS.\end{aligned} \tag{4.6}$$

The energy that will be considered in this application is the electrochemical energy

$$E = E_{\text{chem}} + E_{\text{elec}} \tag{4.7}$$

where the chemical energy is

$$E_{\text{chem}}(t) = \int_\Omega f_h(\boldsymbol{\phi}) + \sum_{i=0}^{N} \frac{\epsilon_i^2}{2} |\nabla \phi_i|^2 d\boldsymbol{x}. \tag{4.8}$$

The time derivative of the total free energy is then

$$\begin{aligned}
\frac{dE}{dt} = & \int_\Omega \left[\nabla \cdot (\varepsilon(\boldsymbol{\phi})\nabla\psi) + \varrho_e\right] \frac{\partial \psi}{\partial t} d\boldsymbol{x} \\
& + \int_\Omega \sum_{i=0}^{N} \left[\frac{\partial f_h(\boldsymbol{\phi})}{\partial \phi_i} - \epsilon_i^2 \Delta \phi_i - \frac{\partial \varepsilon(\boldsymbol{\phi})}{\partial \phi_i} \frac{|\nabla\psi|^2}{2} + \psi e z_i \rho_{0,i}\right] \frac{\partial \phi_i}{\partial t} d\boldsymbol{x} \\
& + \int_{\partial\Omega} \left[-\frac{\varepsilon(\boldsymbol{\phi})}{\eta}(\psi - \psi_0) - \varepsilon(\boldsymbol{\phi})\nabla\psi \cdot \boldsymbol{n}\right] \frac{\partial \psi}{\partial t} dS \\
& + \int_{\partial\Omega} \sum_{i=0}^{N} \left[\epsilon_i^2 \nabla\phi_i \cdot \boldsymbol{n} - \frac{\partial \varepsilon(\boldsymbol{\phi})}{\partial \phi_i} \frac{(\psi - \psi_0)^2}{2\eta}\right] \frac{\partial \phi_i}{\partial t} dS.
\end{aligned} \tag{4.9}$$

We assume locally near the boundary the system is in thermodynamic equilibrium, which implies that

$$\begin{aligned}
0 &= \frac{\varepsilon(\boldsymbol{\phi})}{\eta}(\psi - \psi_0) + \varepsilon(\boldsymbol{\phi})\nabla\psi \cdot \boldsymbol{n} \\
&= \frac{\varepsilon(\boldsymbol{\phi})}{\eta}(\psi - \psi_0 + \eta\nabla\psi \cdot \boldsymbol{n})
\end{aligned} \tag{4.10}$$

and

$$\epsilon_i^2 \nabla\phi_i \cdot \boldsymbol{n} - \epsilon_0^2 \nabla\phi_0 \cdot \boldsymbol{n} - \frac{(\psi - \psi_0)^2}{2\eta}\left(\frac{\partial \varepsilon(\boldsymbol{\phi})}{\partial \phi_i} - \frac{\partial \varepsilon(\boldsymbol{\phi})}{\partial \phi_0}\right) = 0. \tag{4.11}$$

We take the quasi-steady assumption for the electric potential, so that

$$\nabla \cdot (\varepsilon(\boldsymbol{\phi})\nabla\psi) + \varrho_e = 0 \tag{4.12}$$

which is the well known Poisson equation for the electrostatic potential. We define the electrochemical potential associated with this energy is

$$\mu_i = -\frac{1}{2}\frac{\partial \varepsilon(\boldsymbol{\phi})}{\partial \phi_i}|\nabla\psi|^2 + \psi e z_i \rho_{0,i} + \frac{\partial f_h(\boldsymbol{\phi})}{\partial \phi_i} - \epsilon_i^2 \Delta\phi_i \tag{4.13}$$

We now consider a mixture of a polymer which carries a negative charge and its counterion. Let $\phi_c(\boldsymbol{x},t)$, $\phi_p(\boldsymbol{x},t)$ be the volume fraction of the counterion and polymer, respectively, and we define the index set $J=\{c,p\}$. We make the assumption that the densities are matched, $\rho_0=\rho_{0,p}=\rho_{0,c}$, and that the valencies are $z_p=-1, z_c=+1$ so that the polymer is carrying the negative charge. We have then that the electrostatic equations and boundary conditions are

$$\begin{aligned}-\nabla\cdot(\varepsilon(\boldsymbol{\phi})\nabla\psi) &= \varrho_e \\ &= \varrho_{0,e}+\sum_J ez_i\rho_i \\ &= e\rho_0\left(2\phi_c-1\right)\end{aligned} \tag{4.14}$$

$$\frac{\varepsilon(\boldsymbol{\phi})}{\eta}\left[(\psi-\psi_0)+\eta\nabla\psi\cdot\boldsymbol{n}\right]=0 \tag{4.15}$$

$$-\left(\frac{\partial\varepsilon(\boldsymbol{\phi})}{\partial\phi_c}-\frac{\partial\varepsilon(\boldsymbol{\phi})}{\partial\phi_p}\right)\frac{(\psi-\psi_0)^2}{2\eta}+\left(\epsilon_p^2+\epsilon_c^2\right)\nabla\phi_c\cdot\boldsymbol{n}=0 \tag{4.16}$$

where in (4.16) we have used the no voids assumption (2.45). We assume advective-type fluxes (2.4), that the source terms are zero ($S_i=0$) and the boundary velocities are either zero or periodic. After introducing the Lagrange multiplier p (2.25) we have

$$\frac{dE}{dt}=\sum_{i\in J}\int_\Omega \phi_i\nabla\left(\mu_i+p\right)\cdot\boldsymbol{u}_i d\boldsymbol{x} \tag{4.17}$$

where μ_i is now the electrochemical potential introduced in (4.13). We make the thermodynamically consistent choice for the velocities

$$\boldsymbol{u}_i=-\gamma_i\phi_i\nabla\left(\mu_i+p\right) \tag{4.18}$$

where $\gamma_i>0$. We define $\widetilde{\mu}_c=\mu_c-\mu_0$ and $\widetilde{p}=\mu_p+p$, similar to section 2.2.2 with

$$\widetilde{\varepsilon}(\phi_c)=\varepsilon(\phi_c,1-\phi_c)\quad \widetilde{f}_h(\phi_c)=f_h(\phi_c,1-\phi_c), \tag{4.19}$$

and we assume a linear dependence of ε on the concentration so that

$$\begin{aligned}\widetilde{\varepsilon}(\phi_c) &= \varepsilon_c\phi_c + \varepsilon_p(1-\phi_c)\\ &= \varepsilon_p + (\varepsilon_c - \varepsilon_p)\,\phi_c\end{aligned} \tag{4.20}$$

where $\varepsilon_c, \varepsilon_p$ are constants. After eliminating tildes we have that

$$\frac{\partial \phi_c}{\partial t} - \nabla\cdot\left(\gamma_c\phi_c^2\nabla\left(\mu_c + p\right)\right) = 0 \tag{4.21}$$

$$-\nabla\cdot\left(\gamma_c\phi_c^2\nabla\mu_c\right) - \nabla\left(\left(\gamma_c\phi_c^2 + \gamma_p(1-\phi_c)^2\right)\nabla p\right) = 0 \tag{4.22}$$

$$\mu_c = -\varepsilon'(\phi_c)\frac{|\nabla\psi|^2}{2} + 2e\rho_0\psi + f_h'(\phi_c) - (\epsilon_c^2 + \epsilon_p^2)\Delta\phi_i. \tag{4.23}$$

$$-\nabla\cdot(\varepsilon(\phi_c)\nabla\psi) = e\rho_0\left(2\phi_c - 1\right) \tag{4.24}$$

4.2 Nondimensionalization

Let $L\widetilde{\boldsymbol{x}} = \boldsymbol{x}, \tau\widetilde{t} = t$ where L, τ are characteristic length and times. We define the nondimensional chemical potential, pressure, and electrostatic potential as

$$\begin{aligned}\widetilde{\mu}_i(\widetilde{\boldsymbol{x}},\widetilde{t}) &= \frac{\mu_i(L\widetilde{\boldsymbol{x}},\tau\widetilde{t})}{\rho_0 kT}\\ \widetilde{p}(\widetilde{\boldsymbol{x}},\widetilde{t}) &= \frac{p(L\widetilde{\boldsymbol{x}},\tau\widetilde{t})}{\rho_0 kT}\\ \widetilde{\psi}(\widetilde{\boldsymbol{x}},\widetilde{t}) &= \frac{e}{kT}\psi(L\widetilde{\boldsymbol{x}},\tau\widetilde{t}).\end{aligned} \tag{4.25}$$

The above equations are then transformed to

$$\frac{\partial\widetilde{\phi}_c}{\partial\widetilde{t}} - \widetilde{\nabla}\cdot\left(\frac{\tau}{L^2}\gamma_c\rho_0 kT\widetilde{\nabla}\left(\widetilde{\mu}_c + \widetilde{p}\right)\right) = 0 \tag{4.26}$$

$$\widetilde{\mu}_c(\boldsymbol{x},t) = -\frac{1}{2}\left(\frac{\varepsilon_c kT}{L^2\rho_0 e^2} - \frac{\varepsilon_p kT}{L^2\rho_0 e^2}\right)|\widetilde{\nabla}\widetilde{\psi}|^2 + 2\psi + \widetilde{f}_h'(\widetilde{\phi}_c) - \frac{(\epsilon_c^2+\epsilon_p^2)}{\rho_0 kTL^2}\widetilde{\Delta}\widetilde{\phi}_i. \tag{4.27}$$

$$-\widetilde{\nabla}\cdot\left(\frac{1}{L^2}\gamma_c\rho_0 kT\phi_c^2\widetilde{\nabla}\mu_c\right) - \widetilde{\nabla}\left(\frac{1}{L^2}\left(\gamma_c\rho_0 kT\phi_c^2 + \gamma_p\rho_0 kT(1-\phi_c)^2\right)\widetilde{\nabla}p\right) = 0 \tag{4.28}$$

$$-\widetilde{\nabla}\cdot\left(\left[\frac{\varepsilon_c kT}{L^2e^2\rho_0}\phi_c + \frac{\varepsilon_p kT}{L^2e^2\rho_0}(1-\phi_c)\right]\widetilde{\nabla}\widetilde{\psi}\right) = 2\widetilde{\phi}_c - 1. \tag{4.29}$$

Defining $\widetilde{\eta} = \frac{\eta}{L}$, we have the boundary conditions

$$-\left(\frac{\varepsilon_c(kT)^2}{2\widetilde{\eta}Le^2} - \frac{\varepsilon_p(kT)^2}{2\widetilde{\eta}Le^2}\right)\left(\widetilde{\psi}-\widetilde{\psi}_0\right)^2 + \left(\frac{\epsilon_p^2}{L}+\frac{\epsilon_c^2}{L}\right)\widetilde{\nabla}\widetilde{\phi}_c\cdot\boldsymbol{n} = 0. \tag{4.30}$$

So as to introduce parameters used in the previous equations, we multiply both sides of (4.30) by $\frac{1}{L\rho_0 kT}$ so that

$$-\left(\frac{1}{2\widetilde{\eta}}\frac{\varepsilon_c kT}{\rho_0 L^2e^2} - \frac{1}{2\widetilde{\eta}}\frac{\varepsilon_p kT}{\rho_0 L^2e^2}\right)\left(\widetilde{\psi}-\widetilde{\psi}_0\right)^2 + \left(\frac{\epsilon_p^2}{\rho_0 kTL^2}+\frac{\epsilon_c^2}{\rho_0 kTL^2}\right)\widetilde{\nabla}\widetilde{\phi}_c\cdot\boldsymbol{n} = 0. \tag{4.31}$$

We define

$$\begin{aligned}
\widetilde{\varepsilon}_i &= \frac{\varepsilon_i kT}{\rho_0 L^2e^2}\\
\widetilde{\epsilon}_i^2 &= \frac{\epsilon_i^2}{\rho_0 kTL^2}\\
\widetilde{\gamma}_i &= \frac{\gamma_i\rho_0 kT}{L^2}\\
\tau &= \frac{1}{\widetilde{\gamma}_i}.
\end{aligned} \tag{4.32}$$

With these definitions the nondimensional equations are

$$\begin{aligned}
&\frac{\partial\widetilde{\phi}_c(\widetilde{\boldsymbol{x}},\widetilde{t})}{\partial\widetilde{t}} - \widetilde{\nabla}\cdot\left(\phi_c^2(\boldsymbol{x},t)\widetilde{\nabla}\left(\widetilde{\mu}_c+\widetilde{p}\right)\right) = 0\\
&\widetilde{\mu}_c(\boldsymbol{x},t) = -\frac{1}{2}\left(\widetilde{\varepsilon}_c-\widetilde{\varepsilon}_p\right)|\widetilde{\nabla}\widetilde{\psi}|^2 + 2\widetilde{\psi} + \widetilde{f}_h'(\widetilde{\phi}_c) - (\widetilde{\epsilon}_c^2+\widetilde{\epsilon}_p^2)\widetilde{\Delta}\widetilde{\phi}_c\\
&-\widetilde{\nabla}\cdot\left(\left[\widetilde{\varepsilon}_c\phi_c+\widetilde{\varepsilon}_p(1-\phi_c)\right]\widetilde{\nabla}\widetilde{\psi}\right) = 2\widetilde{\phi}_c - 1.
\end{aligned} \tag{4.33}$$

$$\left[\left(\widetilde{\psi}-\widetilde{\psi}_0\right)+\widetilde{\eta}\widetilde{\nabla}\widetilde{\psi}\cdot\boldsymbol{n}\right] = 0 \tag{4.34}$$

$$-\frac{1}{2\widetilde{\eta}}\left(\widetilde{\varepsilon}_c-\widetilde{\varepsilon}_p\right)\left(\widetilde{\psi}-\widetilde{\psi}_0\right)^2 + \left(\widetilde{\epsilon}_p^2+\widetilde{\epsilon}_c^2\right)\widetilde{\nabla}\widetilde{\phi}_c\cdot\boldsymbol{n} = 0 \tag{4.35}$$

where f_h is the logarithmic Flory-Huggins free energy

$$\widetilde{f}_h = \widetilde{\phi}_c\ln\widetilde{\phi}_c + \frac{1}{N_p}\widetilde{\phi}_p\ln\widetilde{\phi}_p + \chi_{pc}\widetilde{\phi}_p\widetilde{\phi}_c \tag{4.36}$$

with boundary conditions for the top and bottom of the computational domain

$$\nabla\mu_i\cdot\boldsymbol{n} = \nabla p\cdot\boldsymbol{n} = 0 \tag{4.37}$$

and periodic boundary conditions for the left and right side of the domain to simulate an semi-infinite system.

Note that when assuming a system with permittivities that are equal, so $\widetilde{\varepsilon} = \widetilde{\varepsilon}_p = \widetilde{\varepsilon}_c$, this system reduces to

$$\frac{\partial\widetilde{\phi}_c}{\partial\widetilde{t}} - \nabla\cdot\left(\widetilde{\phi}_c^2\nabla\left(\widetilde{\mu}_c+\widetilde{p}\right)\right) = 0 \tag{4.38}$$

$$\widetilde{\mu}_c = \widetilde{f}_h'(\widetilde{\phi}_c) - \left(\widetilde{\epsilon}_c^2+\widetilde{\epsilon}_p^2\right)\widetilde{\Delta}\widetilde{\phi}_c + 2\widetilde{\psi} \tag{4.39}$$

$$-\widetilde{\varepsilon}\widetilde{\Delta}\widetilde{\psi} = -1 + 2\widetilde{\phi}_c \tag{4.40}$$

$$-\nabla\cdot\left(\widetilde{\gamma}_c\widetilde{\phi}_c^2\widetilde{\nabla}\left(\widetilde{\mu}_c\right)\right) - \widetilde{\nabla}\cdot\left(\left(\widetilde{\gamma}_p(1-\widetilde{\phi}_c)^2+\widetilde{\gamma}_c\widetilde{\phi}_c^2\right)\widetilde{\nabla}\widetilde{p}\right) = 0 \tag{4.41}$$

with

$$\widetilde{f}_h(\widetilde{\phi}_c) = \widetilde{\phi}_c\ln\widetilde{\phi}_c + \frac{1}{N_p}(1-\widetilde{\phi}_c)\ln(1-\widetilde{\phi}_c) + \widetilde{\chi}\widetilde{\phi}_c(1-\widetilde{\phi}_c). \tag{4.42}$$

The system (4.38)-(4.43) bears resemblence to the Poisson-Nernst-Planck (PNP) equations which is derived from an energy similar to (4.7) for which conservative, accurate numerical schemes is an area of active research [23, 22]. Compared to the PNP equations, this system includes energy effects from the gradients of the volume fractions in $\frac{\epsilon_i^2}{2}|\nabla\phi_i|^2$ and the Flory interaction term $\chi_{pc}\phi_c\phi_p$ in the homogeneous free energy.

4.3 Numerical Method and Simulation

4.3.1 Numerical Method

We consider now discretizing the nondimensional system (4.38)-(4.43) via cell centered finite differences which is first order in time second order in space on a square domain. Let s, h be the time and space step sizes. We introduce the notation

$$f_h(\phi_c^{n+1}, \phi_c^n) = \phi_c^{n+1} \ln_\delta \phi_c^{n+1} + \frac{1}{N_p}(1-\phi_c^{n+1}) \ln_\delta(1-\phi_c^{n+1}) + \chi\phi_c^n(1-\phi_c^n). \tag{4.43}$$

where the regularized logarithm

$$\ln_\delta(x) = \begin{cases} \ln(x) & x > \delta \\ \ln(\delta) + 2\frac{x}{\delta} - \frac{x^2}{2\delta^2} - 1.5 & x \leq \delta \end{cases} \tag{4.44}$$

has been used. Similar to the previous application, we have split the homogeneous free energy into a convex and a non-convex piece. We define

$$G^I(\phi_c^{n+1}) = \frac{\partial}{\partial\phi_c^{n+1}} f_h(\phi_c^{n+1}, \phi_c^n) \tag{4.45}$$

$$G^E(\phi_c^n) = \frac{\partial}{\partial\phi_c^n} f_h(\phi_c^{n+1}, \phi_c^n) \tag{4.46}$$

After excluding the tildes, we have

$$\phi_c^{n+1} - s\nabla_h \cdot \left(M_c(\phi_c^n)\nabla_h\left(\mu_c^{n+1} + p^{n+1}\right)\right) = \phi_c^n = F_\phi \tag{4.47}$$

$$\mu_c^{n+1} - G^I(\phi_c^{n+1}) + \left(\epsilon_c^2 + \epsilon_p^2\right)\Delta_h\phi_c^{n+1} - 2\psi^{n+1} = G^E(\phi_c^n) = F_\mu \tag{4.48}$$

$$-\varepsilon\Delta_h\psi^{n+1} = -1 + 2\phi_c^n = F_\psi \tag{4.49}$$

$$-\nabla_h\cdot\left(M_c(\phi_c^n)\nabla_h\left(\mu_c^{n+1}\right)\right) - \nabla_h\cdot\left(\left(M_p(\phi_p^n) + M_c(\phi_c^n)\right)\nabla_h p^{n+1}\right) = 0 = F_p \tag{4.50}$$

with

$$M_i(\phi_i) = \gamma_i\phi_i^2. \tag{4.51}$$

We use a red-black Gauss-Seidel method for the smoother in the implemented FAS multigrid method described previously in 3.3.2. So as to describe the Gauss-Seidel iteration, we use $\phi^{l+1}(j,k)$ to indicate the grid function value of the $l+1$ Gauss-Seidel iterate at cell (j,k), and drop the time index. Again, similar to Chapter 3, we describe a Jacobi-like method for simplicity. In 4.52 we approximate G^I with a local Newton approximation, and we solve

$$\begin{aligned}
&\mu_c^l - \left(G^I(\phi_c^l) + \frac{dG^I(\phi_c^l)}{d\phi_c}(\phi_c^{l+1} - \phi_c^l)\right)\\
&+ \frac{\left(\epsilon_c^2 + \epsilon_p^2\right)}{h^2}\left(\phi_c^l(j-1,k) + \phi_c^l(j+1,k) + \phi_c^l(j,k-1) + \phi_c^l(j,k+1) - 4\phi_c^{l+1}(j-1,k)\right)\\
&= F_\mu + 2\psi^l(j,k).
\end{aligned} \tag{4.52}$$

We write the rest of the linear equations of the smoother assuming constant mobility M_c for the continuity equation for simplicity

$$\begin{aligned}
\phi_c^{l+1} &- \frac{sM_c}{h^2}\left(-4\mu_c^{l+1}(j,k) - 4p^{l+1}(j,k)\right)\\
&- \frac{sM_c}{h^2}\left(\mu_c^l(j-1,k) + \mu_c^l(j+1,k) + \mu_c^l(j,k-1) + \mu_c^l(j,k+1)\right)\\
&- \frac{sM_c}{h^2}\left(p^l(j-1,k) + p^l(j+1,k) + p^l(j,k-1) + p^l(j,k+1)\right)\\
&= F_\phi
\end{aligned} \tag{4.53}$$

$$\frac{4\varepsilon}{h^2}\psi^{l+1}(j,k) - \frac{\varepsilon}{h^2}\left(\psi^l(j-1,k) + \psi^l(j+1,k) + \psi^l(j,k-1) + \psi^l(j,k+1)\right) = F_\psi \tag{4.54}$$

$$
\begin{aligned}
&- \frac{M_c}{h^2}\left(-4\mu_c^{l+1}(j,k) + \mu_c^l(j-1,k) + \mu_c^l(j+1,k) + \mu_c^l(j,k-1) + \mu_c^l(j,k+1)\right) \\
&- \frac{M_c + M_p}{h^2}\left(-4p^{l+1}(j,k) + p^l(j-1,k) + p^l(j+1,k) + p^l(j,k-1) + p^l(j,k+1)\right) = F_p.
\end{aligned} \tag{4.55}
$$

Boundary Conditions

We implement boundary conditions by adding one extra layer of ghost cells to the computational domain. The homogeneous Neumann boundary conditions can be handled similar to (3.93). Upon assuming $\varepsilon_c = \varepsilon_p$, the only new type of boundary condition in need of description is (4.34). On the bottom boundary, for example, we approximate

$$
\psi(j, \frac{1}{2}) = \frac{1}{2}\left(\psi(j,0) + \psi(j,1)\right) \tag{4.56}
$$

where $\psi(j,0)$ are ghost cell values for ψ. This leads to the boundary conditions implemented as

$$
\psi(j, \frac{1}{2}) - \psi_0 + \eta\frac{\psi(j,0) - \psi(j,1)}{h} = 0 \tag{4.57}
$$

and similarly for other boundaries.

4.3.2 Simulations

For this set of simulations we examine the dependence of the parameters N_p and ϵ_i on the time evolution of the solution variable ϕ_c. Simulations were run on a 256 by 256 uniform grid on a computational domain of size 50 by 50 until steady state is reached. We initialize all simulations with ϕ_c to be a number chosen at random between 0 and 1 on each cell at the first time step. All simulations have an applied voltage of -10 on the bottom, 10 on the top, which causes the attraction of positive charge to the bottom boundary, where $\phi_c \approx 1$ for large enough time, and negative charge on the top boundary, where $\phi_c \approx 0$. In the bulk, we observe a lamellar pattern for large ϵ_i and small N_p at steady state, with the solution

Table 4.1: Parameters for Simulation 1 of an Ionic Fluid

Gradient Energy Coefficients		Mobilities		Boundary Potentials	
ϵ_{sv}^2	.5	γ_{sv}	1.0	$\psi_0(x, 50)$	10.0
ϵ_{sl}^2	.5	γ_{sl}	1.0	$\psi_0(x, 0)$	-10.0

Miscellaneous Parameters	
χ	4.0
δ	.001
N_p	1.0

Table 4.2: Parameters for Simulation 2 of an Ionic Fluid

Gradient Energy Coefficients		Mobilities		Boundary Potentials	
ϵ_{sv}^2	.5	γ_{sv}	1.0	$\psi_0(x, 50)$	10.0
ϵ_{sl}^2	.5	γ_{sl}	1.0	$\psi_0(x, 0)$	-10.0

Miscellaneous Parameters	
χ	4.0
δ	.001
N_p	10.0

diverging from these structures to a labyrinthine pattern with smaller ϵ_i and increased N_p. For the gradient energies, this is what is predicted via a stability analysis [25].

Simulation 1

For the first simulation we choose values for the nondimensional gradient energies large enough to that at equilibrium a lamellar structure is energetically preferred. We see in Figure 4.1 that very shortly after initialization, compared to the next simulations, the system reaches steady state with a lamellar structure.

Simulation 2

A second simulation with parameters listed in Table 4.2, the same as the first simulation, except with increased polymer chain length N_p in the homogeneous free energy f_h. We see in Figures 4.2, 4.3 a more irregular, labyrinthine microstructure develops compared to the first simulation.

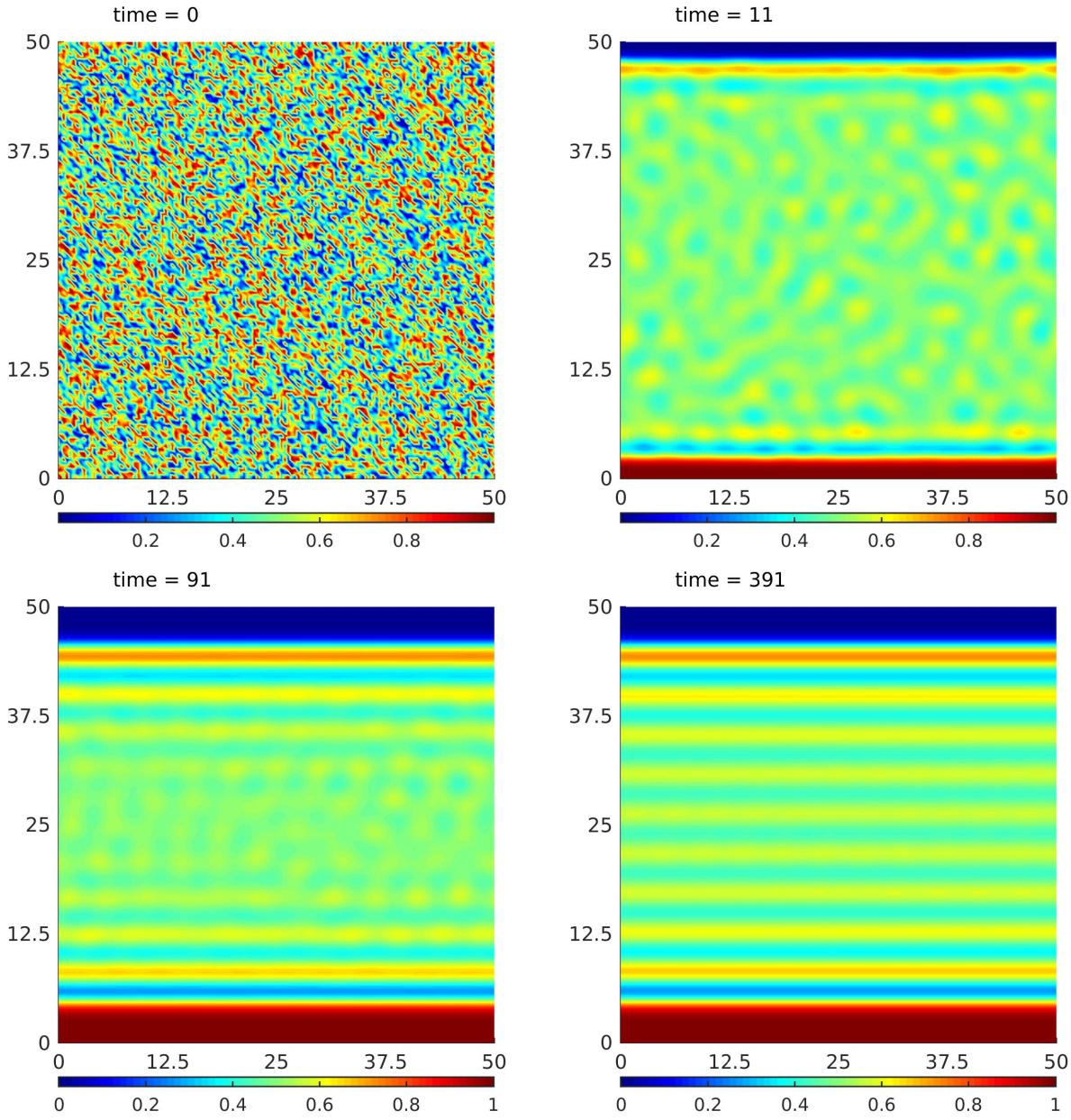

Figure 4.1: We plot the counterion's volume fraction ϕ_c at multiple times with parameters from Table 4.1. We see that near the top an bottom boundary the mixture phase separates into relatively pure phases. We observe phase separation in the bulk and formation of a lamellar pattern due to the large gradient energy for this simulation.

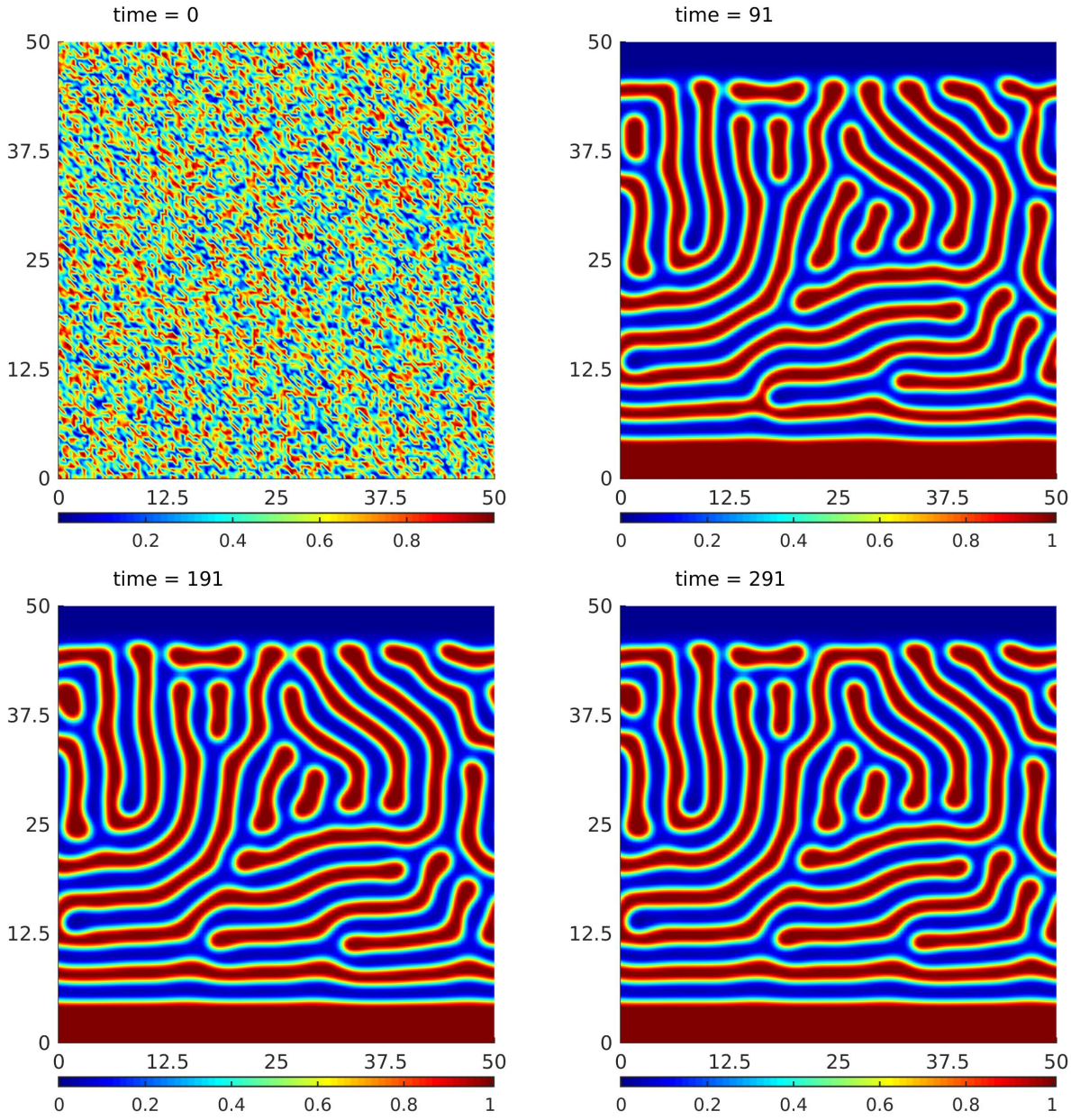

Figure 4.2: We plot the counterion's volume fraction ϕ_c at multiple times with parameters from Table 4.2. We see that near the top an bottom boundary the mixture phase separates into relatively pure phases. In Figure 4.3, we see the bulk phase separates and forms a labyrinthine pattern, differing from the lamellar pattern seen in Figure 4.1 which is due to the increase in the polymer chain length in the homogeneous free energy.

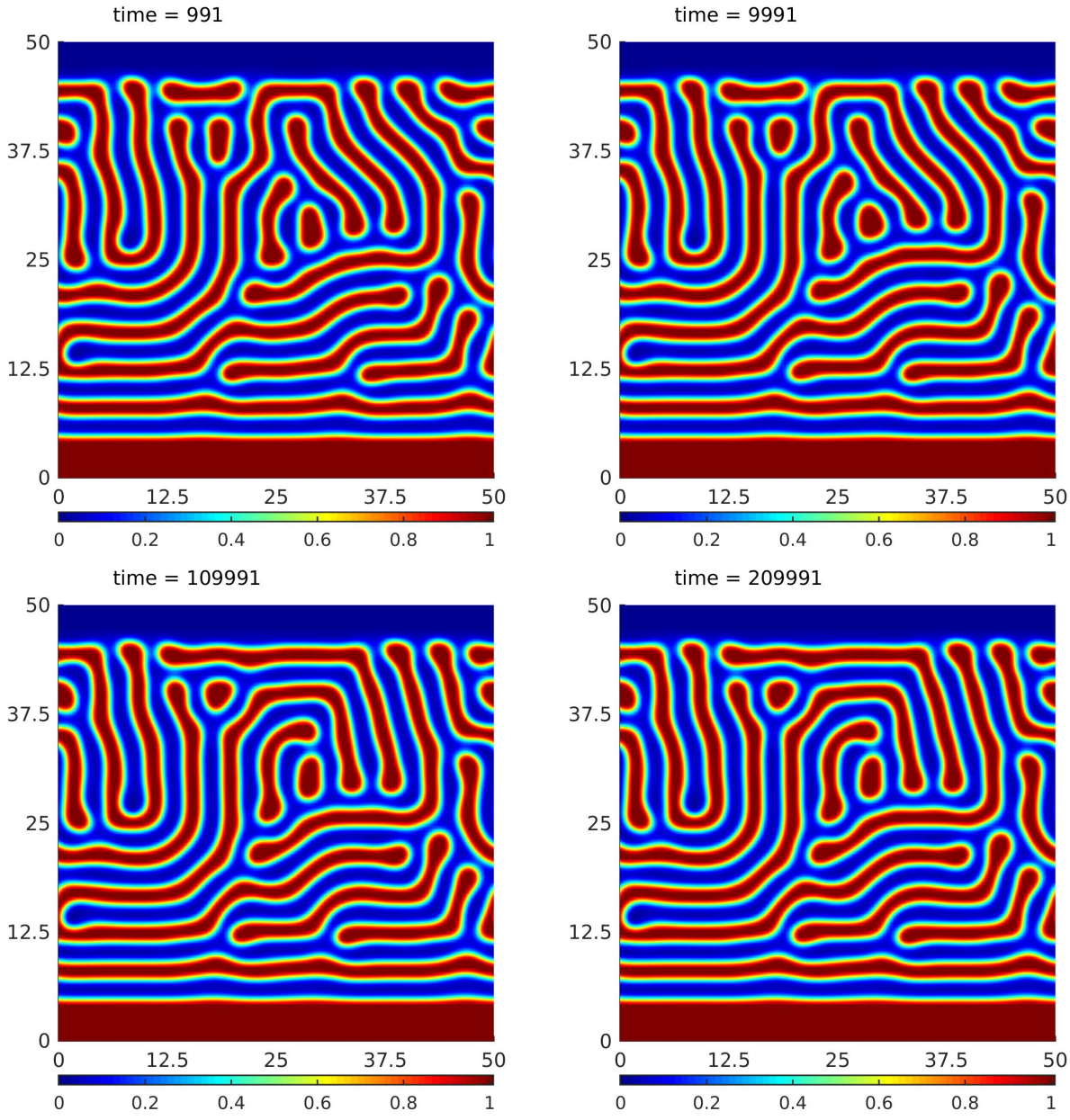

Figure 4.3: We plot a second set of the counterion's volume fraction ϕ_c at multiple times with parameters from Table 4.2. We see that near the top an bottom boundary the mixture phase separates into relatively pure phases. In Figure 4.3, we see the bulk phase separates and forms a labyrinthine pattern, differing from the lamellar pattern seen in Figure 4.1 which is due to the increase in the polymer chain length in the homogeneous free energy.

Table 4.3: Parameters for Simulation 3 of an Ionic Fluid

Gradient Energy Coefficients		Mobilities		Boundary Potentials	
ϵ_{sv}^2	.1	γ_{sv}	1.0	$\psi_0(x, 50)$	10.0
ϵ_{sl}^2	.1	γ_{sl}	1.0	$\psi_0(x, 0)$	-10.0

Miscellaneous Parameters	
χ	4.0
δ	.001
N_p	1.0

Table 4.4: Parameters for Simulation 4 of an Ionic Fluid

Gradient Energy Coefficients		Mobilities		Boundary Potentials	
ϵ_{sv}^2	.3	γ_{sv}	1.0	$\psi_0(x, 50)$	10.0
ϵ_{sl}^2	.3	γ_{sl}	1.0	$\psi_0(x, 0)$	-10.0

Miscellaneous Parameters	
χ	4.0
δ	.001
N_p	1.0

Simulation 3

In this simulation, with parameters from Table 4.3, we decrease the gradient energy coefficients by an amount sufficient enough for the system to energetically prefer the labyrinthine structure in the bulk, as seen in Figures 4.4, 4.5, which can be predicted via a stability analysis [25].

Simulation 4

The last simulation we plot has gradient energy coefficients which lie between that of Tabel 4.1 and Table 4.3. At steady state in Figures 4.6, 4.7 we see a compromise between the lamellar pattern that is observed in Figure 4.1 and the labyrinthine patterns that form in Figures 4.4, 4.5.

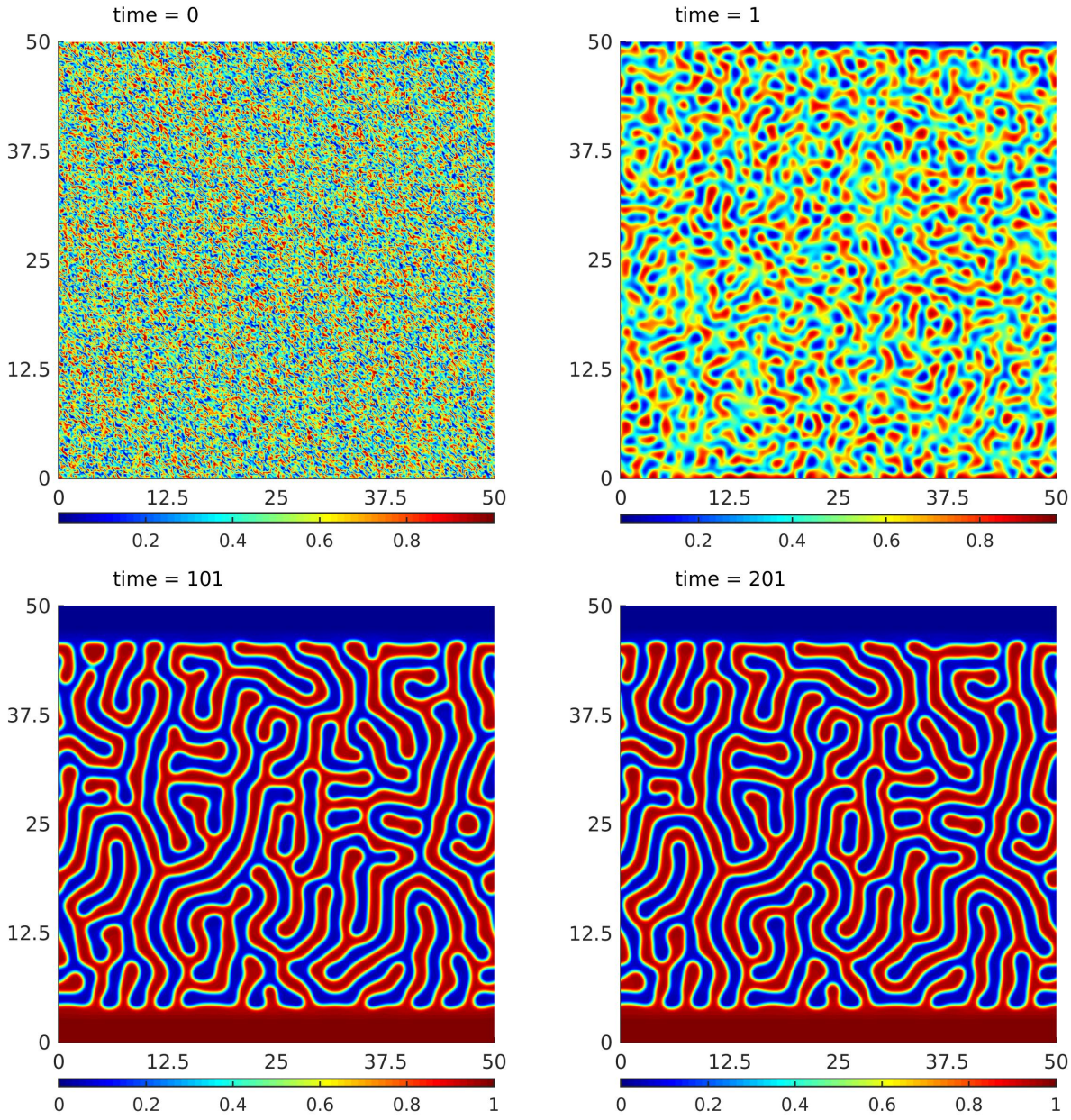

Figure 4.4: We plot the counterion's volume fraction ϕ_c at multiple times with parameters from Table 4.3. We see that near the top an bottom boundary the mixture phase separates into relatively pure phases. In Figure 4.3, we see the bulk phase separates and forms a labyrinthine pattern, differing from the lamellar pattern seen in Figure 4.1 which result from the decreased gradient energy coefficients in 4.3.

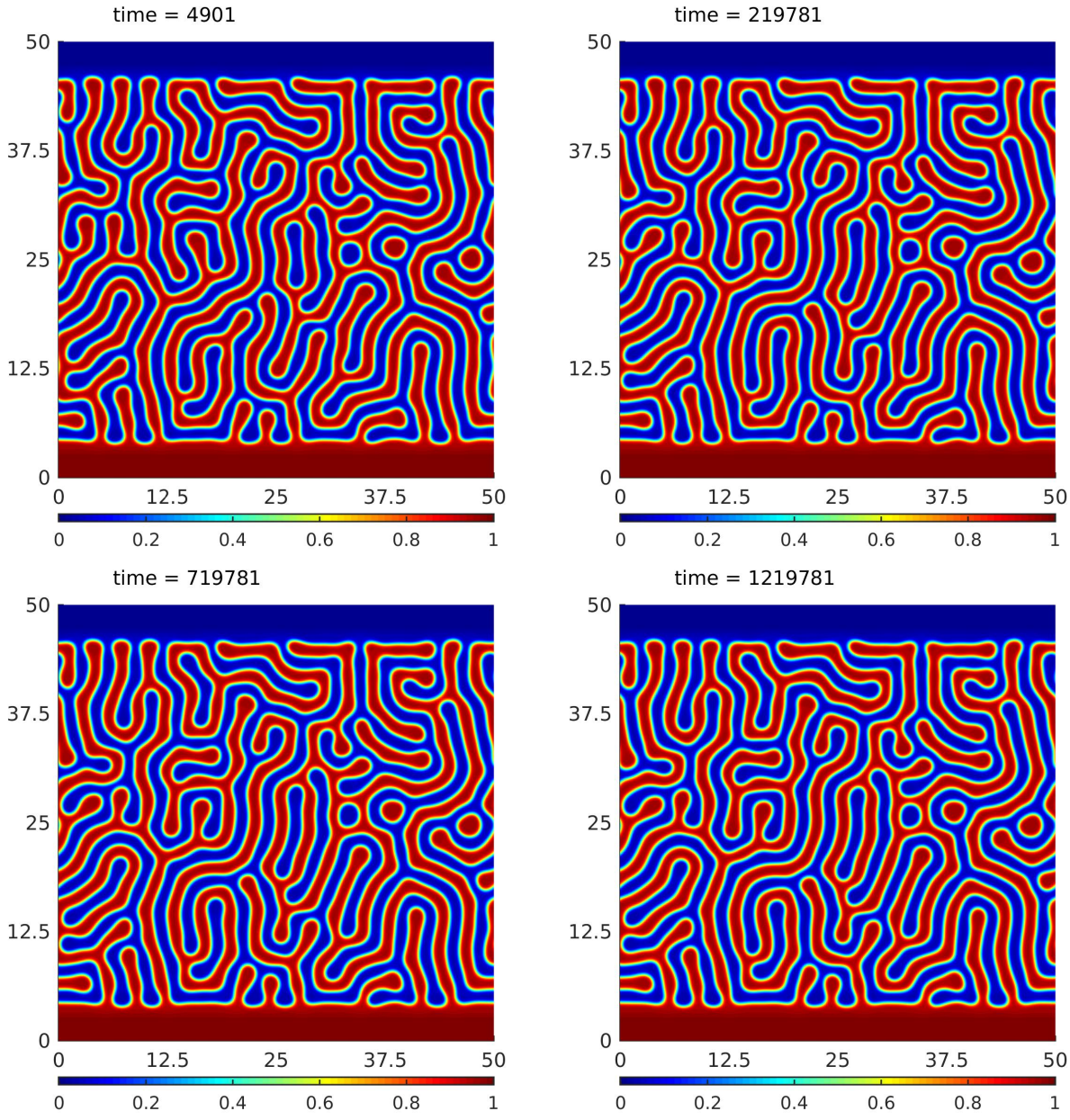

Figure 4.5: We plot a second set of the counterion's volume fraction ϕ_c at multiple times with parameters from Table 4.3. We see that near the top an bottom boundary the mixture phase separates into relatively pure phases. In Figure 4.3, we see the bulk phase separates and forms a labyrinthine pattern, differing from the lamellar pattern seen in Figures 4.1 which result from the decreased gradient energy coefficients in 4.3.

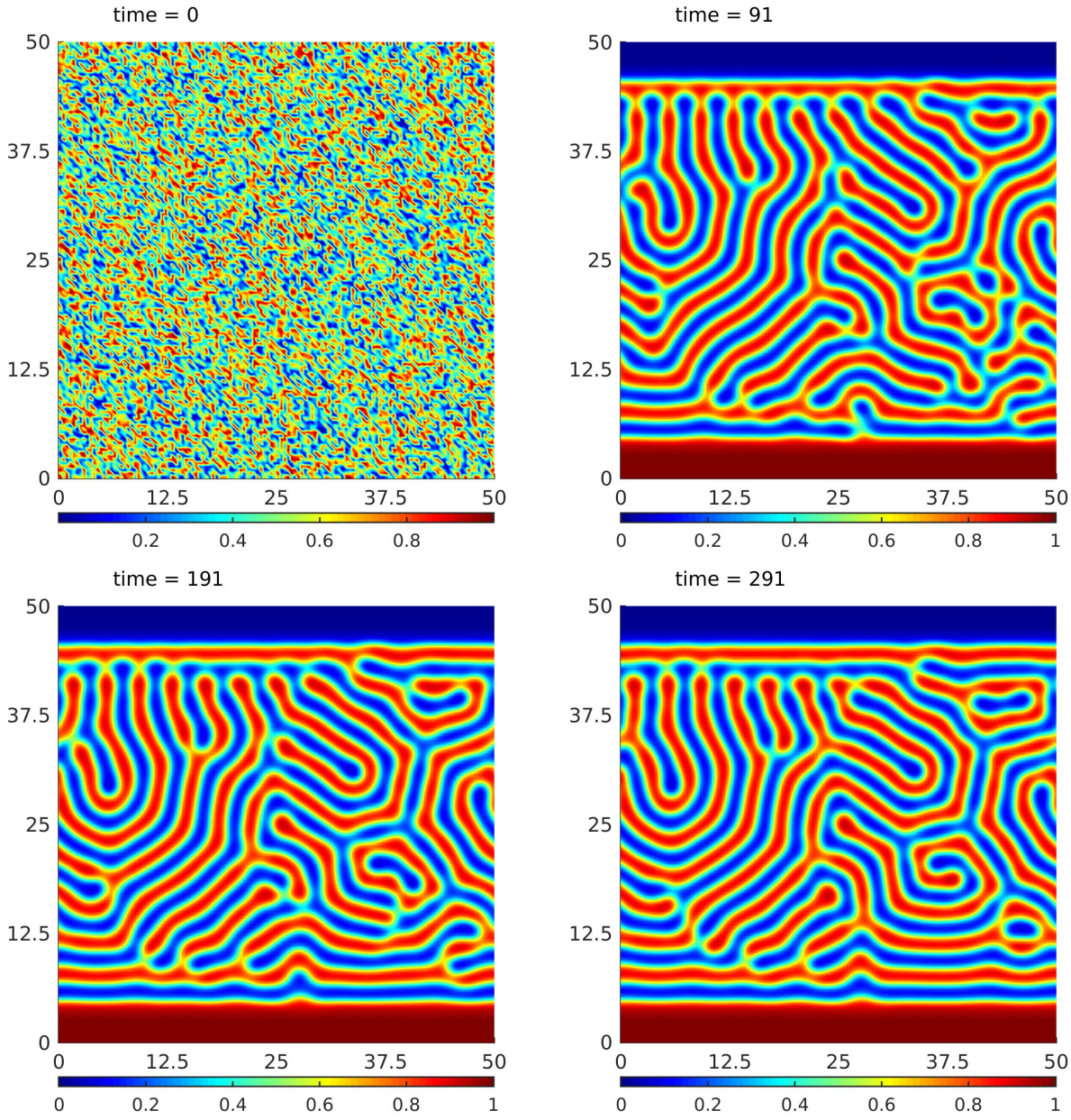

Figure 4.6: We plot the counterion's volume fraction ϕ_c at multiple times with parameters from Table 4.4. We see that near the top an bottom boundary the mixture phase separates into relatively pure phases. In Figure 4.7, we see the bulk phase separates to form structures that resemble the lamellar pattern nearer to the boundaries with regions that are more labyrinthine-like.

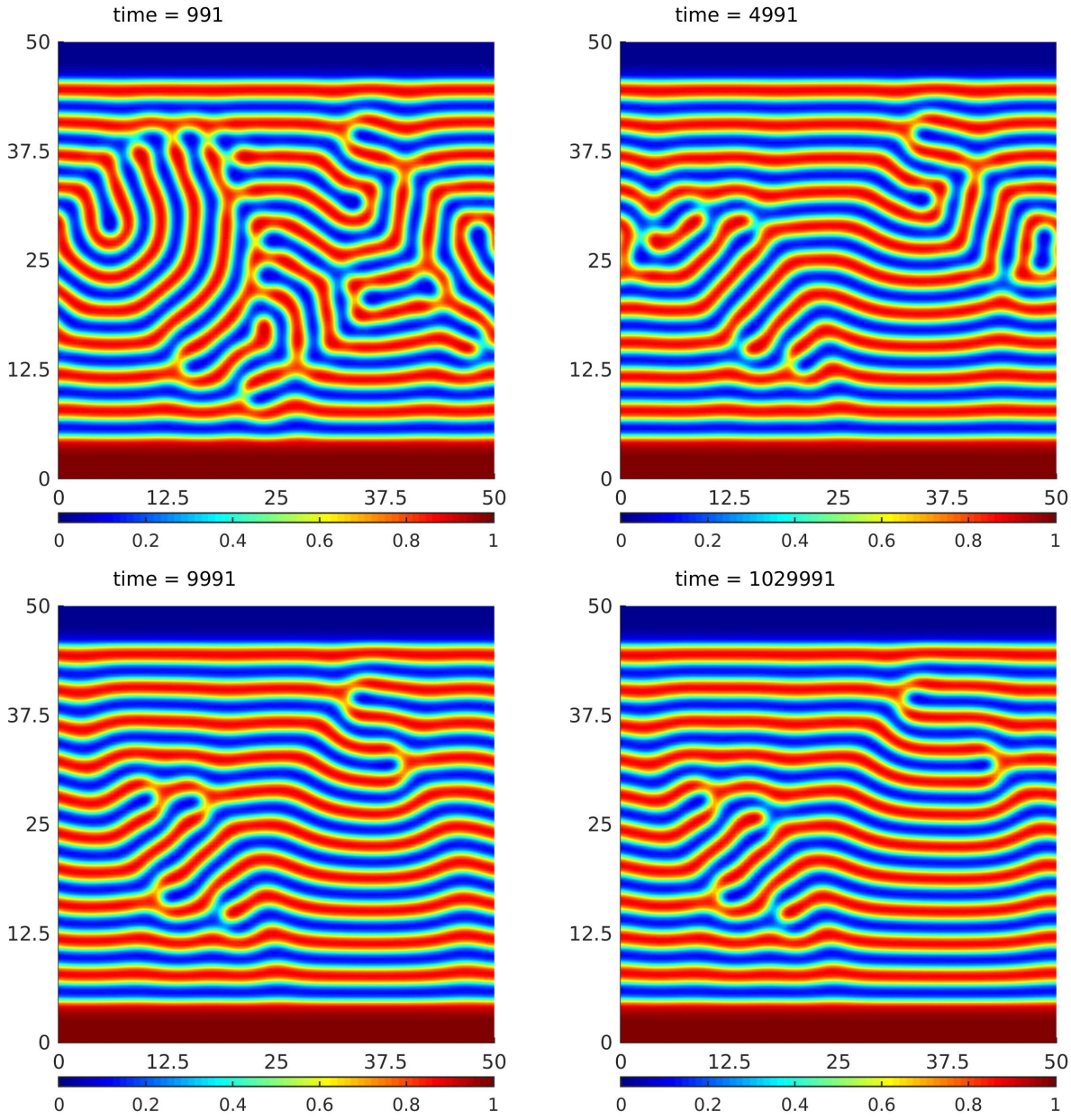

Figure 4.7: We plot a second set of the counterion's volume fraction ϕ_c at multiple times with parameters from Table 4.4. We see that near the top an bottom boundary the mixture phase separates into relatively pure phases. Here we see the bulk phase separates to form structures that resemble the lamellar pattern nearer to the boundaries with regions that are more labyrinthine-like.

4.4 Conclusions and Future Directions

We have applied our general mixture model derived in Chapter 2, including new electric contributions to the free energy. The modeling is done for an arbitrary number of components with possibly varying permittivities. We have provided simulations that demonstrate the microstructural evolution of the mixture and its dependence on the gradient energies and polymer length in the case of constant permittivities. As a future work, we will provide simulations that compute the electric current produced by this model, as well as provide simulations for systems in which the permittivities for the individual components are not necessarily matched.

Bibliography

[1] Abels, H., Garcke, H., and Grün, G. (2011). Thermodynamically consistent, frame indifferent diffuse interface models for incompressible two-phase flows with different densities. 8

[2] Agar, J. C., Damodaran, A. R., Okatan, M. B., Kacher, J., Gammer, C., Vasudevan, R. K., Pandya, S., Dedon, L. R., Mangalam, R. V. K., Velarde, G. A., Jesse, S., Balke, N., Minor, A. M., Kalinin, S. V., and Martin, L. W. (2016). Highly mobile ferroelastic domain walls in compositionally graded ferroelectric thin films. *Nature Materials*, 15(5):549–556. Article. 32

[3] Barrett, J. and Clement, C. (1992). Kinetic evaporation and condensation rates and their coefficients. *Journal of Colloid and Interface Science*, 150(2):352 – 364. 34

[4] Barrett, J. W. and Blowey, J. F. (1995). An errorbound for the finite element approximation of the Cahn-Hilliard equation with logarithmic free energy. *Numerische Mathematik*, 72(1):1–20. 45

[5] Barrett, J. W. and Blowey, J. F. (1996). An error bound for the finite element approximation of a model for phase separation of a multi-component alloy. *IMA Journal of Numerical Analysis*, 16(2):257–287. 45

[6] Boyer, F. and Lapuerta, C. (2006). Study of a three component Cahn-Hilliard flow model. *ESAIM: Mathematical Modelling and Numerical Analysis*. 7

[7] Cahn, J. W. (1961). On spinodal decomposition. *Acta Metallurgica*, 9(9):795 – 801. 1

[8] Cahn, J. W. and Hilliard, J. E. (1958). Free energy of a nonuniform system. I. Interfacial free energy. *The Journal of Chemical Physics*, 28(2):258–267. 1

[9] Chang, J.-F., Sun, B., Breiby, D. W., Nielsen, M. M., Sölling, T. I., Giles, M., McCulloch, I., and Sirringhaus, H. (2004). Enhanced mobility of poly(3-hexylthiophene) transistors by spin-coating from high-boiling-point solvents. *Chemistry of Materials*, 16(23):4772–4776. 32

[10] Chao, H., Koski, J., and Riggleman, R. A. (2017). Solvent vapor annealing in block copolymer nanocomposite films: a dynamic mean field approach. *Soft Matter*, 13:239–249. 33

[11] Cheng, S., Lechman, J. B., Plimpton, S. J., and Grest, G. S. (2011). Evaporation of Lennard-Jones fluids. *The Journal of Chemical Physics*, 134(22):224704. 33

[12] Copetti, M. (2000). Numerical experiments of phase separation in ternary mixtures. *Mathematics and Computers in Simulation*, 52(1):41 – 51. 9, 45

[13] Cristini, V., Li, X., Lowengrub, J. S., and Wise, S. M. (2008). Nonlinear simulations of solid tumor growth using a mixture model: invasion and branching. *Journal of Mathematical Biology*, 58(4):723. 7

[14] de Gennes, P. G. (1980). Dynamics of fluctuations and spinodal decomposition in polymer blends. *The Journal of Chemical Physics*, 72(9):4756–4763. 36

[15] de Groot, S. and Mazur, P. (1984). *Non-equilibrium Thermodynamics*. Dover Books on Physics. Dover Publications. 32, 34

[16] Deegan, R. D., Bakajin, O., Dupont, T. F., Huber, G., Nagel, S. R., and Witten, T. A. (2000). Contact line deposits in an evaporating drop. *Phys. Rev. E*, 62:756–765. 33

[17] Diegel, A. E. (2015). Numerical analysis of convex splitting schemes for Cahn-Hilliard and coupled Cahn-Hilliard-fluid-flow equations. 8

[18] Doi, M. (2011). Onsager's variational principle in soft matter. *Journal of Physics: Condensed Matter*, 23(28):284118. 29

[19] Doi, M. M. (2013). *Soft Matter Physics*. First edition. 8, 29

[20] Eyre, D. J. (1998). Unconditionally gradient stable time marching the Cahn-Hilliard equation. *MRS Proceedings*, 529. 10, 86

[21] Feng, X. (2006). Fully discrete finite element approximations of the Navier–Stokes–Cahn-Hilliard diffuse interface model for two-phase fluid flows. *SIAM Journal on Numerical Analysis*, 44(3):1049–1072. 8

[22] Flavell, A., Kabre, J., and Li, X. (2017). An energy-preserving discretization for the poisson–nernst–planck equations. *Journal of Computational Electronics*, 16(2):431–441. 97

[23] Flavell, A., Machen, M., Eisenberg, B., Kabre, J., Liu, C., and Li, X. (2014). A conservative finite difference scheme for poisson–nernst–planck equations. *Journal of Computational Electronics*, 13(1):235–249. 97

[24] Garcke, H., Nestler, B., and Stoth, B. (1998). On anisotropic order parameter models for multi-phase systems and their sharp interface limits. *Physica D: Nonlinear Phenomena*, 115(1):87 – 108. 7

[25] Gavish, N. and Yochelis, A. (2016). Theory of phase separation and polarization for pure ionic liquids. *The journal of Physical Chemistry Letters*, 7(7). 8, 100, 104

[26] Grün, G. (2013). On convergent schemes for diffuse interface models for two-phase flow of incompressible fluids with general mass densities. *SIAM Journal on Numerical Analysis*, 51(6):3036–3061. 8

[27] Hu, H. and Larson, R. G. (2002). Evaporation of a sessile droplet on a substrate. *The Journal of Physical Chemistry B*, 106(6):1334–1344. 33

[28] Jeong, D. and Kim, J. (2016). A practical numerical scheme for the ternary Cahn-Hilliard system with a logarithmic free energy. *Physica A: Statistical Mechanics and its Applications*, 442:510 – 522. 7, 9, 45

[29] Kim, S., Misner, M., Xu, T., Kimura, M., and Russell, T. (2004). Highly oriented and ordered arrays from block copolymers via solvent evaporation. *Advanced Materials*, 16(3):226–231. 32, 34

[30] Kouijzer, S., Michels, J. J., van den Berg, M., Gevaerts, V. S., Turbiez, M., Wienk, M. M., and Janssen, R. A. J. (2013). Predicting morphologies of solution processed polymer:fullerene blends. *Journal of the American Chemical Society*, 135(32):12057–12067. PMID: 23863101. 8, 33

[31] Kumar, R., Mahalik, J. P., Bocharova, V., Stacy, E. W., Gainaru, C., Saito, T., Gobet, M. P., Greenbaum, S., Sumpter, B. G., and Sokolov, A. P. (2017). A rayleighian approach for modeling kinetics of ionic transport in polymeric media. *The Journal of Chemical Physics*, 146(6). 8

[32] Lee, H.-G., Lowengrub, J. S., and Goodman, J. (2002). Modeling pinchoff and reconnection in a hele-shaw cell. i. the models and their calibration. *Physics of Fluids*, 14(2):492–513. 8

[33] Li, J. and Wang, Q. (2014). A class of conservative phase field models for multiphase fluid flows.(author abstract). *Journal of Applied Mechanics*, 81(2). 7

[34] Liu, C. and Shen, J. (2003). A phase field model for the mixture of two incompressible fluids and its approximation by a fourier-spectral method. *Physica D: Nonlinear Phenomena*, 179(3):211–228. 8

[35] Okuzono, T., Ozawa, K., and Doi, M. (2006). Simple model of skin formation caused by solvent evaporation in polymer solutions. *Phys. Rev. Lett.*, 97:136103. 33

[36] Onuki, A. (2008). Surface tension of electrolytes: Hydrophilic and hydrophobic ions near an interface. *The Journal of Chemical Physics*, 128(22):224704. 33

[37] Onuki, A. (2009). Bubble and droplet motion in binary mixtures: Evaporation-condensation mechanism and marangoni effect. *Phys. Rev. E*, 79:046311. 33

[38] Ozawa, K., Okuzono, T., and Doi, M. (2006). Diffusion process during drying to cause the skin formation in polymer solutions. *Japanese Journal of Applied Physics*, 45(11R):8817. 33

[39] Paradiso, S. P., Delaney, K. T., García-Cervera, C. J., Ceniceros, H. D., and Fredrickson, G. H. (2014). Block copolymer self assembly during rapid solvent evaporation: Insights into cylinder growth and stability. *ACS Macro Letters*, 3(1):16–20. 8, 33

[40] Paradiso, S. P., Delaney, K. T., Garca-Cervera, C. J., Ceniceros, H. D., and Fredrickson, G. H. (2016). Cyclic solvent annealing improves feature orientation in block copolymer thin films. *Macromolecules*, 49(5):1743–1751. 33

[41] Peter, S., Meyer, H., and Baschnagel, J. (2009). Molecular dynamics simulations of concentrated polymer solutions in thin film geometry. ii. solvent evaporation near the glass transition. *The Journal of Chemical Physics*, 131(1):014903. 33

[42] Prosperetti, A. and Plesset, M. S. (1984). The stability of an evaporating liquid surface. *The Physics of Fluids*, 27(7):1590–1602. 33

[43] Routh, A. F. (2013). Drying of thin colloidal films. *Reports on Progress in Physics*, 76(4):046603. 33

[44] Sellinger, A., Weiss, P. M., Nguyen, A., Lu, Y., Assink, R. A., Gong, W., and Brinker, C. J. (1998). Continuous self-assembly of organic-inorganic nanocomposite coatings that mimic nacre. *Nature*, 394(6690):256–260. 32

[45] Strobl, G. (2007). *The Physics of Polymers: Concepts for Understanding Their Structures and Behavior*. Springer Berlin Heidelberg, Berlin, Heidelberg. 36

[46] Teshigawara, R. and Onuki, A. (2008). Droplet evaporation in one-component fluids: Dynamic van der waals theory. *EPL (Europhysics Letters)*, 84(3):36003. 33

[47] Thiele, U. (2010). Thin film evolution equations from (evaporating) dewetting liquid layers toepitaxial growth. *Journal of Physics: Condensed Matter*, 22(8):084019. 33

[48] Thomas, A. (2017). *A General Mixture Model for Nonlinear Heterogeneous Tumor Growth*. PhD thesis, University of California, Irvine. 7

[49] Tree, D. R., Delaney, K. T., Ceniceros, H. D., Iwama, T., and Fredrickson, G. H. (2017). A multi-fluid model for microstructure formation in polymer membranes. *Soft Matter*, 13:3013–3030. 8, 29

[50] Trottenberg, U., Oosterlee, C., and Schüller, A. (2001). *Multigrid*. Academic Press. 9, 48, 86

[51] Tsige, M. and Grest, G. S. (2005). Solvent evaporation and interdiffusion in polymer films. *Journal of Physics: Condensed Matter*, 17(49):S4119. 33

[52] Ward, C. A. (2002). Liquid-Vapour Phase Change Rates and Interfacial Entropy Production. *Journal of Non Equilibrium Thermodynamics*, 27:289–303. 33, 34

[53] Ward, C. A. and Fang, G. (1999). Expression for predicting liquid evaporation flux: Statistical rate theory approach. *Phys. Rev. E*, 59:429–440. 14, 33, 34

[54] Wise, S., Kim, J., and Lowengrub, J. (2007). Solving the regularized, strongly anisotropic Cahn-Hilliard equation by an adaptive nonlinear multigrid method. *Journal of Computational Physics*, 226(1):414 – 446. 9, 48, 86

[55] Wise, S., Lowengrub, J., and Cristini, V. (2011). An adaptive multigrid algorithm for simulating solid tumor growth using mixture models. *Mathematical and Computer Modelling*, 53(1):1 – 20. 7

[56] Wise, S., Lowengrub, J., Frieboes, H., and Cristini, V. (2008). Three-dimensional multispecies nonlinear tumor growthi. *Journal of Theoretical Biology*, 253(3):524 – 543. 7

[57] Wodo, O. and Ganapathysubramanian, B. (2012). Modeling morphology evolution during solvent-based fabrication of organic solar cells. *Computational Materials Science*, 55:113 – 126. 33

[58] Wodo, O. and Ganapathysubramanian, B. (2014). How do evaporating thin films evolve? Unravelling phase-separation mechanisms during solvent-based fabrication of polymer blends. *Applied Physics Letters*, 105(15):153104. 33

Vita

John T. Cummings was born in Decatur, Ga to Rose and Tim Cummings. He is the oldest of four children: Alan Cummings, Rebecca Cummings, and Margaret Cummings. He attended Berkmar High School in Lilburn, Ga before enrolling at Georgia Perimeter College to complete his core college curriculum. He then transferred to Georgia Institute of Technology, completing his bachelor's degree in mathematics and civil engineering, after which he decided to pursue a mathematics career via attending the University of Tennessee and completing his Ph.D. in applied mathematics. After graduating, John will accept a visiting faculty position at Berry College in Rome, Georgia.